

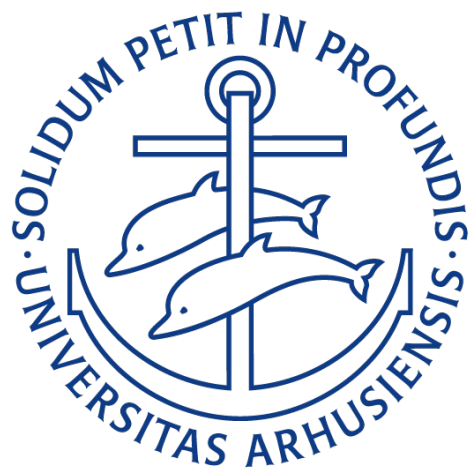
# Investigations of optical Fano microcavities based on pairs of suspended, ultrathin, resonant mirrors

by

Mikkel Kirkegaard Thomsen | 201804798

Supervisor  
**Aurelien Dantan**

A thesis presented for the degree of  
Master of Science



Department of Physics & Astronomy  
Aarhus University  
Denmark  
01.06.2025

# Contents

|   |           |
|---|-----------|
| <b>Abstract</b>   | <b>iv</b> |
| <b>1 Introduction</b>   | <b>1</b>  |
| <b>2 Theory</b>   | <b>4</b>  |
| 2.1 The Fabry-Perot interferometer . . . . .                    | 4         |
| 2.1.1 Transmission . . . . .                                    | 4         |
| 2.1.2 Varying the cavity length . . . . .                       | 6         |
| 2.1.3 Varying the incident wavelength . . . . .                 | 7         |
| 2.1.4 Cavity losses . . . . .                                   | 9         |
| 2.2 The Fano mirror: a sub wavelength grating . . . . .         | 10        |
| 2.2.1 Reflection/transmission spectra and line shape analysis . | 10        |
| 2.2.2 Lossless grating . . . . .                                | 10        |
| 2.2.3 Lossy grating . . . . .                                   | 15        |
| 2.3 The single Fano cavity . . . . .                            | 16        |
| 2.3.1 The single Fano cavity model . . . . .                    | 16        |
| 2.3.2 Transmission linewidth . . . . .                          | 17        |
| 2.4 The double Fano cavity . . . . .                            | 21        |
| 2.4.1 The double Fano cavity model . . . . .                    | 21        |
| 2.4.2 Transmission linewidth . . . . .                          | 22        |
| 2.4.3 Single and double Fano cavity comparison . . . . .        | 23        |
| 2.4.4 Additional cavity losses . . . . .                        | 26        |
| 2.4.5 Spectral detuning (lossless) . . . . .                    | 27        |
| 2.4.6 Spatial detuning (lossless) . . . . .                     | 31        |
| <b>3 Method</b>   | <b>38</b> |
| 3.1 The experimental setup . . . . .                            | 38        |
| 3.1.1 Tunable diode laser . . . . .                             | 39        |
| 3.1.2 $\lambda/2$ - waveplate . . . . .                         | 40        |
| 3.1.3 Optical telescope . . . . .                               | 41        |
| 3.1.4 Transmission, reflection and incident photo-detectors .   | 42        |
| 3.1.5 The double Fano cavity measurement setup . . . . .        | 42        |
| 3.1.6 Vibrational noise reduction . . . . .                     | 45        |
| 3.1.7 Additional equipment used . . . . .                       | 46        |
| 3.2 Characterization of sub-wavelength grating . . . . .        | 46        |
| 3.2.1 The alignment procedure . . . . .                         | 47        |

|                   |  |           |
|-------------------|--|-----------|
| 3.2.2             | Adjusting and measuring the beam waist . . . . .   | 50        |
| 3.2.3             | Obtaining normalized transmission/reflection spectra . . . . .   | 50        |
| 3.3               | Cavity measurements . . . . .  | 52        |
| 3.3.1             | Aligning the double Fano cavity . . . . .  | 53        |
| 3.3.2             | Cavity resonance - the piezo ring . . . . .  | 55        |
| 3.3.3             | Determining the cavity length . . . . .  | 57        |
| 3.3.4             | Recording normalized spectra . . . . .   | 58        |
| 3.3.5             | Centering of the top grating . . . . .   | 59        |
| 3.3.6             | Estimating parallelism . . . . .   | 62        |
| <b>4</b>          | <b>Results</b>   | <b>65</b> |
| 4.1               | Fano mirror characterization . . . . .   | 65        |
| 4.2               | The single Fano cavity . . . . .   | 69        |
| 4.3               | The double Fano cavity . . . . .   | 72        |
| 4.3.1             | Realizing the double fano model . . . . .  | 76        |
| 4.3.2             | The double fano linewidth . . . . .  | 80        |
| 4.4               | Additional discussion . . . . .  | 83        |
| 4.4.1             | Vibrational noise . . . . .  | 83        |
| 4.4.2             | Guided-mode resonance shift . . . . .  | 86        |
| 4.4.3             | Potential broadening due to walk-off effect . . . . .  | 87        |
| <b>5</b>          | <b>Conclusion</b>  | <b>89</b> |
| 5.1               | Outlook . . . . .  | 89        |
| 5.1.1             | Matching analytical and experimental linewidths . . . . .  | 89        |
| 5.1.2             | Optomechanics with the double Fano cavity . . . . .  | 90        |
| 5.1.3             | Sensing applications of the double Fano cavity . . . . .   | 90        |
| 5.1.4             | Fano laser based on bound states in the continuum . . . . .  | 90        |
| <b>References</b> |  | <b>92</b> |
| <b>Appendices</b> |  | <b>98</b> |
| A                 | GitHub . . . . .   | 98        |
| B                 | Additional Fano mirror spectra . . . . .   | 99        |
| C                 | Simulated broadband and single Fano cavity resonance transmission spectra . . . . .                                  | 100       |
| D                 | Simulated single and double Fano cavity resonance transmission spectra . . . . .                                     | 102       |
| E                 | Simulated double Fano cavity resonance transmission spectra for different values of the resonant loss term . . . . . | 103       |

|   |  |     |
|---|--|-----|
| F | Measured single Fano transmission data . . . . . | 104 |
| G | Measured double Fano transmission data . . . . . | 111 |

# Abstract

# 1 Introduction

Cavity electrodynamics[1] is the study of light confined inside an optical resonator and, in the case of this project, quantized as a basis of harmonic oscillator modes[2]. The quantization of the electromagnetic (EM) field inside an optical cavity has been, and continues to be, paramount in the advancement of fields such as optical communication, quantum optics, photonics, sensing, optomechanics[3, 4], etc. The ability to enhance mode selection of a coherent light source allows for an increase in control of a given system, and highly resolved measurements[5].

Many different types of resonators and materials have been utilized for cavity electrodynamics, e.g. beams, drums, photonic crystals and membranes[6, 7]. The latter is here of specific interest, as low mass *Silicon Nitride (SiN)* membranes[8] have proven to posses low losses in the visible- and infrared spectral ranges[9], and has furthermore been shown to have excellent mechanical properties[10, 11]. Examples of applications of *SiN* membranes as mechanical resonators used in cavity electrodynamics are as transducers between optical and microwave fields in telecommunication[12, 13] and in sensing for accelerometry[14, 15], thermometry[16, 17, 18] and pressure sensing[19, 20, 21, 22].

However, while *SiN* membranes are great mechanical resonators, they typically display relatively low reflectivities of  $\sim 10\% - 35\%$ . That is when only the bare membrane is considered. In order to preserve the quality of the mechanical properties along with the low mass, while achieving higher values for the reflectivity, the membranes are patterned with periodic sub-wavelength, 1- or 2-dimensional, photonic crystal structures[23, 24, 25, 26, 27, 28, 29]. In the past decade, tremendous strides have been made in the field of micro- and nano-fabrication methods, and patterned membranes with a record reflectivity of as high as  $\sim 99.9998\%$  have been reported[30, 31, 32].

The type of patterned membrane considered for this project is a 1-dimensional sub-wavelength grating with optical properties well-described by the theory presented by Fan and Joannopoulos [33, 34]. It is thus said to act as so-called *Fano mirrors* with transmission and reflection coefficients dependent on the incident wavelength. The wavelength-dependence gives rise to a *guided-mode* resonance which can be utilized in the designing of optical *Fano* cavities with spectra showcasing ultra-narrow linewidth resonance peaks[35, 36]. By tuning the cavity mode and incoming EM-field to match the guided-mode, one can resolve structures with a linewidth in the low picometer regime for cavity lengths

down to a few microns.

In previous work, the single Fano cavity has been realized and characterized, consisting of a broadband mirror and a Fano mirror in a plane-plane configuration. The Fano cavity have proved to produce ultra-narrow linewidth resonance spectra for very short cavity lengths, while still maintaining a high radiation pressure and thus mechanical Q-factor. This makes them an excellent candidate as subjects for optomechanical experiments and corresponding sensing applications.

In this project we propose the *double Fano cavity* as an expansion of the theory presented for the single Fano cavity by Mitra et al. in [35]. The double Fano cavity consists of two Fano mirrors with each their wavelength-dependent set of optical coefficients and will thus, theoretically, produce an even narrower resonance profile than the *single* Fano cavity. Figure 1 shows schematics for all three aforementioned optical cavities, namely the broadband cavity (1a), single Fano cavity (1b) and double Fano cavity (1c), where  $t_g, r_g$  refers to transmission- and reflection coefficients of a Fano mirror, and  $t_m, r_m$  are the ones for a broadband mirror.

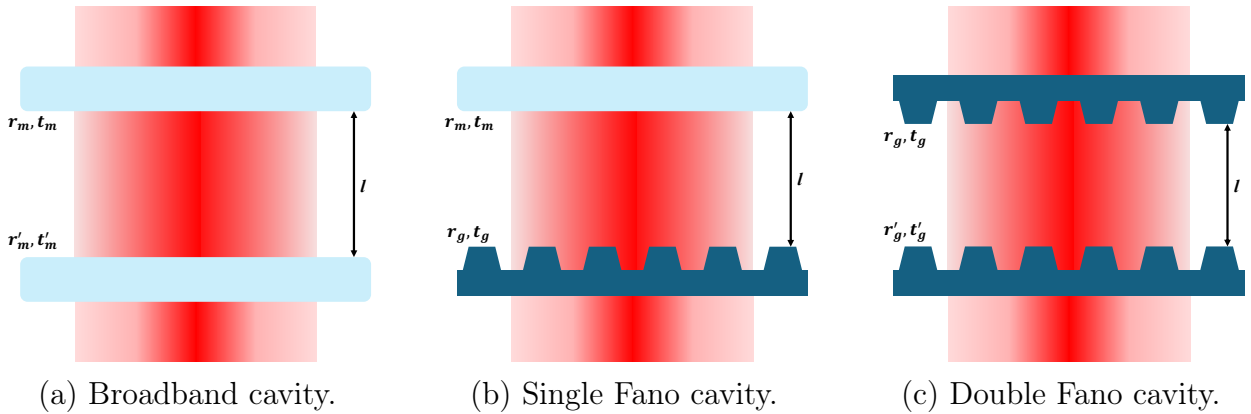


Figure 1

In this thesis I will present the theory of the sub-wavelength grating, i.e. Fano mirrors, and of the single- and double Fano cavities. I will show extensive simulations run for the transmission spectra of the double Fano cavity as a part of my investigations in order to map the on- and off-resonance behaviour as functions of various physical parameters. I will expand in detail on the experimental methods and techniques used in order to realize said theory and outline obstacles faced in that process. Finally I will present the results of my project and compare these with analytical predictions and discuss shortcomings and sources of error and noise of the setup and methods used. I will end by

briefly dicussing the possible outlook of future projects regarding the double Fano cavity and the field of cavity electrodynamics generally in the light of my findings.

## 2 Theory

### 2.1 The Fabry-Perot interferometer

The Fabry-Perot interferometer, also known as an optical cavity, is generally comprised of two reflective optical elements, hereafter referred to as mirrors. In the following we assume a plane-plane configuration for two lossless mirrors and a plane-wave at normal incidence for the incoming field, as sketched in figure 2.

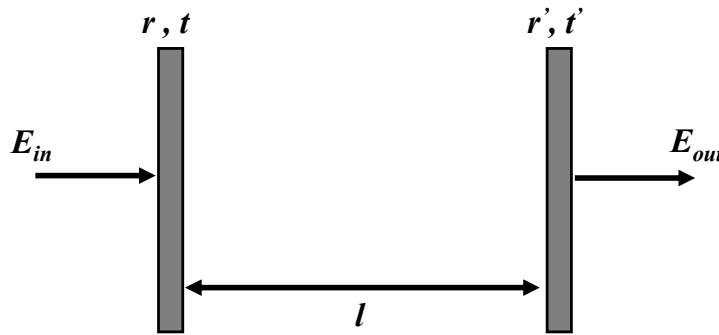


Figure 2: Sketch of a planar Fabry-Perot cavity.

The two mirrors are described by each their respective amplitude coefficients for the reflectivity  $r$  and transmission  $t$  and are placed parallel at a distance  $l$  from each other. The field at the second mirror, i.e. the transmitted field  $E_{out}$  can then be described as a function of the field at the first mirror, i.e. the incident field  $E_{in}$ [37, 38].

#### 2.1.1 Transmission

In order to determine the transmission through the Fabry-Perot cavity, we once again consider the configuration in figure 2. It is further, initially, assumed that the mirrors are both lossless, such that

$$|r|^2 + |t|^2 = |r'|^2 + |t'|^2 = 1. \quad (1)$$

This means that all losses, e.g. due to absorption or scattering, are neglected.

In order to formulate  $E_{out}$  in terms of  $E_{in}$ , we first consider the incident field as a propagating plane-wave with wave number  $k = 2\pi/\lambda$ . We then consider  $E_{out}$  to be comprised of contributions for each roundtrip inside the cavity. This can

be written as an infinite geometrical series given as

$$\begin{aligned}
E_{out} &= tt'E_{in}e^{ik\delta/2} + tt'E_{in}e^{ik\delta/2}rr'e^{i\delta} \\
&\quad + tt'E_{in}e^{ik\delta/2}(rr'e^{i\delta})^2 + tt'E_{in}e^{ik\delta/2}(rr'e^{i\delta})^3 + \dots \\
&= tt'E_{in}e^{ik\delta/2} \sum_{m=0}^{\infty} (rr'e^{i\delta})^m
\end{aligned} \tag{2}$$

where  $\delta = 2kl$ . The first term of the series corresponds to a direct transmission through the cavity, and each term thereafter corresponds to the respective contribution to the transmission after the  $m'th$  round trip.

By evaluating the series it is seen that it converges to the final expression for the transmitted field through a planar Fabry-Perot cavity

$$E_{out} = E_{in} \frac{tt'e^{i\delta/2}}{1 - rr'e^{i\delta}}. \tag{3}$$

The intensity of the transmission is now taken as the square of the norm of the field intensity  $|E_{out}|^2$  and normalizing with respect to the incident field intensity  $|E_{in}|^2$ . We arrive at an expression for the transmission intensity which is an *Airy function*[38]

$$T = \frac{|E_{out}|^2}{|E_{in}|^2} = \left| \frac{tt'e^{i\delta/2}}{1 - rr'e^{i\delta}} \right|^2 = \frac{(1 - |r|^2)(1 - |r'|^2)}{(1 - |rr'|)^2 + 4|rr'|\sin^2(\delta)}, \tag{4}$$

where  $\delta$  is the phase shift associated with each round trip inside the cavity.

Figure 3 displays the Airy function in eq. (4), of a lossless cavity with mirrors of equal reflectivities  $r' = r$ , as a function of  $\delta$  in units of  $\pi$ . The function is plotted for the cases of  $|r|^2 = 50\%$ , shown in blue, and  $|r|^2 = 90\%$ , shown in red. It is readily seen that the transmission is maximized for  $\delta = n2\pi$ , which corresponds to standing wave modes with  $\lambda_n = 2l/n$ . It is further seen that the two cases shown differ significantly as the red profile is much narrower than the blue. The red profile is hence said to have a higher *finesse*  $\mathcal{F}$  than the blue profile. The finesse is a measure of the quality of a cavity by the distance between successive resonance peaks relative to their width. It is thus defined as

$$\mathcal{F} \equiv \frac{FSR}{\delta_\lambda}, \tag{5}$$

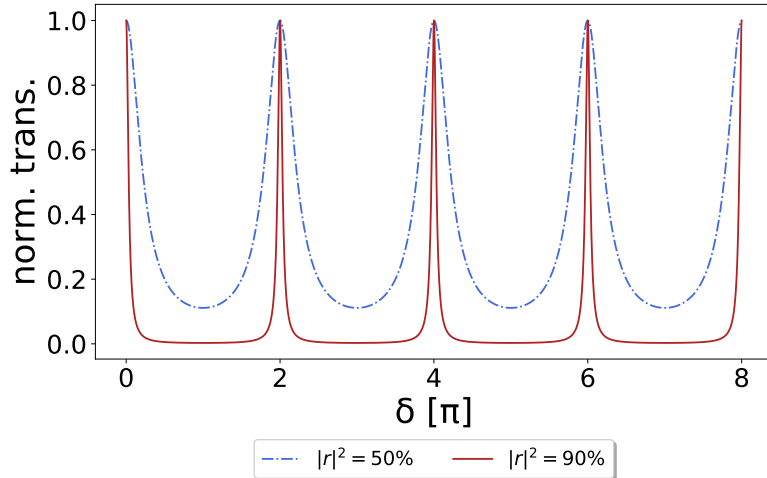


Figure 3: The red line shows the transmission spectrum of a *high* finesse Fabry-Perot cavity of reflectivity  $|r|^2 = 0.90$ , while the blue dashed line shows the transmission spectrum of a *low* finesse cavity with reflectivity  $|r|^2 = 0.50$ .

where  $FSR$  is the so-called *Free Spectral Range* indicating the spectral distance between two peaks and  $\delta_\lambda$  refers to the *Full Width at Half Maximum (FWHM)* which, as the name suggests, is the linewidth defined at half the maximum value for the normalized transmission.

Considering the Airy function in eq. (4) for the high finesse case where  $|r|^2 = |r'|^2 \rightarrow 1$  we furthermore see that each individual peak closely resembles a Lorentzian function.

Note here that the field intensity inside the cavity is closely related to the Fabry-Perot transmission function, this is denoted the so-called *intracavity* intensity. It is representative of the field build-up inside the cavity and is defined as

$$|E_{cav}|^2 \equiv |E_{in}|^2 \left| \frac{1}{1 - rr'e^{i\delta}} \right|^2. \quad (6)$$

### 2.1.2 Varying the cavity length

In order to relate the resonance transmission profile to the length of the cavity we first consider the frequencies at which the cavity is resonant, with respect to the incident light, given as

$$\nu_n = n \frac{c}{2l}, \quad (7)$$

where  $c$  is the speed of light,  $n$  is a positive integer referring to the order of the resonance frequency and  $l$  is the cavity length. This corresponds to resonance occurring at times related to each round trip inside the cavity.

Since the FSR is defined as the spectral distance between each peak, it follows from eq. (7) that it can be expressed in units of frequency as

$$FSR_\nu = \frac{c}{2l}, \quad (8)$$

and the corresponding linewidth, or FWHM,  $\delta_\nu$  is then given as

$$\delta_\nu = \frac{1}{2\pi} \frac{|t|^2 + |t'|^2}{\tau}, \quad (9)$$

where  $\tau = 2l/c$  is the round trip time in seconds.

Finally, considering the definition of the finesse from eq. (5) it can be shown that

$$\mathcal{F} \equiv \frac{FSR_\nu}{\delta_\nu} = \frac{2\pi}{|t|^2 + |t'|^2}, \quad (10)$$

where the finesse is now defined in terms of the total cavity transmission at resonance.

Note here that the relation between the FSR and the cavity length  $l$  is clearly shown in eq. (8), and figure 4 furthermore shows transmission spectra underlining the effect of changing the cavity length.

### 2.1.3 Varying the incident wavelength

In order to simplify the Airy function in eq. (4) we introduce the so-called *coefficient of finesse*  $F$ , which is a function only of the mirror reflectivities, given as

$$F = \frac{4|rr'|}{(1 - |rr'|)^2}. \quad (11)$$

The coefficient of finesse  $F$  is not to be confused with the finesse  $\mathcal{F}$ , as they are not equal, but rather related by

$$\mathcal{F} = \frac{\pi}{2} \sqrt{F}. \quad (12)$$

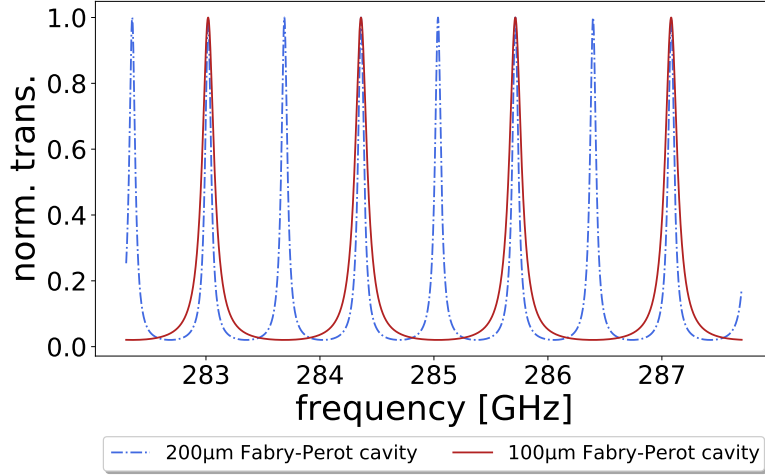


Figure 4: Fabry-Perot transmission spectra for cavities of lengths  $l = 100\mu m$  and  $l = 200\mu m$ . It is clearly seen that the FSR is inversely proportional with the cavity length as it is apparent that  $FSR_{100\mu m} = 2 \cdot FSR_{200\mu m}$ .

Rewriting the Airy function in terms of the coefficient of finesse yields

$$T_\lambda = \frac{1}{1 + F \sin^2(\delta/2)}, \quad (13)$$

where the round trip phase shift  $\delta$  is related to the wavelength  $\lambda$  of the incident light by

$$\delta = 2kl = \frac{4\pi l}{\lambda}, \quad (14)$$

as  $k = 2\pi/\lambda$  is the incident wave number.

Re-writing the general cavity brightness condition, it can easily be shown that the resonant wavelengths for a cavity at normal incidence are given as

$$\lambda_n = \frac{2l}{n}, \quad (15)$$

where  $n = 1, 2, 3, \dots$  is a positive integer referring to the order of the resonance.

Since  $\nu = c/\lambda$ , the relation between the linewidth in wavelength space  $\delta_\lambda$  and the one in frequency space  $\delta_\nu$  is non-linear. Therefore one does not simply make the aforementioned substitution in order to relate them. It can however

be shown that their respective expressions differ by a factor of  $\lambda^2/c$ , and the linewidth when varying the wavelength is thus given as

$$\delta_\lambda = \frac{\lambda^2}{c} \cdot \delta_\nu = \frac{\lambda^2}{4\pi l} (|t|^2 + |t'|^2). \quad (16)$$

Finally we consider the definition for the finesse  $\mathcal{F}$  and the expression given in eq. (10), in order to show that the  $FSR$  in wavelength space is given as

$$FSR_\lambda \equiv \delta_\lambda \cdot \mathcal{F} = \frac{\lambda^2}{2l}. \quad (17)$$

Figure 5 shows an example of the Airy function given in eq. (13) as a function of the wavelength for a lossless Fabry-Perot cavity of reflectivity intensities  $|r|^2 = |r'|^2 = 90\%$ , transmission intensities  $|t|^2 = |t'|^2 = 10\%$  and length  $l = 100\mu m$ . It also includes an example of the transmission function with non-zero cavity losses, this is outlined further in section 2.1.4 below.

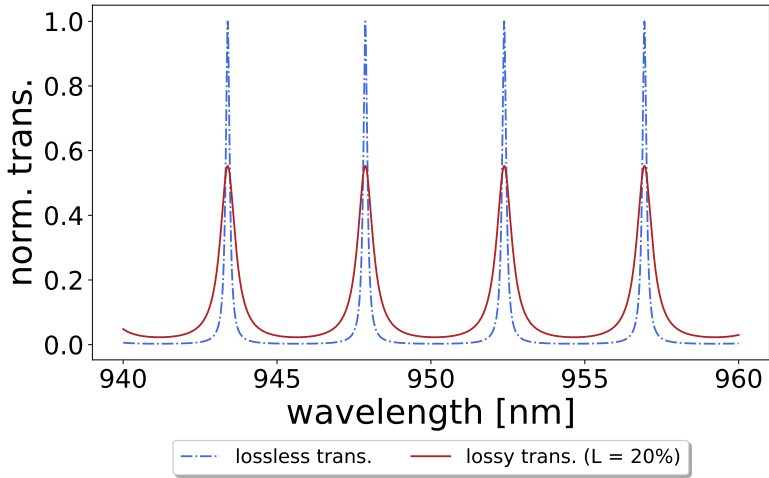


Figure 5: The Airy function as seen in eq. (13) as a function of the incident wavelength for a cavity length of  $l = 100\mu m$ . The blue dashed line shows an example without losses due to e.g. scattering or absorption, while the red line shows an example of a lossy cavity with intensities given as  $|r|^2 = 70\%$ ,  $|t|^2 = 10\%$  and  $L = 20\%$ .

#### 2.1.4 Cavity losses

In eq. (10) we assume the case of a lossless cavity, i.e. eq. (1) is fulfilled. In practice, any cavity will have some amount of losses, which would have to be

taken into account when calculating the finesse. When losses are present eq. (1) instead generally reads

$$|r|^2 + |t|^2 + L + L' = 1, \quad (18)$$

where  $L$  and  $L'$  indicates the fractional losses of each mirror.

In this case the finesse would be given as

$$\mathcal{F} = \frac{2\pi}{|t|^2 + |t'|^2 + L_{total}}, \quad (19)$$

where  $L_{total} = L + L'$  are the total additional cavity losses.

The effect on the transmission spectrum of a cavity with losses is that the level of the normalized transmission will not reach unity, as some light is lost to e.g. absorption or scattering for each round trip of the cavity. This is shown in figure 5 where the Airy function is shown and compared for examples with  $L = 0$  and  $L = 20\%$ .

## 2.2 The Fano mirror: a sub wavelength grating

### 2.2.1 Reflection/transmission spectra and line shape analysis

#### 2.2.2 Lossless grating

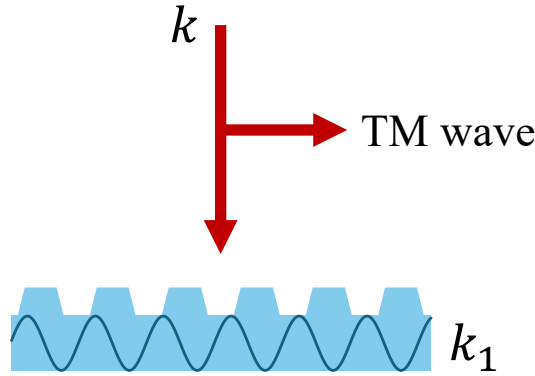


Figure 6: A simple sketch of a sub-wavelength grating with a guided-mode of wave number  $k_1$  and a TM-polarized incident wave of wave number  $k$ . It is illustrated how the sub-wavelength grating acts as an effective  $TM_0$  waveguide for an incident beam with a polarization perpendicular to the grating lines.

We wish to analytically describe the wavelength-dependent spectra for the transmission and reflectivity of an infinite sub-wavelength grating. The wavelength

dependence arises from the fact that any incident light will be subject to interactions with the so-called *guided-mode* of the grating. The grating is, in this way, said to act as an effective  $\text{TM}_0$  waveguide for the resonance that we wish to leverage and study. This is sketched in figure 6.

By first considering the case where absorption and thermal coupling effects are neglected, i.e. a lossless grating, we can assume conservation of energy and thereby the relations

$$|r_g|^2 + |t_g|^2 = 1 \quad \text{and} \quad |r_d|^2 + |t_d|^2 = 1, \quad (20)$$

where the subscripts  $g$  and  $d$  indicate the *grating* and *direct* transmissions and reflectivities, respectively. It is implied that the direct coefficients are constants and describe the transmission and reflectivity when the incident wavelength is significantly detuned from any guided-mode resonance of the grating. Furthermore, it is also implied that the grating coefficients arise from the interaction between the guided-mode and the incident light and are thus functions of the incident wavelength.

We now assume a normal incident beam on the grating as a linearly polarized monochromatic plane wave, with a wavelength close to a guided-mode resonance of the grating. In order to describe the coefficients  $r_g$  and  $t_g$  we follow the formalism presented by Fan and Joannopoulos [33] and consider the likely paths of the incident light through the grating. It is quite intuitive to consider the case where the light is simply transmitted, and this shall be our first case hereafter denoted the *direct pathway*. Another case one might consider is the one where the incident light excites the guided-mode resonance in the grating. This case is denoted the *indirect pathway* and decays more slowly than its direct counterpart.

The interference caused when the guided mode is excited gives rise to a *Fano resonance*, due to its physical similarities to the description of interference between a discrete autoionized state and a bound continuum state first reported by Fano [39]. The cross section of inelastic scattering, when measured as a function of energy, showed characteristic asymmetric peaks. These were described as the aforementioned interference pattern between *direct* (the discrete state) and *indirect* (the continuum state) pathways.

By generalizing the model of Fan and Joannopoulos [33] we describe the trans-

mission and reflectivity coefficient amplitudes as

$$r_g = r_d + \frac{a}{k - k_1 + i\gamma} \quad \text{and} \quad t_g = t_d + \frac{b}{k - k_1 + i\gamma}, \quad (21)$$

where  $k = 2\pi/\lambda$  is the incident wave number,  $k_1 = 2\pi/\lambda_1$  is the wave number according to the guided-mode resonance and  $\gamma$  is the HWHM (half width at half maximum) of the guided-mode resonance. Complex coefficients  $a$  and  $b$  describe the interference between the directly transmitted or reflected waves and the guided mode of the grating.

Note that in eq. (21) the right side of the expression for each coefficient corresponds to the continuum state i.e. the indirect pathway, while the direct transmission and reflection coefficients take the role of the autoionized discrete state, i.e. the direct pathway[39].

As we are dealing with an ideal, lossless, grating, we assume coefficients  $a$  and  $b$  to be equal, meaning that we specifically assume vertical symmetry throughout the grating. By considering eq. (20) this in turn leads to

$$a = b = -i\gamma(t_d + r_d), \quad (22)$$

which further yields an expression for the grating transmission amplitude coefficient on the form

$$t_g = t_d \frac{k - k_0}{k - k_1 + i\gamma}. \quad (23)$$

Here, the newly introduced  $k_0 = 2\pi/\lambda_0 = k_1 - i\gamma(r_d/t_d)$  is the zero-transmission/unity-reflectivity wave number.

To generalize eq. (23) to include non-unity reflectivity and non-zero transmission, we allow for  $a \neq b$ [40][41][42], meaning that the case of vertical asymmetry is included in the model[43]. By assuming  $r_d, t_d \in \mathbb{R}$ , eq. (20) leads to the coupled differential equations

$$\begin{aligned} t_d x_a + r_d x_b &= 0, \quad \text{and} \\ x_a^2 + y_a^2 + x_b^2 + y_b^2 + 2t_d\gamma y_a + 2r_d\gamma y_b &= 0, \end{aligned} \quad (24)$$

where  $\{x, y\}_{a,b}$  respectively denotes the real and imaginary parts of the coefficients  $a$  and  $b$ . Solving eqs. (24) leads to the correct complex reflectivity coefficients and the expression for the transmission coefficient amplitudes now reads

$$t_g = t_d \frac{k - k_0 + i\beta}{k - k_1 + i\gamma}, \quad (25)$$

where  $k_0$  and  $\beta$  are defined from the expression for  $a$  found by solving eqs. (24), given as

$$a = t_d(k_1 - k_0 - i\gamma + i\beta). \quad (26)$$

Finally, this allows for non-zero transmission and non-unity reflectivity at wave number  $k_0$ .

To show the validity of the model at this point, we introduce a periodic grating which is arbitrarily sketched in figure 7. The sketch indicates the period of the grating  $\Lambda$ , the top finger width  $w_t$ , the offset between the finger top and the bottom of the grating  $x$ , the total grating thickness  $t$  and finger depth  $d$ . Furthermore, the grating is patterned on a *silicon nitride (SiN)* membrane of refractive index  $n_{SiN}$ .

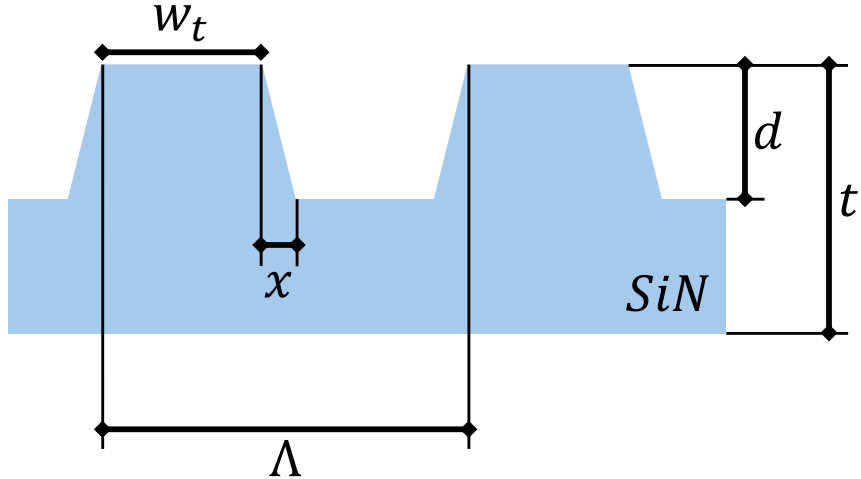


Figure 7: Schematics of a periodic optical *SiN* grating with physical parameters:  $\Lambda = 857\text{nm}$ ,  $w_t = 623\text{nm}$ ,  $d = 55.1\text{nm}$ ,  $t = 152\text{nm}$ ,  $x = 67\text{nm}$ ,  $n_{SiN} = 2.15$ .

In order to simulate the transmission and reflectivity profiles as a function of the incident wavelength, we utilize the *Modeled Integrated Scatter Tool (MIST)* developed by the *National Institute of Standards and Technology (NIST)*[44]. The simulation solves Maxwell's equations for any pre-defined infinite periodic structure.

MIST assumes an incident plane-wave, and hence predicts the *ideal* spectra for the transmission and reflectivity, i.e. zero and unity when on resonance, respectively. In order to include effects related to the Gaussian behaviour of a more realistic incident beam, such as collimation and finite-size effects[45], one would have to solve Maxwell's equations for a Gaussian distribution. We safely

assume an incident plane-wave for reasons related to the order of magnitude for the *Rayleigh range* of the beam used, compared with that of the typical cavity length.

In reality, the interference inside the cavity however cannot be perfect, as any Gaussian beam can be represented by a number rays, infinitesimal in size, which would all track differently through the grating, resulting in non-unity reflectivity and non-zero transmission. In order to phenomenologically model this we scale each transmission value found by MIST according to

$$t_g = (1 - \varepsilon) \cdot t_{MIST} + \varepsilon, \quad (27)$$

where we define the correction to be arbitrarily small as  $\varepsilon = 1\%$ .

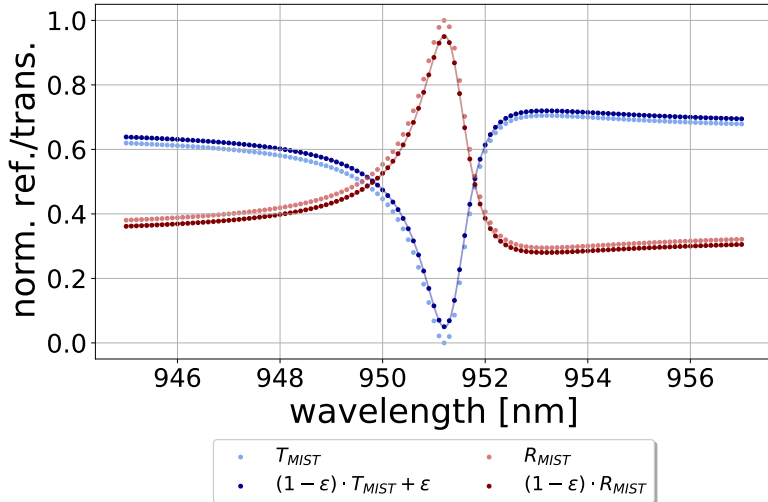


Figure 8: Reflectivity and transmission values (scaled and unscaled) found from a MIST simulation plotted with the corresponding least squares fit to the model in eq. (25). The resulting grating parameters are given as  $\lambda_0 = 951.217\text{nm}$ ,  $\lambda_1 = 951.356\text{nm}$ ,  $t_d = 0.818$ ,  $r_d = 0.527$ ,  $\gamma_\lambda = (\lambda_1^2/2\pi)\gamma = 0.527\text{nm}$ , and  $\beta = 1.03 \cdot 10^{-6}\text{nm}^1$ .

Figure 8 shows the scaled and unscaled results of the simulation using MIST for the following physical grating parameters:

$$\begin{aligned} \Lambda &= 857\text{nm}, \quad w_t = 623\text{nm}, \quad h = 55.1\text{nm}, \\ t &= 152\text{nm}, \quad d = 67\text{nm} \quad \text{and} \quad n_{SiN} = 2.15, \end{aligned} \quad (28)$$

The reflectivity- and (corrected) transmission values were then fitted to the model in eq. (25) using a least squares fitting method, and plotted along with the simulated values. The resulting grating parameters were found as

$$\begin{aligned}\lambda_0 &= 951.208\text{nm}, \quad \lambda_1 = 951.356\text{nm}, \quad t_d = 0.8094, \\ r_d &= 0.527, \quad \gamma_\lambda = 0.527\text{nm} \quad \text{and} \quad \beta = 4.42 \cdot 10^{-7}\text{nm}^1,\end{aligned}\tag{29}$$

where  $\lambda_0$  is the cavity mode resonance wavelength,  $\lambda_1$  is the guided-mode resonance wavelength,  $r_d$  ( $t_d$ ) is the direct reflectivity (transmission),  $\gamma_\lambda$  is the width of the guided-mode resonance and  $\beta$  is a constant associated with non-unity reflectivity and non-zero transmission.

### 2.2.3 Lossy grating

In order to modify the above model such that losses, e.g. due to absorption or thermal coupling effects, are accounted for, we add a resonant loss term to the energy conservation relation in eq. (20). For this we introduce the resonant loss level  $L$ , which must be known in order to accurately calculate the complex reflectivity coefficients. The energy conservation relation is modified such that

$$|t_g|^2 + |r_g|^2 + \frac{c^2}{(k - k_1)^2 + \gamma^2} = 1,\tag{30}$$

where the coefficient  $c^2 = L((k - k_1)^2 + \gamma^2)$  includes the resonant loss term  $L$ . A new set of coupled differential equations are found, using eq. (30), given as

$$\begin{aligned}t_d x_a + r_d x_b &= 0, \quad \text{and} \\ x_a^2 + y_a^2 + x_b^2 + y_b^2 + c^2 + 2t_d \gamma y_a + 2r_d \gamma y_b &= 0.\end{aligned}\tag{31}$$

It is easily identified that eq. (24) and eq. (31) differ only by the addition of coefficient  $c^2$ , and thereby the losses. Solving eq. (31) leads to the correct complex reflectivity coefficients, except that they now account for any losses associated with the grating.

In conclusion, the complete grating model consists of an expression for the transmission coefficients and a set of coupled differential equations for the reflection coefficients, shown in eq. (25) and eq. (31), respectively. The model on the form used for this project and subsequent thesis is derived in previous work by A. Darki et al. [46] and more recently T. Mitra et al. [35].

Figure 9 shows reflection and transmission spectra of a grating of parameters given in eq. 29 with a synthetic non-zero resonance loss term in order to show

the effect of including losses. It is seen from the added *loss curve* that the losses increase when approaching the resonance wavelength, as the interaction with the guided-mode, and thus the grating, gets stronger in this region.

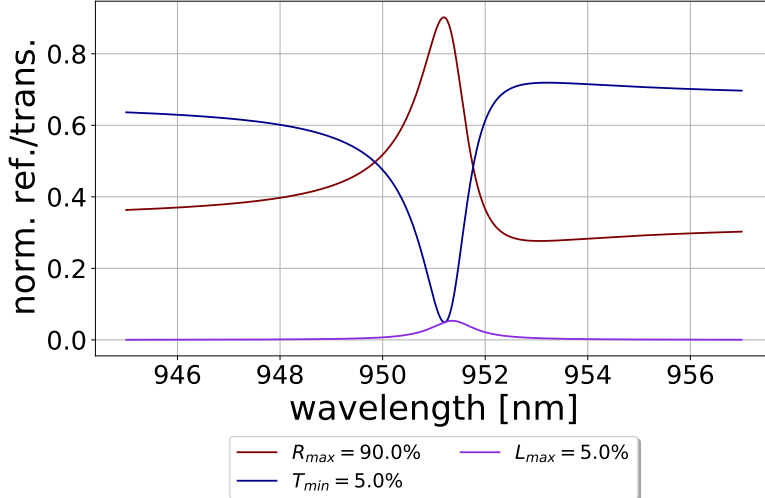


Figure 9: Simulated reflectivity and transmission spectra of a grating of parameters given in eq. (29) with a synthetically added non-zero resonant loss term. The purple line indicate the corresponding grating losses.

## 2.3 The single Fano cavity

### 2.3.1 The single Fano cavity model

The single Fano cavity consists of a planar broadband mirror, and a sub-wavelength grating, i.e. a Fano mirror, as described in section 2.2 and seen in figure 10 where schematics of the single Fano and broadband cavity configurations are shown. While the broadband mirror has fixed optical properties, the Fano mirror has transmission and reflection coefficients dependent on the incident wavelength, according to solutions to the coupled differential equations of eq. (31).

In order to model the single Fano cavity transmission spectra, we therefore consider the transmission function of a normal incident and planer Fabry-Perot cavity in eq. (3) with  $r, t \rightarrow r_m, t_m$  and  $r', t' \rightarrow r_g(\lambda), t_g(\lambda)$ [47]. Here the subscript  $m$  indicates the broadband *mirror* coefficients, and  $g$  is for *grating*, which indicates the coefficients of the Fano mirror. Rewriting eq. (3) such that

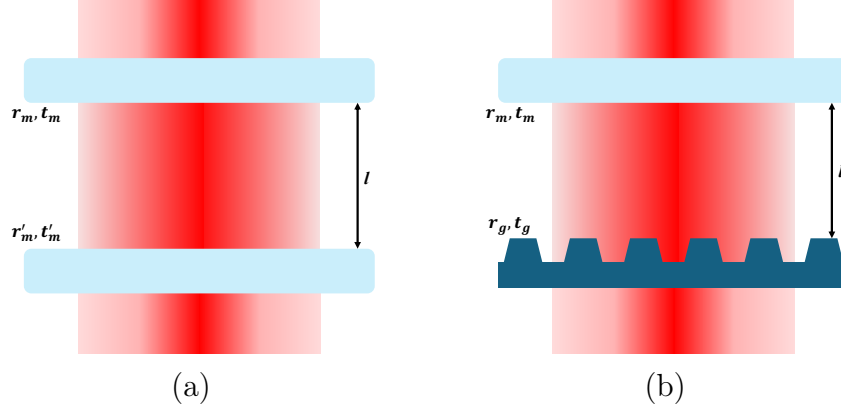


Figure 10: In (a) is seen the schematics of a cavity consisting of two broadband mirrors with transmission and reflectivity coefficients  $t_m$ ,  $r_m$ ,  $t'_m$ , and  $r'_m$ . (b) shows the schematics of a single Fano cavity consisting of one broadband mirror with coefficients  $t_m$ ,  $r_m$  and one Fano mirror with wavelength dependent coefficients  $t_g$ ,  $r_g$ . The reflectors in either cavity are separated by a cavity length  $l$ .

it describes the normalized transmission amplitude, through the single Fano cavity,  $T_{cav} = |E_{out}|^2 / |E_{0,in}|^2$  we get

$$T_{cav} = \left| \frac{t_m t_g(\lambda) e^{i\phi}}{1 - r_m r_g e^{2i\phi}} \right|^2, \quad (32)$$

where  $\phi = 2\delta = kl$ ,  $k = 2\pi/\lambda$  and  $l$  is the cavity length, as is consistent with the general case described in section 2.2.

### 2.3.2 Transmission linewidth

We aim to analytically describe how the transmission spectrum at, or close to, the overall resonance behaves as a function of the incident wavelength. The overall resonance is the term used for the case of  $\lambda_g \approx \lambda_c \approx \lambda_l$ , where  $g, c, l$  stands for grating/guided-mode, cavity and laser, respectively, and the Fano model is hence generalized for this specific scenario. Considering the case where the cavity resonance closely resembles the guided-mode resonance of the Fano mirror (the zero-transmission wavelength), eq. (32) can be approximated well by

$$T_{cav} \approx \frac{A}{1 + \left( \frac{\Delta}{1-\nu\Delta} \right)^2}, \quad (33)$$

where  $\Delta = (\lambda - \lambda_c)/\delta\lambda$  is the detuning from the cavity resonance normalized by the HWHM  $\delta\lambda$ , and  $\nu$  is a constant describing the asymmetry of the single

Fano transmission spectrum. [35][46]

From eq. (33) it can be shown that the HWHM of the Fano transmission profile around the overall resonance wavelength, i.e. when  $\lambda_c \approx \lambda_0$ , is approximately given as

$$\delta\lambda \approx \frac{1}{\frac{1}{\delta\lambda_c} + \frac{1}{\delta\lambda_g}}, \quad (34)$$

where

$$\delta\lambda_c = \frac{\lambda_0^2}{8\pi l} (|t_g(\lambda_0)|^2 + |t_m|^2 + L) \quad (35)$$

is the HWHM of a broadband cavity and

$$\delta\lambda_g = \frac{\gamma\lambda}{2(1 - r_d)} (|t_g(\lambda_0)|^2 + |t_m|^2 + L) \quad (36)$$

is the HWHM of the Fano cavity in the so-called Fano regime.[35][46] In eqs. (34)-(36)  $\lambda_0$  is the Fano cavity resonance wavelength,  $l$  is the cavity length,  $L = (1 - |r_g(\lambda_0)|^2 - |t_g(\lambda_0)|^2)$  is the total additional losses of the cavity when on resonance,  $\gamma\lambda$  is the width of the guided-mode resonance of the Fano mirror and  $r_d$  is the off-resonance, or *direct*, reflectivity of the Fano mirror.

The *Fano regime* and its counterpart the so-called *standard regime* are defined for a given single Fano cavity, by its length  $l$ . By inspection of eqs. (35) and (36) it is seen that for  $l \rightarrow \infty$  the linewidth in eq. (34) is dominated by the broadband cavity term, while for the opposite case,  $l \rightarrow 0$ , the linewidth is predominantly given by the Fano cavity term.

Generally the Fano regime describes the cavity lengths for which eq. (34) shows a significant divergence from the broadband linewidth in eq. (35). Oppositely, when in the standard regime the broadband and Fano cavity produces resonance transmission peaks of comparable, if not equal, linewidths.

We now introduce a single Fano cavity consisting of the Fano mirror introduced in section 2.2 and sketched in figure 7, and a broadband mirror of reflectivity  $|r|^2 = 90\%$  and transmission  $|t|^2 = 1\%$ . Figures 11a and 11b depicts examples of the transmission spectra in the standard and Fano regimes together with their respective corresponding broadband cavity transmission profiles. The reflectivity of the Fano mirror is shown in both figures.

Figure 11a shows the transmission spectra of the two cavities for a length of  $l \approx 1000\mu m$ , i.e. in the standard regime. It is clear from inspection of the figure

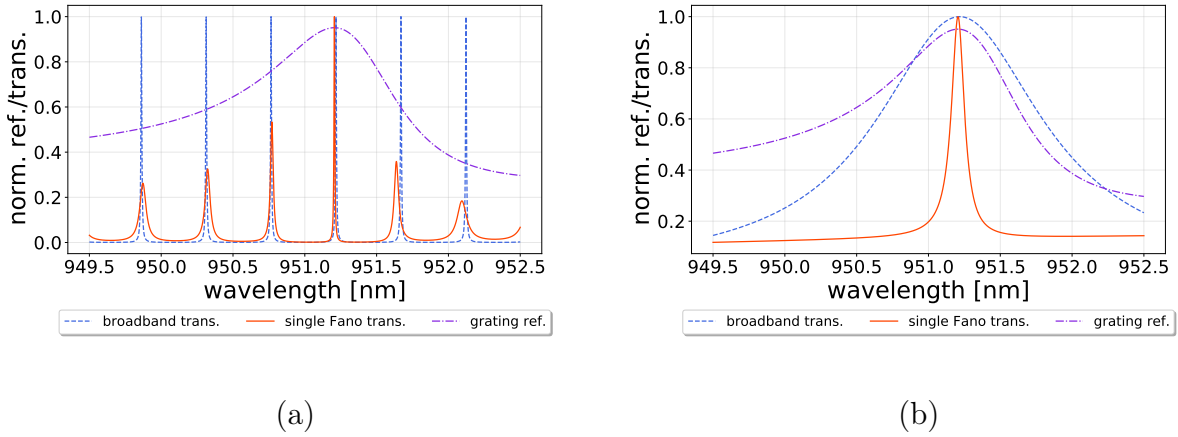
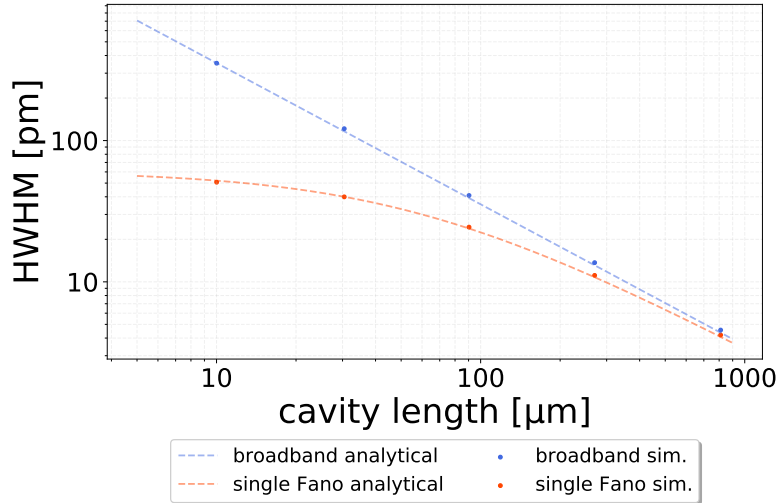


Figure 11: In (a) is seen the comparison of broadband and single Fano cavity transmission spectra for a cavity length of  $l \approx 1000\mu\text{m}$ , i.e. in the *standard* regime. (b) shows the same comparison, but for a cavity length of  $l \approx 5\mu\text{m}$ , i.e. in the so-called *Fano* regime.

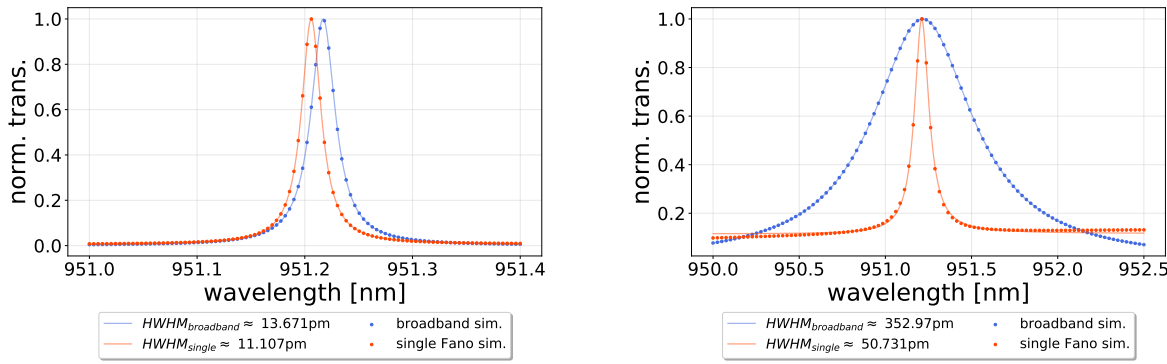
that the resonance transmission profile of the standard broadband cavity is not wavelength dependent, in the sense that all fringes appear to have the same high finesse  $\mathcal{F}$ , i.e. ratio between the FSR and HWHM. This is not the case for the Fano cavity which is due to the wavelength dependence of the optical properties of the Fano mirror, as this causes the transmission and reflectivity to *only* match those of the broadband mirror when on resonance. Furthermore, no significant difference in linewidth is seen for the transmission of the two cavities on resonance, as predicted by eq. (34).

In figure 11b, the transmission spectra of both cavities are shown for a length of  $l \approx 5\mu\text{m}$ , i.e. in the Fano regime. Here it is clearly seen that while the standard cavity, as expected, experiences broadening for shorter cavity lengths, this is not the case for the Fano cavity transmission peak.

Figure 12a models the behavior of the linewidth of the single Fano cavity compared with the one for a broadband cavity of similar optical properties, as a function of wavelength. Here it is easily seen where the linewidth of the single Fano transmission begins to saturate, and hence deviate from the one of the broadband cavity. The plotted line in the figure is calculated using eq. (34) while the points depict linewidths found as a fitting parameter from a least squares fit of the general Fano model in eq. (33) to transmission spectra simulated by the Fabry-Perot (eq. (3)) and single Fano (eq. (32)) transmission functions. Finally, it can be concluded that the approximate analytical expression for the



(a)



(b)

(c)

Figure 12: (a) shows the approximate analytical resonance linewidths (eq. (34)) as a function of cavity length for the broadband and single Fano cavities together with linewidths of transmission profiles simulated using eq. (32) and eq. (3), found as parameters of least squares fits, for comparison. In (b) and (c) is seen transmission spectra of broadband and single Fano cavities of lengths  $\sim 270\mu\text{m}$  and  $\sim 10\mu\text{m}$ , respectively. The spectra shown indicate each their respective linewidths, and are examples of the values plotted in (a). The spectra used to determine the points in (a) can be found in Appendix C.

linewidth of the broadband and single fano cavities in eq. (34) correlates very well with the values found from the simulated spectra.

## 2.4 The double Fano cavity

### 2.4.1 The double Fano cavity model

We now consider a *double Fano cavity* consisting of two Fano mirrors, or sub-wavelength gratings. The schematics of this configuration is shown together with the one for the single Fano cavity in figure 13.

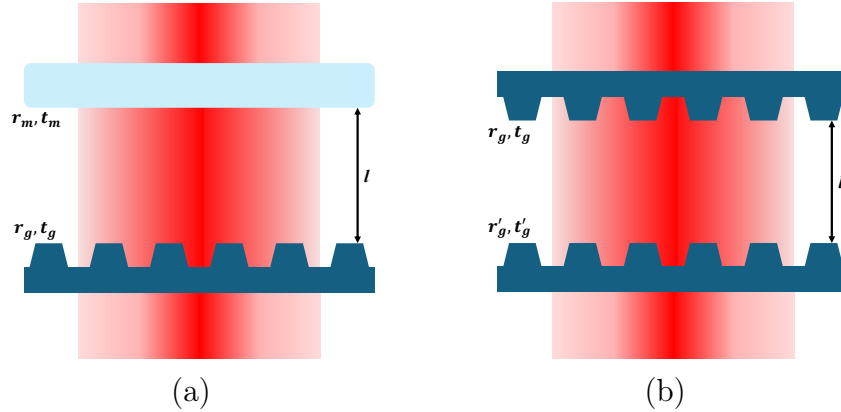


Figure 13: (a) shows schematics of the single Fano cavity consisting of a broadband mirror with transmission and reflectivity coefficients  $t_m, r_m$  and a Fano mirror with coefficients  $t_g, r_g$ . (b) shows the schematics of the double Fano cavity consisting of two Fano mirrors with coefficients  $t_g, r_g, t'_g, r'_g$ . Both cavities have lengths denoted  $l$ .

Here it is evident that instead of having one set of reflectivity and transmission coefficients that depend on the incident wavelength, we now have two. In order to model the transmission of the double Fano cavity, we once again consider the transmission function for the normal incident and planar Fabry-Perot cavity in eq. (3), this time with  $r, t \rightarrow r_g(\lambda), t_g(\lambda)$  and  $r', t' \rightarrow r'_g(\lambda), t'_g(\lambda)$ [47]. We rewrite the Fabry-Perot transmission function with the addressed substitutions of the optical coefficients and such that it describes the normalized transmission amplitudes  $T_{cav} = |E_{out}|^2/|E_{0,in}|^2$  and get

$$T_{cav} = \left| \frac{t_g(\lambda)t'_g(\lambda)e^{i\phi}}{1 - r_g(\lambda)r'_g(\lambda)e^{2i\phi}} \right|^2. \quad (37)$$

We now introduce a double Fano cavity consisting of two identical Fano mirrors, each as sketched in figure 7 in section 2.2, and thus with optical parameters given in eq. (29). Figure 14 shows an example of the normalized transmission spectrum of this double Fano cavity on- and off-resonance for a cavity length of  $l \approx 30\mu m$ . The spectrum was found using eq. (37).

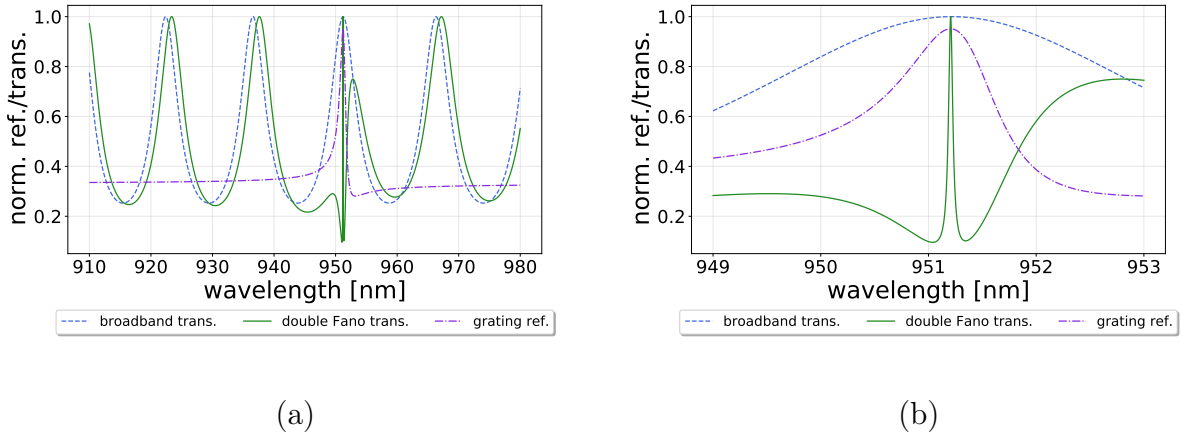


Figure 14: An example of a normalized double Fano transmission spectrum of a cavity of length  $l \approx 30\mu m$ . (a) shows a long-range wavelength scan, depicting both the on- and off-resonance behaviour of the double Fano cavity transmission. Note that the off-resonance spectrum perfectly resembles the transmission of a low-finesse Fabry-Perot cavity with optical amplitude coefficients given by the direct transmission  $t_d$  and reflectivity  $r_d$  of the Fano mirror used, only displaced by a small phase. This is shown as a blue dashed line in (a). (b) shows the transmission focussed specifically around the resonance wavelength. Both examples are shown together with the reflectivity of the Fano mirror used to model them.

#### 2.4.2 Transmission linewidth

In order to describe the analytical linewidth of the transmission profile of the double Fano cavity, we take a similar approach as in the single Fano case outlined in section 2.3.2. It can be shown from eq. (34) when including the wavelength dependence of the optical coefficients of both Fano mirrors, that the HWHM  $\delta\lambda$  of the double Fano cavity transmission profile is approximately given as

$$\delta\lambda^{double} \approx \frac{1}{\frac{1}{\delta\lambda_c} + \frac{1}{\delta\lambda_g^{double}}}, \quad (38)$$

where

$$\delta\lambda_c = \frac{\lambda_0^2}{8\pi l} (|t_g(\lambda_0)|^2 + |t'_g(\lambda_0)|^2 + L) \quad (39)$$

is still the HWHM of a broadband cavity and

$$\delta\lambda_g^{double} = \frac{\gamma_\lambda}{4(1 - r_d)} (|t_g(\lambda_0)|^2 + |t'_g(\lambda_0)|^2 + L). \quad (40)$$

is the HWHM of the double Fano cavity in the Fano regime. Note that  $\delta\lambda^{double} = \delta\lambda^{single}/2$  for  $l \rightarrow 0$  when eq. (38) is predominantly given by eq. (40). In this brief evaluation of the estimated analytical linewidth of the double Fano transmission profile it is assumed that all defining parameters of the two Fano mirrors are identical, except for the cavity and guided-mode resonance wavelengths  $\lambda_{0,1}$ . Namely the following relevant parameters are assumed identical,

$$r_d = r'_d \text{ and } \gamma_\lambda = \gamma'_\lambda. \quad (41)$$

In this way any spectral detuning of the two Fano mirrors used to make a cavity is included in the analytical expression. The spectral detuning, and the effect hereof, will be further described in section 2.4.5.

### 2.4.3 Single and double Fano cavity comparison

Using the analytical expression for the double Fano cavity transmission in eq. (38) we are now in a position to compare the single and double Fano cavities. Note that we at this point only consider the ideal case of the double Fano cavity where additional cavity losses are neglected and the two Fano mirrors used are identical, i.e. the cavity is said to be *symmetrical*. The additional cavity losses are explicitly set to be given as

$$L = 1 - |r_g|^2 - |t_g|^2 = 0. \quad (42)$$

Figure 15 shows the transmission of the ideal double Fano cavity and the corresponding single Fano cavity for comparison.

Figures 15a and 15b shows the transmission for a cavity length of  $l \approx 1000\mu m$  which is well-inside the standard regime outlined in section 2.3.2, where the standard, broadband and single Fano cavities produce transmission spectra of roughly identical linewidths. In this regime, due to the  $1/l$  proportionality of the FSR, the off-resonance behavior of the double Fano cavity transmission is visible in the range plotted. It is seen that the transmission at each cavity resonance reaches a normalized transmission of  $|E_{out}|^2/|E_{0,in}|^2 = 1$ . This is due to the fact that the two Fano mirrors, while they have wavelength dependent transmission and reflectivity coefficients, always have identical ones for the ideal case. This maximizes the Fabry-Perot transmission function and ensures unity transmission at any cavity resonance. The minimum level of the cavity changes according to the coefficient of finesse, and thus only the Fano mirror reflectivity, hence the HWHM also changes as we move further from the guided-mode resonance.

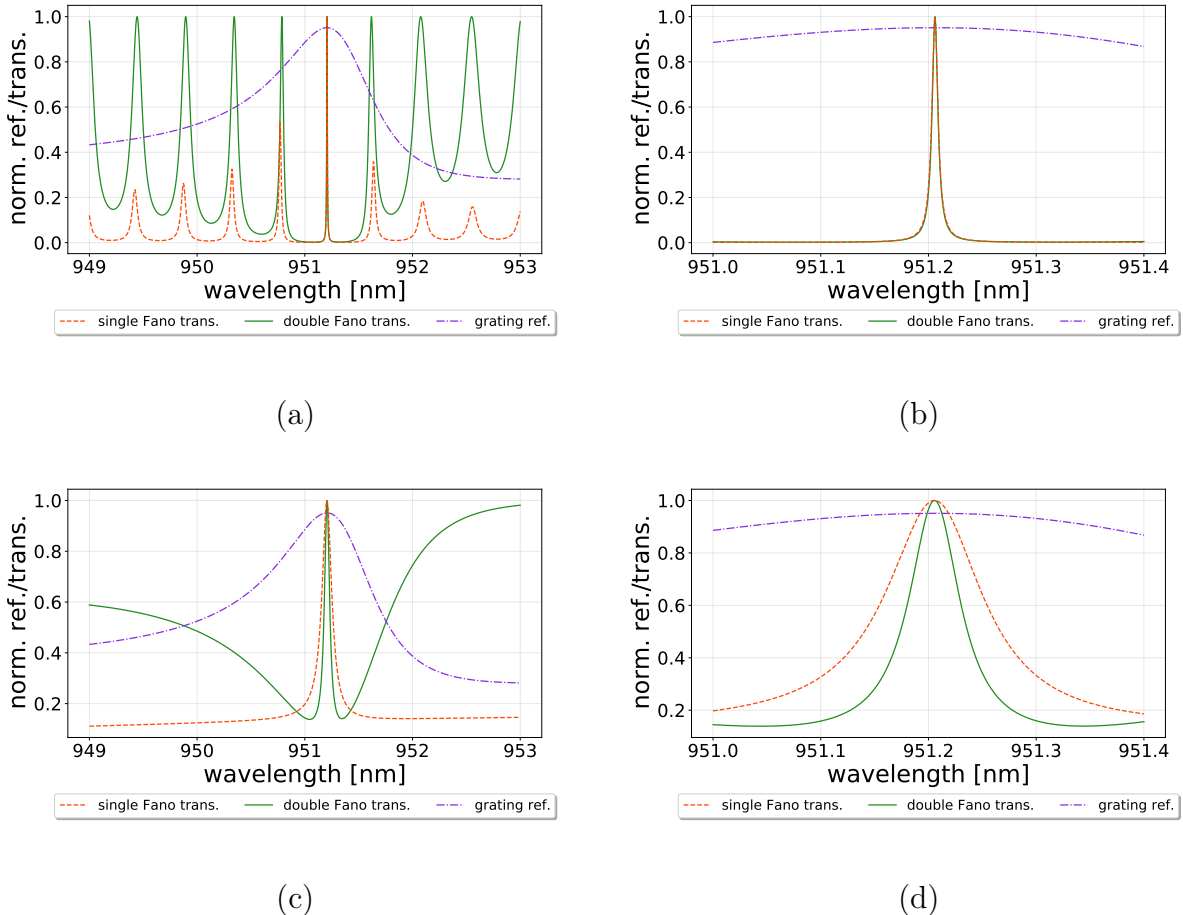
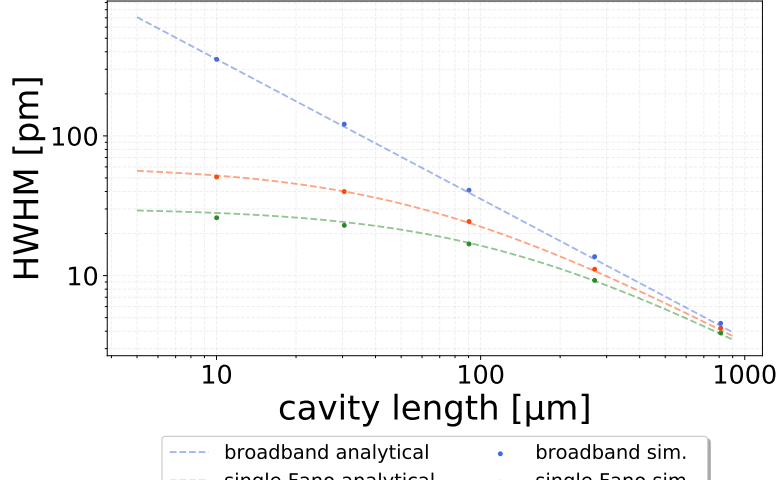


Figure 15: Comparison of the single and double Fano transmission spectra in the *standard* and *Fano* regimes. (a) and (b) shows the spectral comparison for a cavity of length  $l \approx 1000\mu\text{m}$ , i.e. in the *standard* regime, while (c) and (d) shows the same for a cavity of length  $l \approx 5\mu\text{m}$ , i.e. in the *Fano* regime. (b) and (c) show spectra zoomed around the resonance peak, and the Fano mirror reflectivity is depicted in all figures.

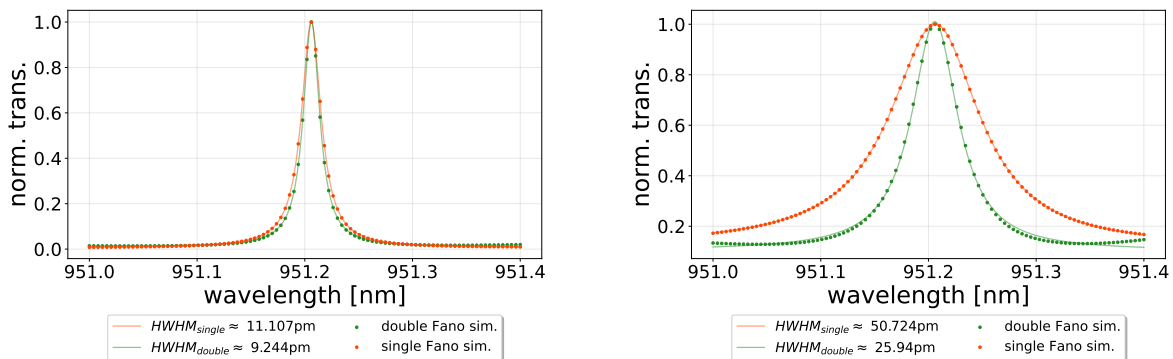
Both the minimum transmission level and the HWHM converge when moving away from the resonance wavelength, when  $r \rightarrow r_d$  becomes constant.

Figures 15c and 15d shows the transmission of a double Fano cavity of length  $l \approx 5\mu\text{m}$ , i.e. well within the Fano regime. It is seen that the double Fano cavity transmission produces a resonance peak with a HWHM narrower than the one for the single Fano cavity, as is predicted in eq. (40). Furthermore, the immediate off-resonance behavior of the double Fano cavity transmission in the Fano regime, is drastically different than for the single Fano cavity. This is due to the collective higher transmission in this region compared with the

single Fano case where the broadband mirror has a constant, and often high, reflectivity and hence a correspondingly low transmission.



(a)



(b)

(c)

Figure 16: (a) shows the analytical resonance linewidths (eqs. (34), (38), and (35)) as a function of the cavity length for the broadband, single and double Fano cavities together with linewidths of corresponding profiles simulated using eqs. (32), (37), and (3) for comparison. In (b) and (c) is seen transmission spectra of single and double Fano cavities of lengths  $l \approx 270\mu m$ , and  $l \approx 10\mu m$ , respectively. The spectra shown indicate each their respective linewidths, and are examples of the values plotted in (a). Note however, that the broadband cavity peak has been left out of (b) and (c). The spectra used to determine the points in (a) can be found in Appendix D.

Figure 16a shows the analytical linewidth calculated and compared for the broadband, single Fano, and double Fano cavities, calculated using eqs. (35), (34), (38). These are compared with linewidths found as fitting parameters from a least squares fit of the general Fano transmission formula given in eq. (33) to transmission spectra calculated using eqs. (3), (32), and (37). According to eq. (38) the linewidth of the double Fano cavity transmission should converge to exactly half that of the single Fano cavity, meaning that

$$\delta\lambda_{double} = \frac{\delta\lambda_{single}}{2}, \quad \text{for } l \rightarrow 0. \quad (43)$$

This is supported well by the simulation depicted in figure 16a.

Figures 16b and 16c contain examples of transmission spectra of single- and double Fano cavities and corresponding least squares fits to the general Fano model in order to determine their linewidths.

#### 2.4.4 Additional cavity losses

Thus far we have only examined a lossless double Fano cavity where

$$|r_g|^2 + |t_g|^2 = 1 \quad (44)$$

is fulfilled for both Fano mirrors used to construct the cavity.

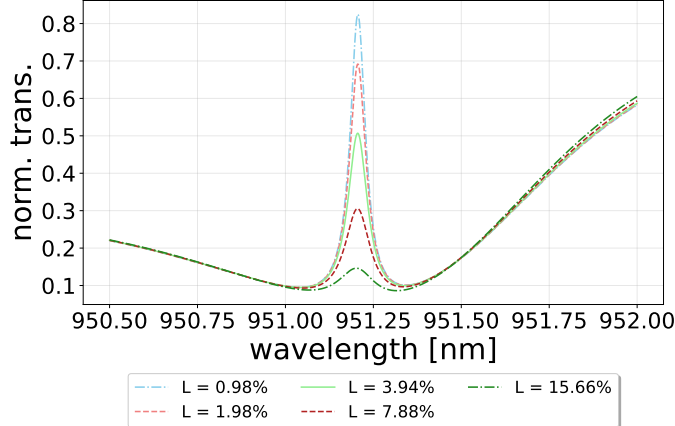


Figure 17: Resonant transmission spectra for different values of the additional resonant loss term  $L$ , of a symmetric double Fano cavity of length  $l \approx 30\mu\text{m}$ .

In this section we will investigate what happens when we introduce *additional* cavity losses, not to be confused with the often used definition of cavity losses

defined as  $L = 1 - |r|^2$  where anything not being reflected back into the cavity is considered as "losses". Additional cavity losses, as described in this section, is given as

$$L = 1 - |r_g|^2 - |t_g|^2. \quad (45)$$

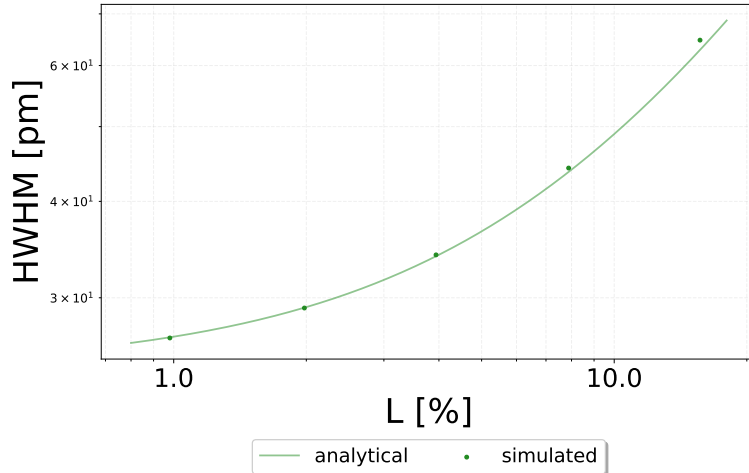
Figure 17 shows double Fano transmission spectra for a symmetric cavity with varying values for the additional cavity losses. It is readily seen that the maximum value reached in each spectrum is rapidly reduced with the introduction of these losses.

Since the linewidth is defined as the HWHM of the transmission profile, this will naturally vary as a function of additional cavity losses. This is depicted in figure 18a where the HWHM is shown for different values of  $L$ . Examples of transmission spectra taken for different values of  $L$  are shown in figures 18b and 18c, along with their respective least squares fits to the general Fano model in eq. (33) and linewidths found as fitting parameters hereof.

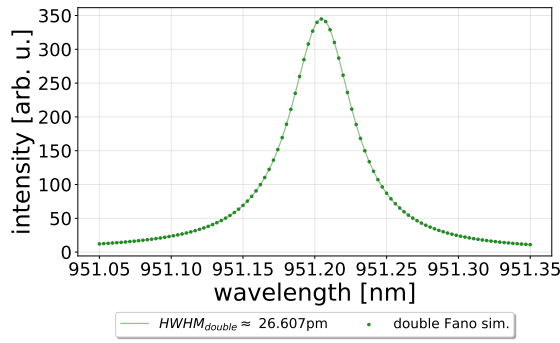
Figure 18a shows the simulated linewidths of resonance transmission spectra as a function of the total additional cavity losses  $L$ , and is compared with the analytical formula for the double Fano linewidth in eq. (38).

#### 2.4.5 Spectral detuning (lossless)

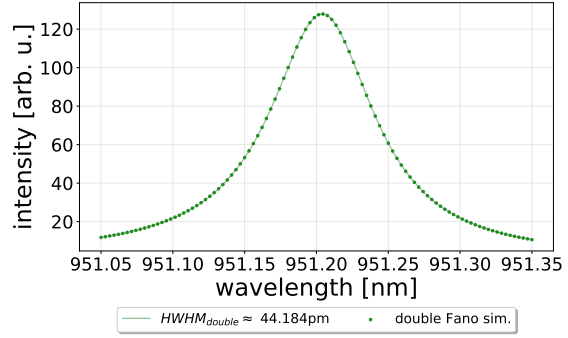
Up until this point, it has been assumed that the Fano mirrors making up the double Fano cavity have been identical, namely the cavity has been *symmetrical*. However, in practice this is very unlikely to be the case, as any Fano mirror constructed is bound to have some uncertainties attached to the physical parameters describing it (see eq. (28)). For that reason we investigate the effect of an *assymmetric* cavity on the resulting transmission profile. Here we remember that each Fano mirror is described by a set of parameters,  $\lambda_0$ ,  $\lambda_1$ ,  $t_d$ ,  $\gamma\lambda$  and  $\beta$ , which respectively describe the cavity resonance wavelength, guided-mode resonance wavelength, direct transmission, guided-mode resonance linewidth and additional losses of each grating. In order to model only a spectral detuning, we therefore simply change the parameters regarding the cavity and guided-mode resonance wavelengths,  $\lambda_0$  and  $\lambda_1$  by an amount corresponding to the detuning we wish to study. For this section the parameters will be given by the ones for the Fano mirror sketched in figure 7, and thus given in eq. (29) for the



(a)



(b)



(c)

Figure 18: (a) shows the linewidth (HWHM) of a symmetric double Fano cavity of length  $l \approx 30\mu m$  as a function of additional cavity losses  $L = 2(1 - |r_g|^2 - |t_g|^2)$ . Each point is found as a fitting parameter of a least squares fit of the double Fano intracavity spectrum (eq. (6)) for a certain value of  $L$  to the general Fano model. The plotted line indicates the analytical value of the linewidth (eq. 34) as a function of  $L$ , for comparison. In (b) and (c) are seen examples of double Fano transmission spectra, with their respective linewidths, for cavities of  $L = 1\%$  and  $L = 8\%$ , respectively. The spectra used to determine the points in (a) can be found in Appendix E.

unchanged Fano mirror, and

$$\begin{aligned} \lambda'_0 &= \lambda_0 + \Delta, \quad \lambda'_1 = \lambda_1 + \Delta, \quad t'_d = t_d, \\ \gamma'_\lambda &= \gamma_\lambda \quad \text{and} \quad \beta' = \beta \end{aligned} \tag{46}$$

for the *detuned* Fano mirror, where  $\Delta$  is the detuning given by  $\Delta = |\lambda_0 - \lambda'_0|$ . Figure 19 shows the normalized reflectivity and transmission spectra of the unchanged Fano mirror (eq. (29)) and the detuned Fano mirror (eq. (46)) for a detuning of  $\Delta = 0.3\text{nm}$ .

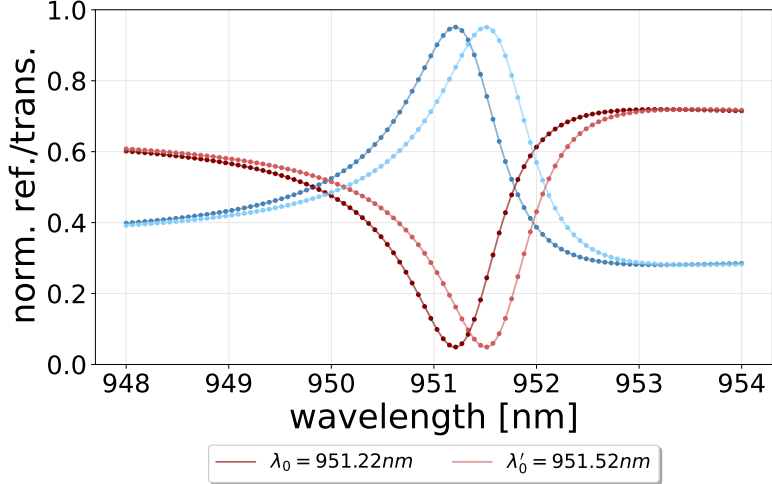


Figure 19: The normalized reflectivity and transmission spectra of the Fano mirrors described in eqs. (29) and (46) for detuning  $\Delta = 0.3\text{nm}$ .

As has been observed in previous sections, the Fano resonance transmission peak is present at the point where the grating reflectivity  $r_g(\lambda)$  is maximized and transmission  $t_g(\lambda)$  minimized. However, when  $\lambda_0 \neq \lambda'_0$  and  $\lambda_1 \neq \lambda'_1$ , this is no longer a trivial conclusion to draw. The question of whether the cavity resonance should be tuned to match the guided-mode resonance wavelength of one grating or the other, or maybe somewhere in between does not have an obvious answer. This will be further expanded upon later in section 2.4.6, but in order to move forward with the investigation of the spectral detuning we, for now, accept that the optimal cavity length, is the one corresponding to a cavity resonance  $\lambda_t$  given, exactly between the two guided-mode resonance wavelengths, as

$$\lambda_t = \frac{\lambda_0 + \lambda'_0}{2}. \quad (47)$$

Where  $t$  is for *transmission* as this is, later on, to be used experimentally as the *transmission wavelength*.

Figure 20 shows the transmission spectrum of a detuned double Fano cavity with parameters corresponding to the transmission and reflectivity spectra in figure

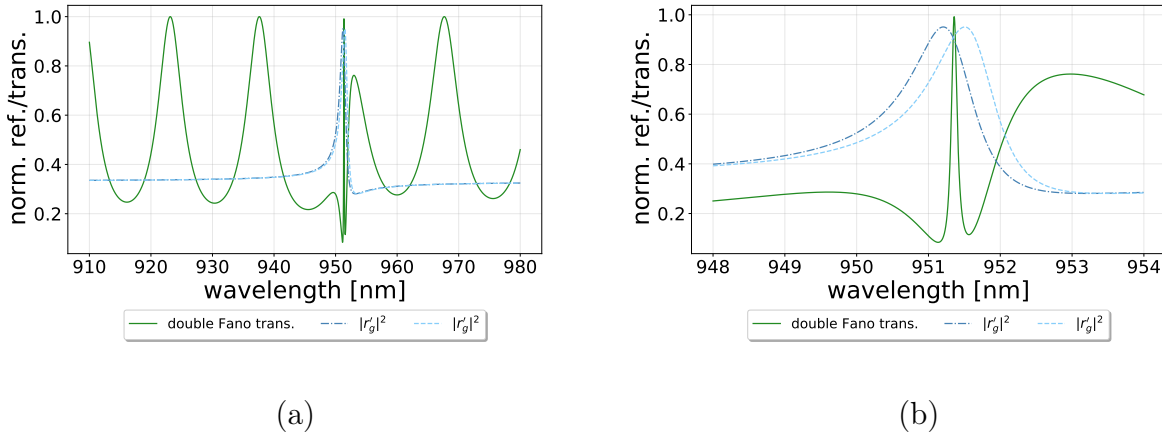


Figure 20: The double Fano transmission spectra of a cavity of length  $l \approx 30\mu m$  and detuned by  $\Delta = 0.3\text{nm}$ , as seen in figure 19, together with the reflectivity spectra of the Fano mirrors used for the simulation.

19, meaning that  $\Delta = 0.3\text{nm}$ . The transmission wavelength  $\lambda_t$  is chosen such that eq. (47) is fulfilled, and correspondingly it is seen that the transmission peak is placed exactly between the maximum (minimum) reflectivities (transmissions) of the two grating, i.e. between the two guided-mode resonance wavelengths. Furthermore, it can be concluded that the detuning is chosen such that the overlap between the guided-mode resonances is still substantial enough for them to couple and hence for the overall Fano resonance to be excited.

While knowing that a detuning of  $0.3\text{nm}$  is acceptable in terms of exciting the Fano resonance in the lossless case is a nice result, it does not provide much in terms of estimating the acceptable detuning for any experimental purposes. In figure 21a the double Fano transmission is shown for increasing detuning  $\Delta$  and transmission wavelength  $\lambda_t = (\lambda_0 + \lambda'_0(\Delta))/2$ .

It is readily seen that with increasing positive detuning, relative to the resonant wavelength of the unchanged Fano mirror, that the peak shifts to higher wavelengths. This in itself is easily seen from eq. (47), but it is apparent from the figure that the linewidth also increases with the detuning. Figure 21b shows the intracavity spectra corresponding to the transmission spectra in figure 21a, and provides valuable insight into the mode density inside the cavity for different values of  $\Delta$ . It is clearly demonstrated by the two figures that the spectral overlap is a very crucial parameter of the double Fano cavity, and is paramount in describing the cavity's ability to sustain the Fano resonance.

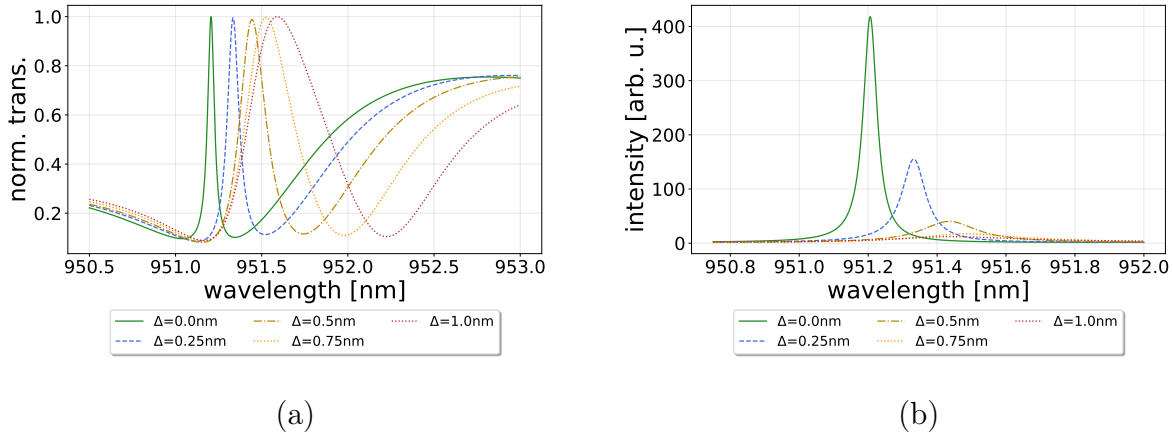


Figure 21: In (a) is seen lossless double Fano transmission spectra for increasing value of the detuning  $\Delta = |\lambda_0 - \lambda'_0|$ . It is readily seen that the transmission wavelength  $\lambda_t = (\lambda_0 + \lambda'_0)/2$  becomes higher, and that the linewidth likewise becomes larger with increasing detuning. (b) shows the intracavity spectra (eq. (6)) corresponding to the transmission spectra in (a) normalized by each their maximum value, shown in (c), in order to preserve readability.

#### 2.4.6 Spatial detuning (lossless)

As mentioned above in section 2.4.5, any spectral detuning gives rise to the potential of a spatial detuning as  $2l = m\lambda$  must be fulfilled for any sustained plane-wave mode inside a normal incident optical cavity. We denote the length corresponding to the resonance wavelength of the unchanged Fano mirror as simply  $l$ , while the one for the detuned Fano mirror will be denoted as  $l'$ . Previously we assumed that the optimal length of a detuned double Fano cavity is the one where the so-called transmission wavelength is given as

$$\lambda_t = \frac{\lambda_0 + \lambda'_0}{2}. \quad (48)$$

And while this does turn out to be a good empirically justified assumption in the experimental part of this project, we will model and investigate the resonant length-dependence of the linewidth of the Fano resonance profile.

Figure 22 shows double Fano resonance transmission profiles plotted for varying cavity length  $l \rightarrow l'$  with detuning  $\Delta = 0.1\text{nm}$ . The long range wavelength scan in figure 22a shows a well-defined off-resonance behavior, as the detuning is barely visible on this scale, while the peak height on resonance is already visibly affected. The immediate off-resonance spectra also shows visible changes

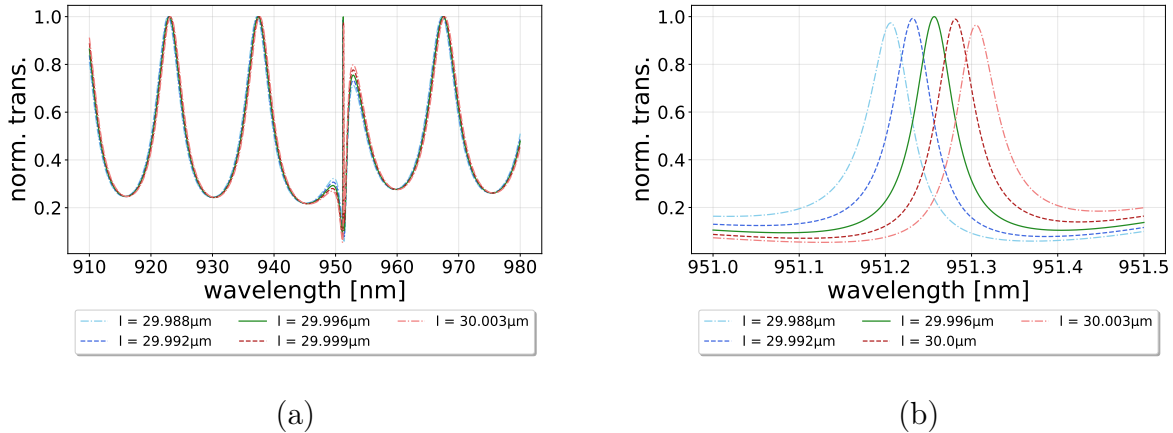


Figure 22: (a) shows lossless long-range transmission spectra of double Fano cavities of lengths  $l \rightarrow l' \approx 30\mu\text{m}$  with  $\Delta = 0.1\text{nm}$ . (b) shows the same spectra as seen in (a), zoomed in on the range around the transmission wavelength  $\lambda_t$ .

as the peak "background" level depend heavily on the location of the overall resonance.

Figure 22b shows the same spectra, but enhanced around the resonance wavelength. This shows that the substantial guided-mode overlap, and thus small detuning, is enough to detect significant changes in the resonance spectra. The shifting of the peak position is evident, but the most prominent change is seen in the peak height, which is reduced from 1 when  $\lambda_t = (\lambda_0 + \lambda'_0)/2$  to around 0.8 when  $\lambda_t = \lambda_0$  or  $\lambda_t = \lambda'_0$ .

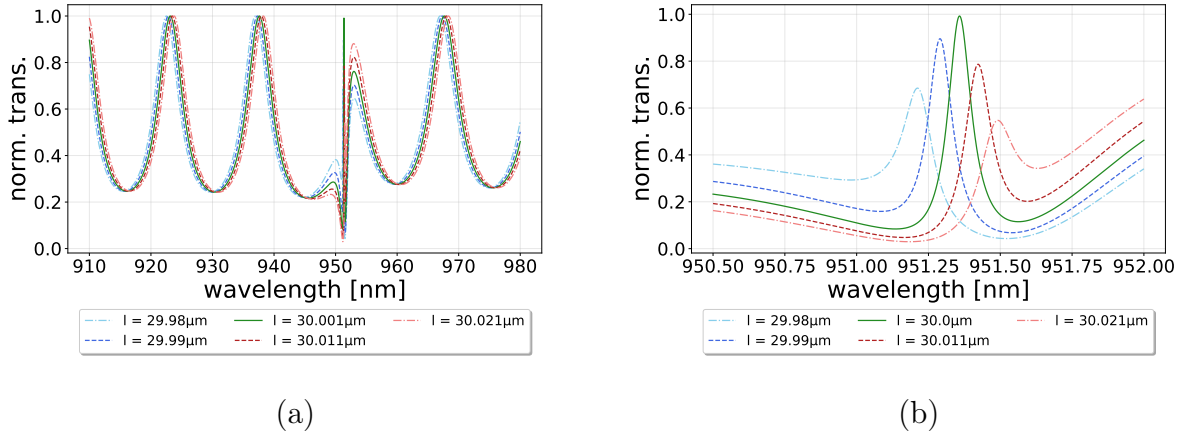


Figure 23: (a) shows lossless long-range transmission spectra of double Fano cavities of lengths  $l \rightarrow l' \approx 30\mu\text{m}$  with  $\Delta = 0.3\text{nm}$ . (b) shows the same spectra as seen in (a), zoomed in on the range around the transmission wavelength  $\lambda_t$ .

Figure 23 shows similar transmission profiles as in figure 22, only with an increased detuning of  $\Delta = 0.3\text{nm}$ . Looking at the long range scan in figure 23a and comparing with the one in figure 22a, it is seen that the displacement of the off-resonance Fabry-Perot like fringes have increased with the slightly higher detuning. This is not surprising as the Fabry-Perot cavity modes, like any other interference pattern inside a cavity must fulfill the brightness identity  $2l = m\lambda$ . Furthermore, the immediate off-resonance regime shows an increase in the intensity displacement when compared with the less detuned example.

Figure 23b, which shows the spectra enhanced around the resonance position, provides a more detailed image of what happens to the transmission profiles as a function of the cavity length. Here it is seen that the peaks at the edges of the length interval have varied even more in shape, height and linewidth than in figure 23b. In short, the increased detuning has also increased the fractional length-dependence of the double Fano cavity transmission profile. Here it must however be noted here that the range in which the cavity length is scanned is increased with the detuning. So the length-dependence is fractional in the sense that the step size is here defined by the size of the interval.

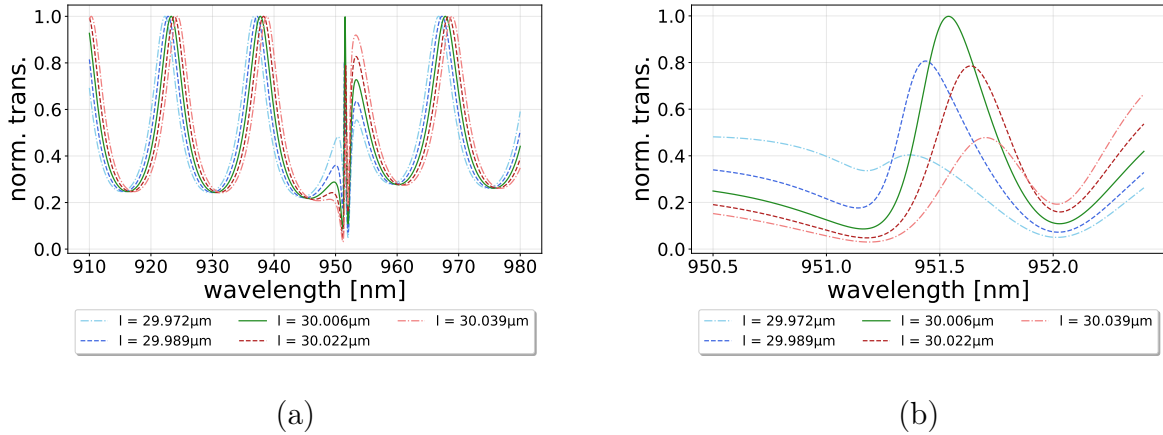


Figure 24: (a) shows lossless long-range transmission spectra of double Fano cavities of lengths  $l \rightarrow l' \approx 30\mu\text{m}$  with  $\Delta = 0.8\text{nm}$ . (b) shows the same spectra as seen in (a), zoomed in on the range around the transmission wavelength  $\lambda_t$ .

Figure 24 shows the effect of a relatively large detuning of  $\Delta = 0.8\text{nm}$ . This is simply included for a visual representation of a detuning which is considered "too large" for any practical use. The long range scan in figure 24a shows that the Fabry-Perot like fringes are now even more displaced, and figure 24b showing the spectra enhanced around the resonance wavelength shows roughly the same

trend as in figure 23b, only that this example is greatly broadened in comparison. It is though noted, that while broadened, the Fano resonance mode is sustained even for the relatively large detuning.

In order to get a clear qualitative picture of the double Fano cavity transmission profile as a function of both cavity length and wavelength, we visualize the varying of both in a heat map and let the color indicate the transmission intensity. This is shown in figure 25 which depicts a lossless cavity of length  $l \approx 30\mu m$  and detuning  $\Delta = 0.3nm$ . Here the movement of the resonance peak as a function of the cavity length is clearly seen as a slope of the "line" representing the high intensity region due to the Fano resonance.

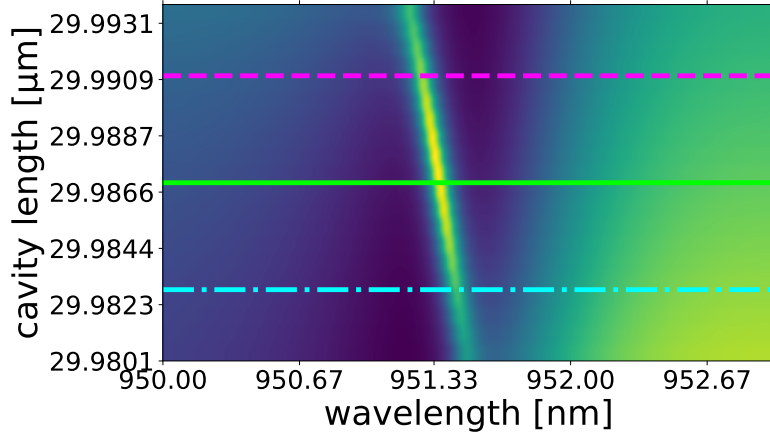


Figure 25: Heat map of the lossless double Fano cavity transmission as a function of wavelength and cavity lengths ranging  $l \rightarrow l' \approx 30\mu m$  for  $\Delta = 0.3nm$

Considering only the heat map, it is not easily visible which cavity length is the optimal one, however, the *magenta*, *cyan*, and *limegreen* lines across the heat map indicate slices which are depicted separately in figure 26. It is seen by analysing the transmission profiles of the three cavities of specific lengths, how they vary in both position and linewidth. The lengths and corresponding linewidths are given as

$$\begin{aligned} l_{magenta} &= 0.2l + 0.8l' \rightarrow HWHM_{magenta} = 40.5pm \\ l_{cyan} &= 0.8l + 0.2l' \rightarrow HWHM_{cyan} = 31.9pm \\ l_{lime} &= (l + l')/2 \rightarrow HWHM_{lime} = 29.7pm. \end{aligned} \quad (49)$$

It turns out that of the three cases, the *lime* transmission profile seems optimal as it is the narrowest of the three, and seems to be more preferably positioned, i.e.

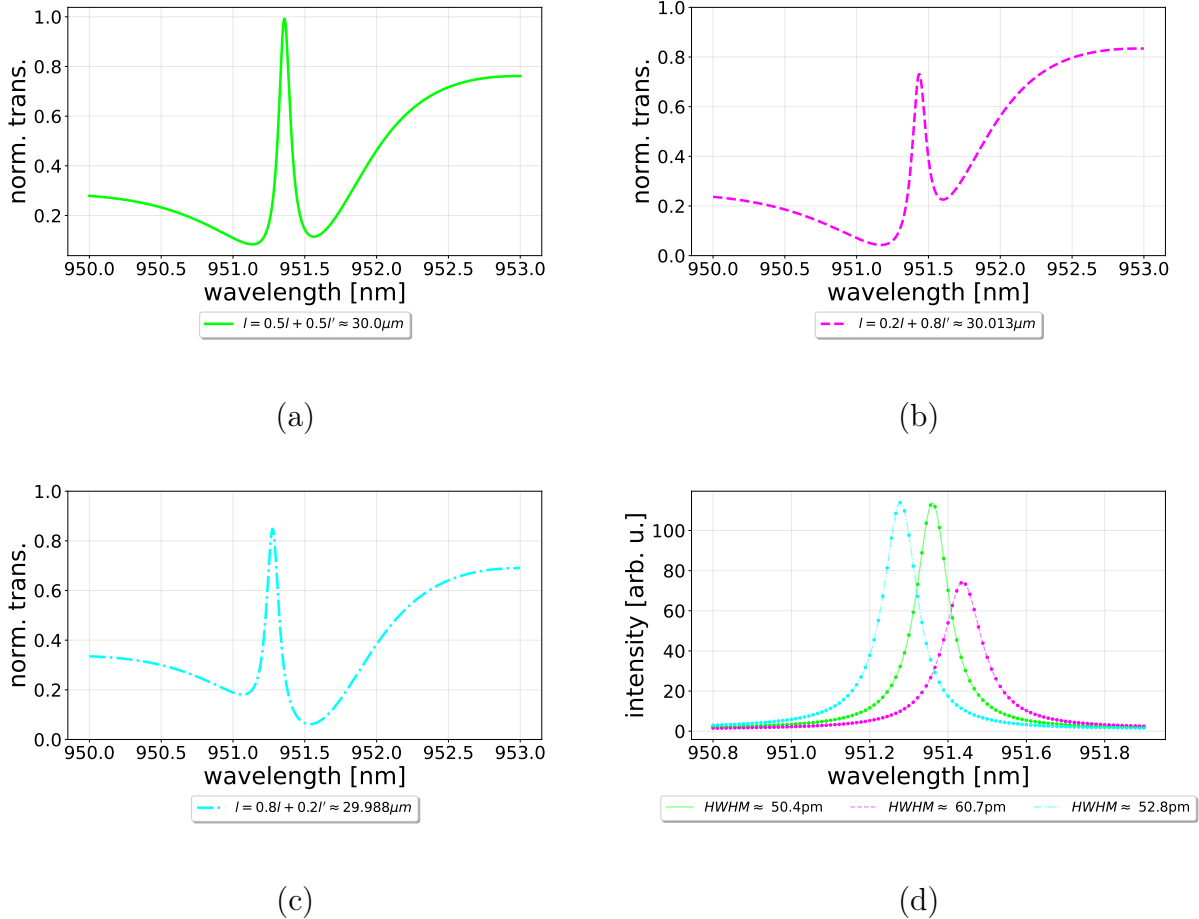


Figure 26: (a), (b) and (c) show slices of the heat map in figure 25 indicated by their respective color and line type in order to compare different cavity lengths. (d) show intracavity spectra of the peaks in (a), (b) and (c) with corresponding least squares fits and linewidths found as parameters hereof.

it is more centered in and thus separated from the Fabry-Perot-like background.

This trend is further examined in figure 27 where the linewidths of intracavity spectra are shown as a function of the cavity length. The parameters used are the same as in figure 25 and the figure indicates that the optimal cavity length is definitely "somewhere in between" the two guided-mode resonance lengths. However, it is also evident that the previous assumption for  $\lambda_t$  is too simple to be general in this case.

As a visual and qualitative representation of the effect of increasing the detuning  $\Delta$ , figure 28 shows heat maps similar to the one in figure 25, but for a range of values for the detuning  $\Delta = 0.01\text{nm} \rightarrow \Delta = 1.21\text{nm}$ . It is readily seen that

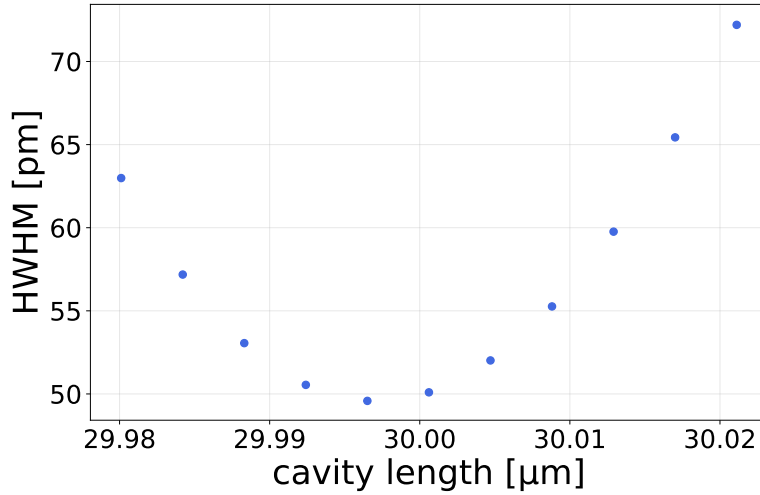


Figure 27: Linewidth as a function of cavity length  $l \rightarrow l'$ . Each point is found as a fitting parameter from a least squares fit to the generalized Fano model in eq. (33) of lossless intracavity double Fano spectra.

the aforementioned slope of the high intensity region, indicating the resonance peak, increases with the detuning. This is a representation of the peak moving to higher wavelengths, both for the optimal transmission wavelength and for the one closer to the detuned Fano mirror guided-mode resonance. The broadening of the peak is also displayed in a way that is, while only qualitative, convincing.

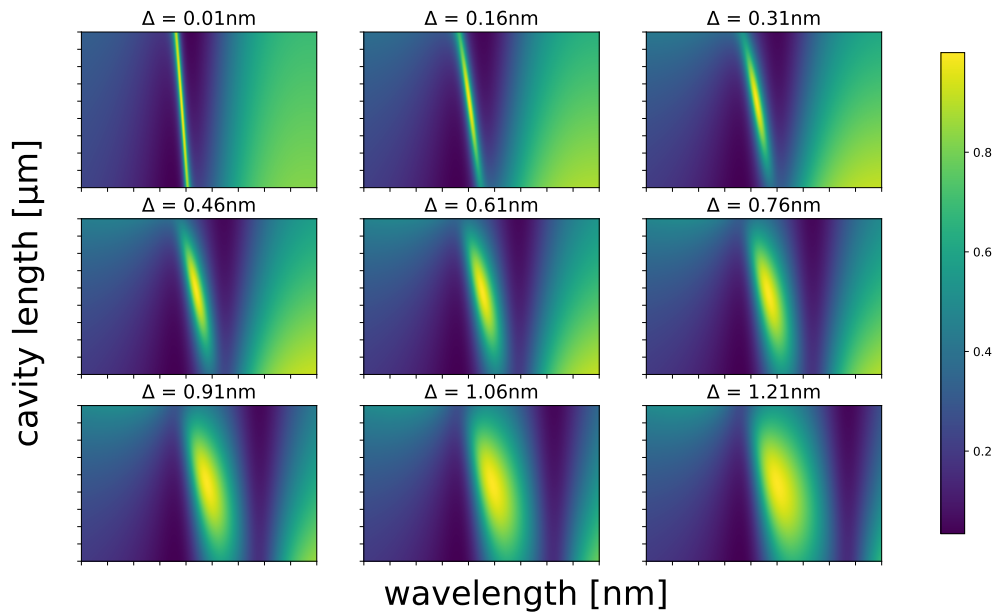


Figure 28: Series of heat maps showing lossless double Fano transmission spectra as a function of the cavity length, for increasing detuning  $\Delta$ .

# 3 Method

## 3.1 The experimental setup

The experimental setup used to optically characterize the Fano mirrors, single- and double Fano cavities is illustrated in figure 29. The specific part of the setup surrounding the cavity, outlined by the dashed line, is subsequently shown in figure 30.

In order to effectively conduct the experiments in this project, it is imperative to be able to control certain parameters. Each element in the experimental setup is thoroughly considered for each their purpose in this regard, these will be outlined in this section.

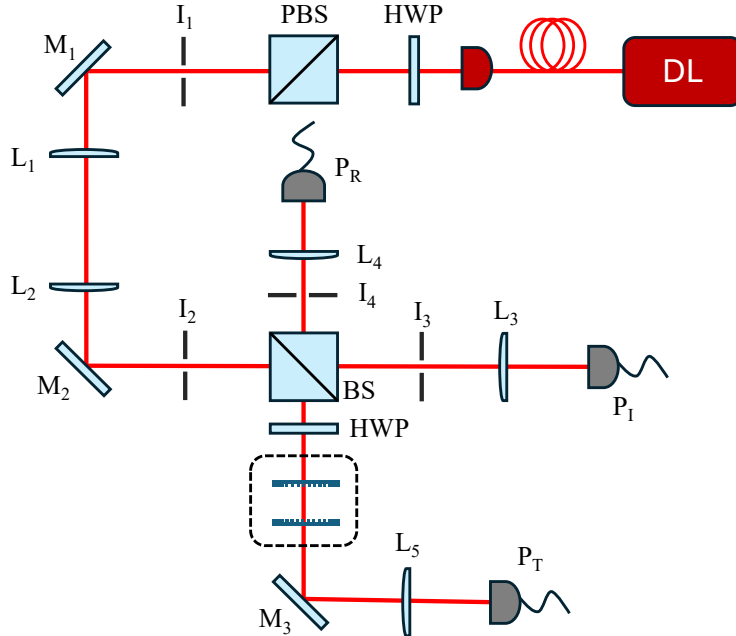


Figure 29: Schematics of the experimental setup for measuring Fano cavity transmission- and Fano mirror transmission/reflection spectra. The diode laser  $DL$  emits light into the setup through the optical fiber, the  $\lambda/2$ -waveplate  $HWP$  and polarizing beam splitter  $PBS$  ensures the light is linearly polarized and the optical telescope consisting of lenses  $L_{1,2}$  modifies the beam waist to fit the given purpose. Detectors  $P_{T,R,I}$  records the transmitted, reflected and incident light, respectively and the second HWP makes it possible to tune the polarization of the light just before the light is incident on the Fano cavity/mirror. The dashed line indicates the cavity setup seen in detail in figure 30.  $I_{1-4}$  and  $M_{1-3}$  indicate apertures/iris' and mirrors, respectively.

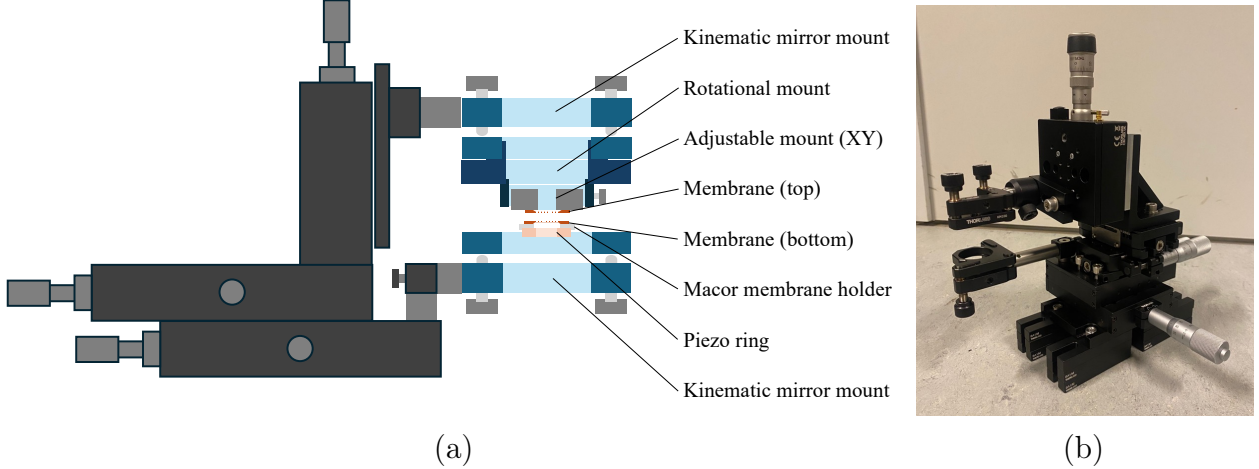
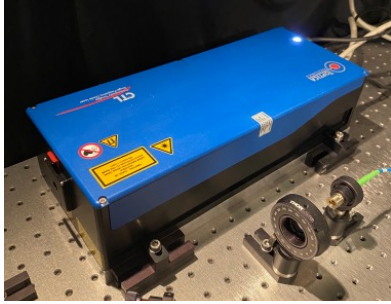


Figure 30: (a) shows a sketch of the schematics of the Fano cavity setup located inside the dashed line in figure 29. The stages attached to both the top and bottom of the cavity are used to spatially align the Fano mirrors of the cavity, while the kinematics mirrors are used to adjust for the angular degrees of freedom. The piezo ring is used to scan for and tune the optimal length of the cavity and the rotational and adjustable xy-mounts are used for aligning the top of the cavity. (b) shows a picture of the cavity setup depicted schematically in (a). Note that the setup, both in (a) and (b), depicted is the one used to measure double Fano cavity transmission, and would thus be modified for Fano mirror characterizations.

### 3.1.1 Tunable diode laser

As shown in figure 29 the laser source used for optical characterizations is coupled into the setup through an optical fiber. The laser used is a *Toptica DLC Pro* tunable CW diode laser with a range for the transmission wavelength of 910 – 980nm[48]. The laser and controller are both depicted in figure 31. The optical fiber is a *P3-780PM-FC-10* fiber from Thorlabs which is a single mode, polarization-maintaining optical fiber with an effective range of 770 – 1100nm[49]. Between the Toptica laser and the incoupling end of the fiber, an achromatic  $\lambda/2$ -plate (HWP) and *polarizing beam splitter* (PBS) is placed in order to be able to control the incident power of the laser and to only couple linearly polarized light into the setup.

The light being emitted from the optical fiber is sent through another HWP and PBS in order to be able to control the resulting polarization in the setup even more precisely, should there be any discrepancies of the light coupled into the fiber. The out-coupling end of the fiber with the HWP and PBS is shown



(a)



(b)

Figure 31: The Toptica DLC Pro tunable CW diode laser (a) and the controller (b) used to tune the wavelength of the output beam.

in figure 32.

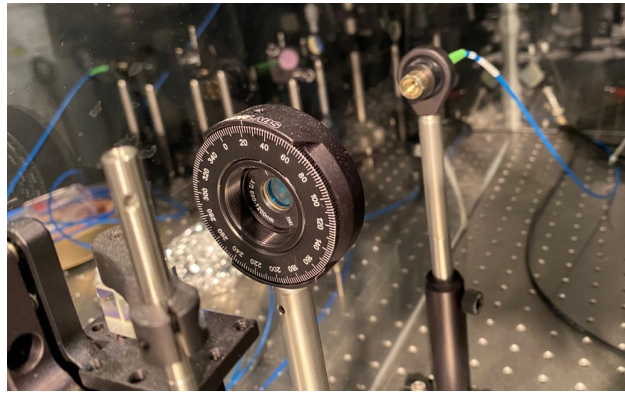


Figure 32: The out-coupling end of the P3-780PM-FC-10 polarization maintaining optical fiber from Thorlabs along with the HWP and PBS ensuring linear polarized light incident on the cavity or Fano mirror.

### 3.1.2 $\lambda/2$ - waveplate

A  $\lambda/2$ -waveplate, or HWP, is constructed of a so-called bi-refringent material (most commonly crystalline quartz), which means that it has slightly different refractive indices for incident light of different polarization axis'. Generally a HWP will have a *fast-* and *slow axis*, where it is understood that light polarized along the fast axis experiences a lower refractive index (and hence moves faster), than that along the slow axis. In this way the HWP separates the components of unpolarized light that has perpendicular and parallel polarizations with respect to the fast axis.

The effect of the HWP on linearly polarized light, is an effective rotation of the polarization, this is sketched simply in figure 33. It can be shown that the

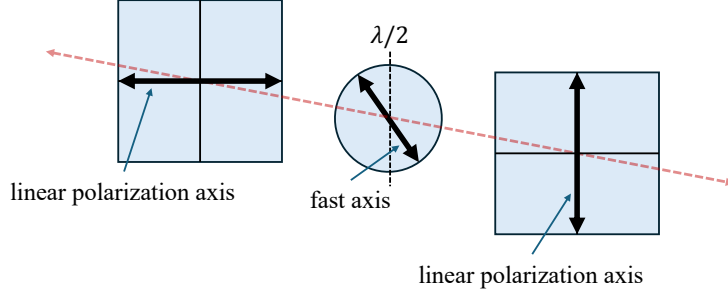


Figure 33: A simple sketch of the effect of a HWP on linearly polarized light.

polarization axis is rotated according to the angle between the fast axis of the HWP and the incident polarization axis. A relative angle  $\theta$  will thus result in a rotation of  $2\theta$ , e.g. if  $\theta = 45^\circ$ , this will constitute a rotation from completely p-polarized light to completely s-polarized light. This is the specific scenario sketched in figure 33[50]. In this way a rotating HWP can allow one to alter an incident linearly polarized beam to be polarized along any axis, and is thus a necessary component for this particular setup.

### 3.1.3 Optical telescope

The linearly polarized light transmitted through the PBS passes through plano-convex lenses  $L_1$  and  $L_2$  of respective positive focal lengths  $f_1$  and  $f_2$ . The two lenses makes up an optical telescope used to manipulate the beam waist  $w_0$  incident on the cavity or Fano mirror.

Figure 34a shows schematics of the general way an optical telescope is utilized to manipulate the beam waist of a laser beam.

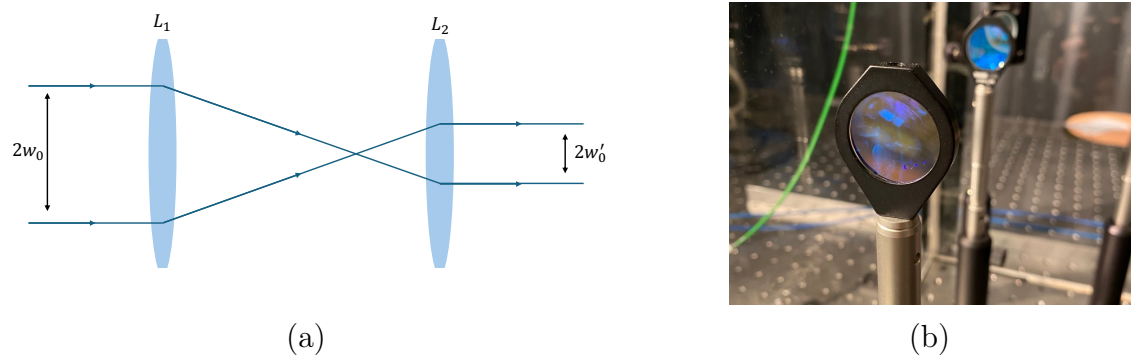


Figure 34: (a) shows simple schematics of an optical telescope used to alter the waist of an incoming collimated beam, while (b) shows a picture taken of the actual optical telescope used in the setup.

When the incident beam hits  $L_1$  it is focused according to its focal length  $f_1$ ,

and by inserting another lens  $L_2$  of a relatively longer focal length one can *catch* the beam at the desired beam waist. If focal length  $f_2$  is sufficiently large, compared with the path of the beam after the optical telescope, the beam will be approximately collimated and remain at the waist obtained when incident on  $L_2$ .

### 3.1.4 Transmission, reflection and incident photo-detectors

After passing the optical telescope the beam reaches a simple 50/50 beam splitter (BS) which transmits 50% of the light while reflecting the remaining 50%. The reflected light is then incident on the Fano cavity/mirror (target).

The transmitted light passes through a lens  $L_3$ , which is focused on photo-detector  $P_I$  used for reference measurements and later normalization. Since the tunable laser in nature varies in power with the wavelength, it is necessary to keep track of these fluctuations and correct for them in data analysis.

The reflected light is sent through, yet another, HWP which in this case is used only to alter the polarization of the light incident on the target. After the beam, or a portion of it, has passed the target it is sent through a lens  $L_5$  focused onto transmission detector  $P_T$ .

The part of the light incident on the target that is *not* transmitted, is reflected back onto the BS which then transmits 50% once again, and thus reflects the other 50%. The transmitted part here is focused through the lens  $L_4$  onto reflection detector  $P_R$ .

### 3.1.5 The double Fano cavity measurement setup

The cavity measurement setup shown in figure 30a is the one used to measure transmission spectra of the double Fano cavity consisting of two Fano mirrors. This part of the setup consists of one set of standard  $PT1\ \mu m$ -stages from Thorlabs[51] combined with an additional set of  $XRN25/M$  stages, also from Thorlabs[52], to provide precise movement of each Fano mirror in the xy-plane.

Examining the structure from the bottom (as it is built), a kinematic mirror mount is attached to the lower set of xy-stages, this is used to control the angular degrees of freedom of the bottom Fano mirror. On the mirror mount, a *NAC2123* piezo ring actuator from Noliac[53] is firmly attached and connected to a piezo driver. The driver is capable of applying a fixed current, and thus manually controlling the piezo expansion, but is also connected to a frequency

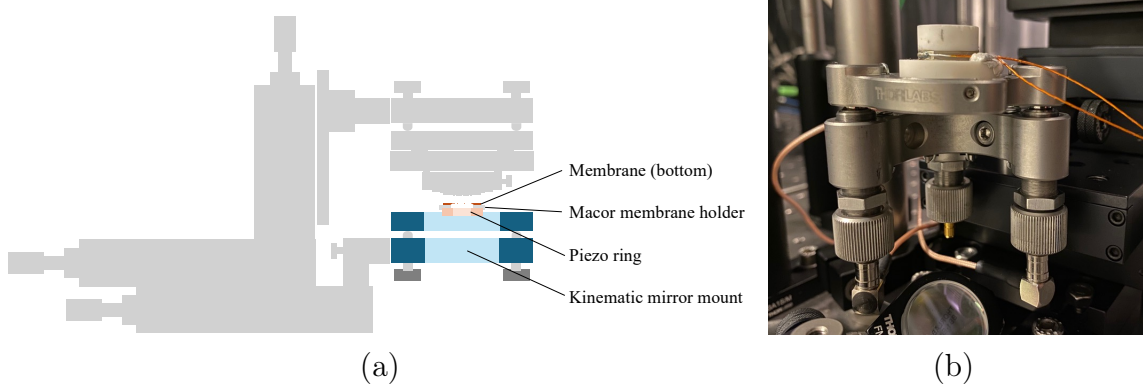


Figure 35: (b) shows a picture taken of the *bottom* part of the double Fano cavity setup, while (a) depicts the corresponding schematics.

generator. The signal from the frequency generator can be used to modulate the piezo expansion by an alternating current, which practically scans the cavity length in a range according to the effective free stroke of the piezo ring. Lastly, in order to be able to place the Fano mirror on the piezo ring, a ceramic Macor membrane holder is used. The bottom part of the cavity setup is highlighted in figure 35a.

The part of the setup built to control the top Fano mirror is slightly more complicated, as this is the Fano mirror that is, for practical reasons, aligned last. This means that additional degrees of freedom must be controlled by movement of the Fano mirror itself. The alignment procedure will be explained in detail in sections 3.2 and 3.3.

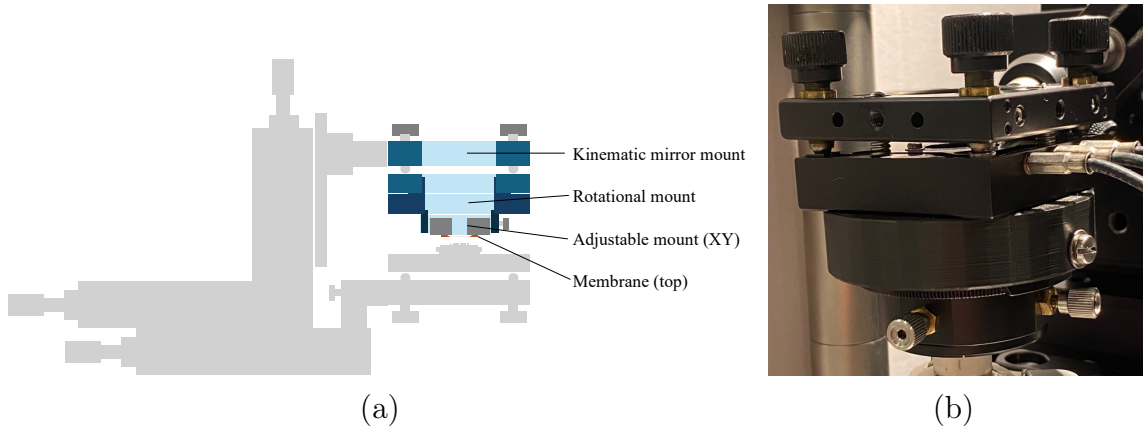


Figure 36: (b) shows a picture taken of the *top* part of the double Fano cavity setup, while (a) depicts the corresponding schematics.

The top part of the cavity setup is attached to the second set of xy-stages and additionally to an *NFL5DP20* stage from Thorlabs[54] placed in the z-direction

in order to be able to change the length of the cavity when aligned. As for the bottom part of the cavity setup, a kinematic mirror mount acts as the base of the construction. This is, once again, to control the angular degrees of freedom of the corresponding Fano mirror. This mirror mount is equipped with built-in piezo actuators in order to control the angular degrees of freedom, by applied voltage, with higher resolution than for manual adjustments. On the mirror mount, a standard rotational mount with a 1 inch inner winding is attached in order to be able to control the rotational degree of freedom of the Fano mirror. An additional xy-adjustable mount is then used in order to effectively place the Fano mirror in the center of the rotational mount to ensure the rotational axis is in the center of the membrane. Finally, the Fano mirror is taped to a custom mount created to fit into the xy-adjustable mount. The top part of the cavity setup is highlighted in figure 36a, and presented separate from the setup to show how the Fano mirror is attached in figure 37.

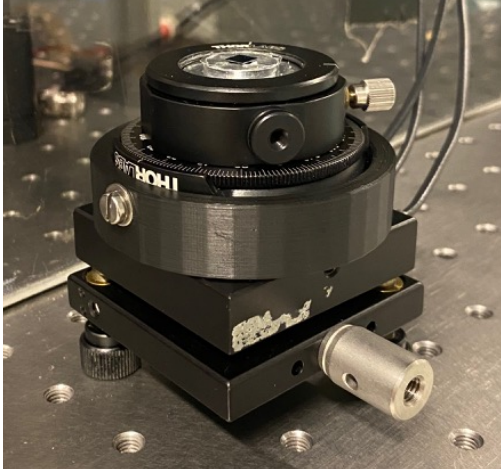


Figure 37: The top part of the cavity setup separated from the rest and flipped. Note that the Fano mirror attached with the tape is shown. The three wires visible are connecting the piezo actuators with a driver.

What has been outlined here is the setup utilized to optically characterize the double Fano cavity. If one wishes to do so for the single Fano cavity instead, the setup would be modified such that the top part of the setup, highlighted in figure 36a, would only consist of the kinematic mirror mount, and the top xy-stages would furthermore be redundant and hence removed. Inside the mirror mount would then be placed a broadband mirror. The rotational- and xy-adjustable mounts would not be needed in this case, due to the rotational symmetry, and size, of a standard broadband mirror.

### 3.1.6 Vibrational noise reduction

When the cavity measurements were conducted it was apparent that the double Fano cavity was particularly prone to noise. While noise is not a very precise definition in its own, it did seem that the most prominent source was associated with the length of the cavity. When applying a constant voltage to the piezo actuator depicted in figure 35, in order to achieve the correct length for sustaining the Fano resonance, the signal started to fluctuate dramatically when approaching the resonance.

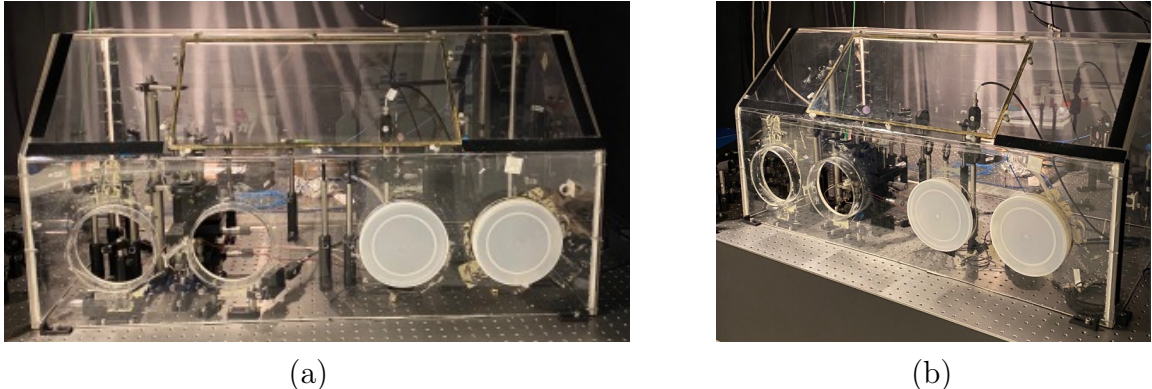


Figure 38: Front- (a) and side (b) views of the plexi-glass box used to reduce the acoustic noise in the setup.

By examining the characteristics of the noise when apparent, the source appeared to be acoustic in origin, i.e. making a sudden sound in close vicinity of the setup caused a spike in the noise level.

In order to reduce the acoustic noise, a plexi-glas box was placed around the entire setup as seen in figure 38. This proved to reduce the noise, and hence improved the signal-to-noise ratio substantially.

While the signal-to-noise ratio was improved, noise was still present, and additional measures in order to reduce this was taken. Two slabs of *teflon* were introduced into the setup, one between the optical table and the first set of xy-stages in the cavity setup, and the next between the first and second set of xy-stages. The reasoning behind this modification relied on the difference in acoustic impedance of teflon relative to aluminium. A high change in acoustic impedance creates an interface which should reflect any unwanted vibrations propagating through the optical table. This further reduced the noise, while it regrettably did not remove it completely.

### 3.1.7 Additional equipment used

In order to record a measurement of any kind in the setup, a *Keysight InfiniiVision DSOX2024A*[55] oscilloscope was connected with all the detectors  $P_T$ ,  $P_R$  and  $P_I$  in the setup. The oscilloscope, along with the Toptica laser, was then controlled by a Matlab script implemented by previous students/researchers of the lab.

Scanning the piezo element, by application of an alternating current also required additional equipment, and more specifically a frequency generator capable of generating a triangular signal with an offset. The frequency generator used was a *Keysight 33500B Waveform Generator*[56]. Insight on scanning the cavity length using the piezo actuator will be provided in section 3.3. The oscilloscope and frequency generater are shown in figure 39.



Figure 39: Pictures of the oscilloscope (a) and frequency generator (b) used during experimental investigations in this project.

## 3.2 Characterization of sub-wavelength grating

The sub-wavelength gratings, or Fano mirrors, used are commercially available high-quality silicone nitride  $SiN$  membranes suspended on a  $Si$  frame, which have been patterned into a grating. Figure 40a shows a packaged membrane from Norcada, which is the company who has provided all gratings/membranes used in this project. Figure 40b is a close-up picture of a bare membrane which have not yet been patterned, and includes a scale to provide perspective regarding the physical dimensions.

The patterned area of the Fano mirrors used throughout this project is  $400 \times 400\mu m$ , and this along with detailed dimensions of the whole membrane is sketched in figure 41.

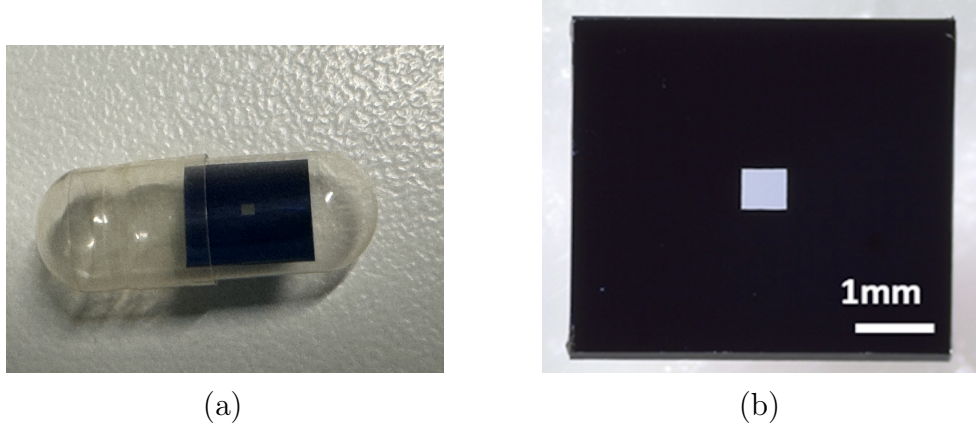


Figure 40: (a) shows an image of a packaged bare membrane, which has not yet been patterned, from Norcada. (b) is a close-up image of a bare membrane like the one in figure 40a.

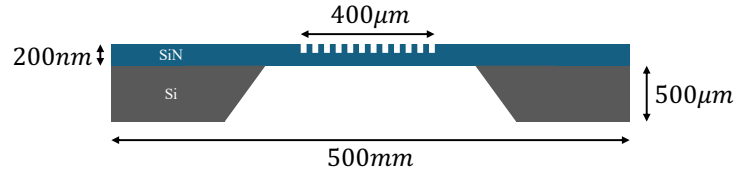


Figure 41: A simple sketch of the profile of a patterned membrane, i.e. a Fano mirror. It is seen that the width of the patterned area is  $400\mu m$ .

### 3.2.1 The alignment procedure

In order to align the Fano mirror for optical characterization, the setup utilized is a simplified one compared with the double Fano cavity setup shown in figure 30. This setup corresponds to one where only the *bottom* part is included, i.e. corresponding to the one highlighted in figure 35a. It must here be noted, that if the purpose of the Fano mirror alignment is to create a cavity, the top part shown in figure 36a must of course be utilized as well.

The goal of the alignment procedure is to ensure that the coupling between the guided-mode and the mode of the laser is maximized, this is outlined in section 2.2. The transmission of the Fano mirror is measured during alignment with a *PM100D* digital handheld optical power meter from Thorlabs[57], and progression of the alignment procedure is understood as minimizing the transmission. The behavior of the Fano mirror transmission, when perfectly aligned, can be seen in figure 9, where it has been simulated for a Fano mirror of arbitrary physical parameters. When aligned, the guided-mode resonance wavelength can thus be found. This is practically done by scanning the expected

wavelength range using the Toptica laser and recording the wavelength at which the transmission is minimized.

The three degrees of freedom, in which the alignment of the Fano mirror is optimized, are the translational coordinates ( $x$ ,  $y$ ), the rotational degree of freedom, and the two angular degrees of freedom. It is assumed at this point that the waist of the beam incident on the Fano mirror is optimal, this will be expanded upon in section 3.2.2.

The general order in which the alignment is done is given as:

1. xy-plane alignment.
2. Alignment of the angular degrees of freedom (adjusting the kinematic mirror mount).
3. Rotational alignment (adjusting the HWP placed prior to the cavity setup).

## xy-plane alignment

The translational alignment of the Fano mirror in the xy-plane is simply done by movement of the xy-stages (linear  $\mu m$ -stages from Thorlabs) shown in figure 30. Here it is crucial to know how the transmission level behaves qualitatively as a function of the xy-positions when the wavelength of the laser is off-resonance with respect to the guided-mode of the Fano mirror. Due to the effective thickness of the membrane in patterned and un-patterned areas being different, the transmission properties will vary slightly. This can be utilized in order to align these parameters effectively. Assuming one of the coordinates,  $x$  or  $y$ , is optimal, and one scans across the other as indicated in figure 42, it will be evident that the transmission is constant when the entire beam is incident on the bare membrane, while it will experience a slight change in the patterned area, simply due to the changed effective thickness of the structure in this area.

## Angular alignment

Adjusting the angular alignment, which is done by turning the screws on the kinematic mirror mount holding the piezo ring and the Macor membrane holder, is crucial for the evaluation of the guided-mode resonance wavelength. As reported by Parthenopoulos et al. in [42] the resonance wavelength of the guided-mode depends strongly on the angle of incidence.

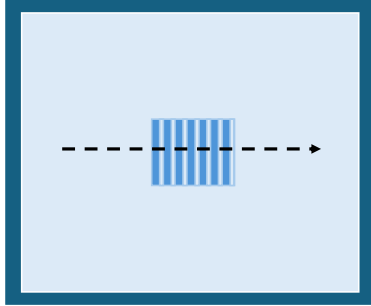


Figure 42: Simple sketch of a patterned membrane, i.e. a Fano mirror. The darker area surrounding the *SiN* membrane is the *Si* frame and the dark blue lines in the center indicate the  $400 \times 400\mu m$  patterned area. The black dotted arrow is indicative of scanning across the membrane, by moving it relative to the beam, using one of the linear stages.

In figure 29 the components  $I_{1-4}$  indicate apertures (iris') used for the angular alignment. Specifically  $I_1$  and  $I_2$  are used to track the back-reflection of the beam incident on the Fano mirror to ensure as much overlap as possible. A complete overlap indicates that the incident beam is normal to the Fano mirror surface.

## Rotational alignment

The Fano mirrors provided by Norcada are designed to be used as so-called  $TM_0$  wave-guides. This means that the guided-mode resonance we wish to study is spectrally located inside the available wavelength range for an electric field polarized perpendicular to the grating lines. The polarization is thus an important parameter in order to achieve a maximized interaction between the laser and the Fano mirror[58].

For this reason the rotational alignment is vital in order to achieve the correct minimum transmission wavelength of the Fano mirror.

Since no rotaitonal degree of freedom is appointed the Fano mirror itself, and that this would greatly complicate the alignment procedure, the rotational alignment is achieved by changing the polarization of the incident light. This is done by adjusting the rotating HWP placed immediately before the light is incident on the Fano mirror surface and is possible due to its effect on linearly polarized light illustrated in figure 33.

### 3.2.2 Adjusting and measuring the beam waist

In section 3.2.1 we assumed an optimal beam waist as the alignment procedure was outlined. This was due to the fact that the beam waist optimization is unnecessary unless the entire setup is rebuilt or if the size of the Fano mirror is changed. Since the patterned area of the Fano mirrors characterized in this project was only  $400 \times 400\mu m$ , the beam waist optimization was only done once.

As is evident from figure 34a an optical telescope was utilized to tune the waist size  $w_0$  of the collimated beam. In order to determine the optimal value of  $w_0$  the second lens  $L_2$  was moved back and forth without diverging from the position where the optical axis passed through the center of the lens. The minimum transmission was then recorded for each iteration, until the transmission converged. When the minimum transmission as a function of  $w_0$  was found, this was measured using the *razor blade method*. The razor blade method is a simple tool to, fairly accurately, measure the beam waist of a Gaussian laser beam by *cutting* the beam gradually with a sharp blade. The distance the blade moves is recorded along with the transmitted intensity, and the two are thus directly correlated[59].

An arbitrary Gaussian distribution, corresponding to a laser beam in the TEM00 mode, is shown in figure 43a, while figure 43b shows the integral of the distribution as a function of the razor blade position, which corresponds to an error function.

In practice the blade position was recorded by counting the turns made on a linear  $\mu m$ -stage with the razor blade attached, and the transmitted intensity was recorded live by a power meter from Thorlabs. The power of the laser beam without being *cut* by the blade was tuned to  $\sim 1mW$  such that the percentile change was intuitively recorded. The linewidth of the Gaussian beam is then approximately given as the distance between the two cut-off points where the transmitted intensity is given as 16% and 84%. The optimal value for the beam waist was found to be

$$\delta\lambda_{400\mu m} \approx 160\mu m. \quad (50)$$

### 3.2.3 Obtaining normalized transmission/reflection spectra

When the Fano mirror and the surrounding setup is completely aligned, it is time for the optical characterization. A series of measurements is necessary to

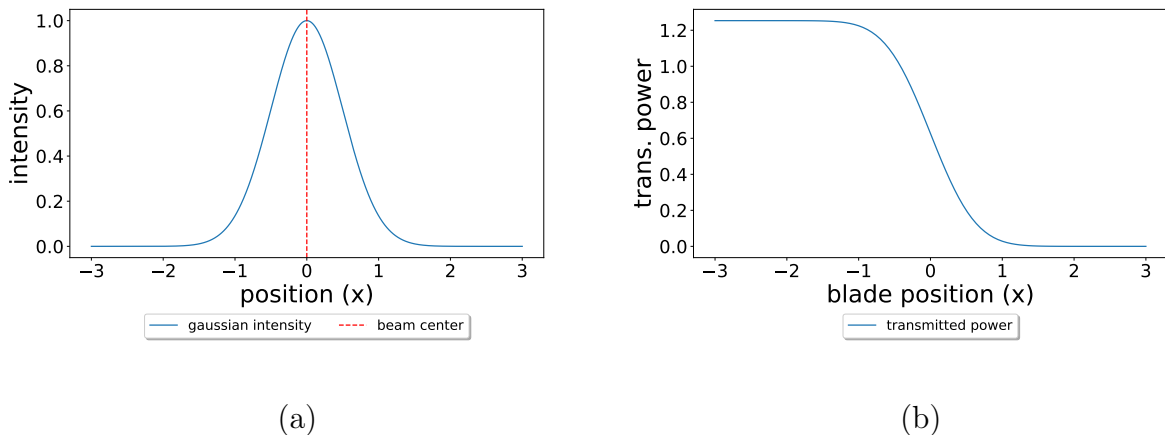


Figure 43: (a) shows an arbitrary Gaussian distribution, where the red dashed line indicates the position of the maximum value. (b) shows the transmitted intensity as a function of the position of the razor blade, as the razor blade method is simulated, i.e. the beam is gradually covered with the blade.

obtain normalized transmission and reflection spectra which rightfully represent the optical properties of the Fano mirror.

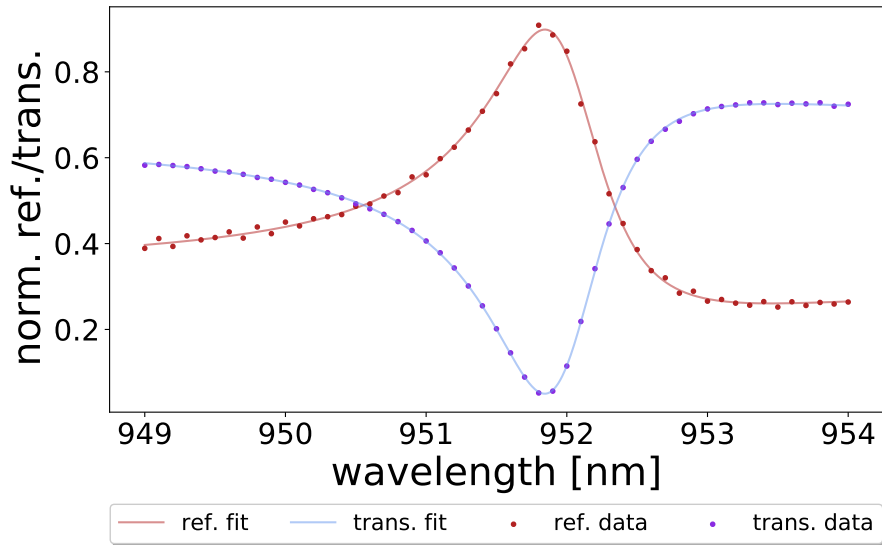


Figure 44: Normalized transmission and reflection spectra of  $400 \times 400\mu\text{m}$  Fano mirror G2 (M3).

The structure of such measurements is given as follows:

1. The transmission and reflection intensities as a function of the wavelength are measured using the reflection detector  $P_R$  and the transmission detector  $P_T$ , while the signal measured in detector  $P_I$  is recorded as a reference measurement. The positions of all detectors are shown in figure 29.
2. The Fano mirror is removed and identical measurements are done for an "empty" setup. The purpose of this measurement is to measure the signal when *all* the incident light is transmitted, and *no* light is reflected. This data is used to normalize the transmission intensities obtained in the first measurement.
3. On the former position of the Fano mirror, a highly reflective (HR) mirror is now placed, and all measurements are repeated. This is corresponding to *all* the incident light being reflected, and *no* light being transmitted. This data is used to normalize the reflection intensities obtained in the first measurement.
4. Lastly, a measurement of the background signal is taken, by simply blocking the laser before it enters the setup and repeating the measurements.

The normalized values are then given as

$$T_{norm} = \frac{(T - bg)/(T_I - bg)}{(T' - bg)/(T'_I - bg)} \quad (51)$$

for the transmission amplitudes, and

$$R_{norm} = \frac{(R - bg)/(R_I - bg)}{(R' - bg)/(R'_I - bg)} \quad (52)$$

for the reflection amplitudes. Here  $T = |t|^2$  and  $R = |r|^2$  denote the transmission and reflection intensities measured by  $P_T$  and  $P_R$  in step (1),  $T'$  and  $R'$  are the values measured for the transmission- and reflection intensities in steps (2) and (3), respectively. The subscript  $I$  indicates values obtained by the incident detector  $P_I$  for its corresponding measurement type. The background values obtained in step (4) are subtracted, these are labeled  $bg$ . Figure 44 shows an example of normalized spectra obtained by measurements (1)-(4) and calculations of eqs. (51) and (52).

### 3.3 Cavity measurements

The cavity measurements outlined in this section will be that of the double Fano cavity. The single Fano cavity measurement procedure will secondarily be clear

as a simplification of the one for the double Fano cavity.

A very simple explanation of the cavity measurement procedure is that one must go through the Fano mirror alignment process outlined in section 3.2 twice. One time for the bottom of the cavity, and then once for the top of the cavity, whereafter the two Fano mirrors are broad together according to the wanted cavity length and the transmission is recorded. However, this procedure contains many degrees of freedom and practicalities making it difficult to simply align each Fano mirror independently of each other. This section will go through each step of the process of arriving at a meaningful measurement of the transmission of the double Fano cavity.

### 3.3.1 Aligning the double Fano cavity

Before considering beginning to align the double Fano cavity, it is imperative to have two Fano mirrors which have similar physical dimensions, and thus be described by similar parameters as presented in section 2.2. In order to find a *match*, the only valid method is to use brute force and simply characterize Fano mirrors until a match is found. The batch of tested Fano mirrors in this project all came from the same order delivered by Norcada, as this was assumed to provide the best chances for a match. The condition for the spectral detuning  $\Delta = |\lambda_0 - \lambda'_0|$  of otherwise identical and lossless Fano mirrors is outlined in section 2.4.5. The spectra of Fano mirrors characterized but *not* used is found in Appendix B.

Here we introduce a matching set of arbitrary Fano mirrors denoted  $A1$  and  $A2$ . The alignment process is then given as follows:

1. The bottom, i.e. Fano mirror  $A1$ , of the cavity is aligned according to the procedure outlined in section 3.2. This means that the incident beam is centered on and normal to  $A1$ , and the polarization of the light is aligned such that the electric field is perpendicular to the grating lines. The wavelength of the laser is scanned, and the one corresponding to the guided-mode resonance of  $A1$  is recorded.
2. The bottom grating position is marked and the macor membrane holder (the macor membrane holder can be seen in figure 30a) containing  $A1$  is removed and stored safely. Now the laser polarization and translational coordinates of  $A1$  are fixed and must not be changed in the following steps of the alignment procedure. The marks used to indicate the position of

A1 is shown in figure 45.

3. The top part of the cavity is inserted, but *without* the other Fano mirror A2 in place, as the kinetic mirror- and rotational mounts first need to be centered in the beam. This is done by inserting a  $100\mu\text{m}$  pinhole, specifically designed for the purpose, into the rotational mount. The translational and angular coordinates of the top mount is thus changed to maximize the signal through the pinhole. The centering is then tested by rotating the pinhole and ensuring that the signal does not change, i.e. that the center of the rotational mount does not move out of the beam by rotating it. When this is satisfied, the top mount is removed and the translational coordinates are considered aligned and thus fixed. The so-called *pinhole alignment method* will be explained in greater detail in section 3.3.5.
4. The Fano mirror A2 is placed, with tape, onto the xy-adjustable mount (see figure 37), which is then fastened to the rotational mount. The top mount now completely resembles the one shown in figure 37. A2 is now aligned following a similar structure as the one outlined in section 3.2, but with the constraint of the above parameters being fixed. A2 is moved into a position where it is centered with respect to the incident beam by adjusting the xy-adjustable mount, and the Fano mirror itself is now rotated to match the polarization of the laser. The angular alignment is done very similarly to that of A1, as the kinetic mirror mount is here used. When A2 is aligned, the wavelength is once again scanned, and the one matching the guided-mode of A2 is recorded.
5. The top mount, including A2, is now removed from the setup and all degrees of freedom are expected to be aligned. The trick to make sure that the angular alignment is preserved when re-inserting the top mount is that the back reflection is centered in the aperture  $I_4$  depicted in figure 29, this way one can quite easily regain the approximate angular alignment.
6. The macor membrane holder, with A1 placed on it, is now re-inserted into the bottom of the setup and the Toptica laser is set to the guided-mode resonance wavelength according to A1. In this way A1 is carefully placed according to the marked position (see figure 45) and adjusted, by hand, to achieve the same minimum transmission as before it was removed.
7. The top mount, including A2, is now too re-inserted, and adjusted by

hand such that the back-reflected beam overlaps with the aperture  $I_4$ .

8. The wavelength of the Toptica laser is now set to the transmission wavelength given in eq. (47), the wavelength exactly between the guided-mode resonance wavelengths of A1 and A2, i.e.  $\lambda_t = (\lambda_{0,A1} + \lambda_{0,A2})/2$ .

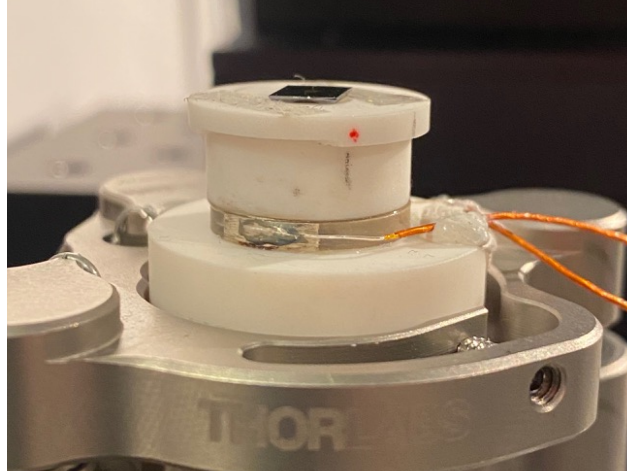


Figure 45: A close-up of the bottom part of the cavity with a Fano mirror placed on the macor membrane holder. Note the marks used to re-insert the bottom part of the cavity as mentioned in steps 2 and 6.

### 3.3.2 Cavity resonance - the piezo ring

Once the double Fano cavity is successfully aligned with respect to the individual guided-modes of A1 and A2, the cavity length must be tuned to match this according to  $2l = m\lambda$ , in order to excite the Fano resonance mode.

In order to tune the cavity length on the scale necessary, it is scanned by periodically varying the length of the cavity using the piezo ring actuator and applying an alternating current specified with the frequency generator shown in figure 39b. In this way the resulting signal recorded with photo detector  $P_T$  and seen in the oscilloscope shown in figure 39a is time-dependent and seen as fringes. Figure 46 shows the corresponding signal for an approximate cavity length of  $100\mu m$ , both simulated and as data recorded directly on the oscilloscope screen.

When the fringes on the time-dependent length scan are visible while scanning with the piezo ring, they can be optimized by making small adjustments of the angular degrees of freedom on the top of the cavity, i.e. of A2. The parallelism of the cavity is an important parameter for a cavity of high finesse, and while normal incidence have here been achieved for A1 and A2 individually, both

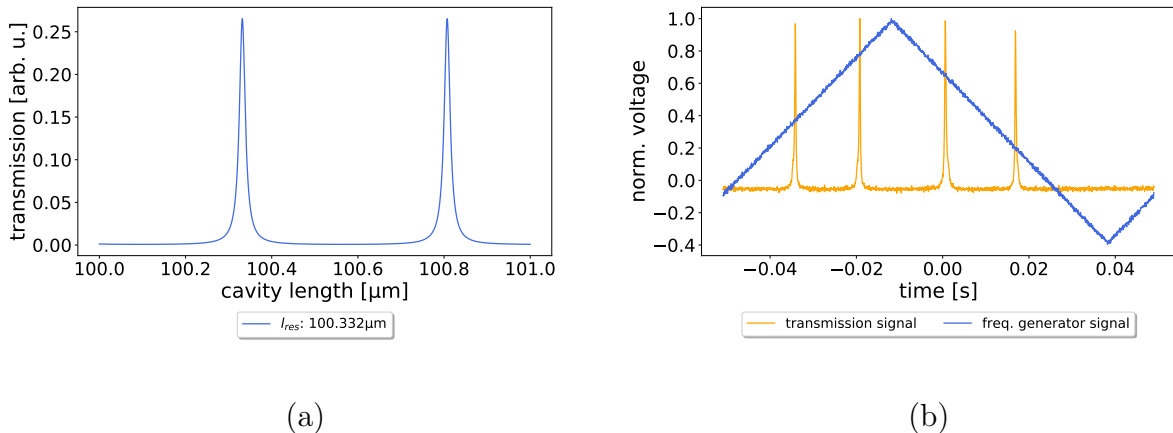


Figure 46: (a) shows a simulated length scan of range  $1\mu m$  for a symmetric lossless double Fano cavity of length  $\sim 100\mu m$ . The labeled resonant length  $l_{res}$  in the figure indicates the first length found that fulfills the brightness condition. (b) is a plot of raw data logged from the oscilloscope used to record cavity transmission data. The blue line shows the signal from a frequency generator which is applied to the piezo ring, i.e. it correlates to the piezo expansion and thus a change in the cavity length. The orange line represents normalized cavity transmission intensity as a function of time. Note that the triangular signal is necessary in order to uniformly expand and compress the piezo ring. This ensures that the FSR stems from a linear expansion and that the piezo ring does not break from non-linear stress across the crystal structure.

Fano mirrors have since been removed and re-inserted into the setup, which introduces uncertainty regarding the fine-tuning of the alignment. Especially the top of the cavity, which is fastened on nothing more than an optical post from Thorlabs have only approximate reproducability of the angular alignment (this is seen in figure 37). It is therefore prone to uncertainties hereof after re-insertion. For this reason the parallelism is optimized using the fringes on the oscilloscope. The parallelism is outlined in greater detail in section 3.3.6.

When the fringes of the time-dependent signal have been optimized fully, the frequency generator is then turned off and the fringes disappear. The piezo driver is now used to manually apply a constant voltage to expand the piezo gradually until the signal through the Fano cavity is maximized. This corresponds to the point where the cavity length and thus the cavity mode is resonant with the guided-modes of A1 and A2.

The piezo ring, while capable of tuning the cavity length on a very small scale,

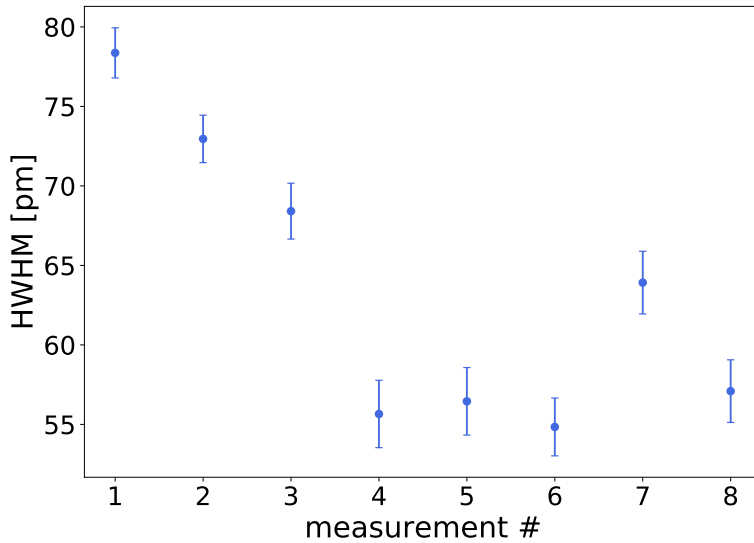


Figure 47: Linewidth as a function of "time" of an approximately  $452\mu m$  double Fano cavity. It is clear that the linewidth generally decreases with time as a baseline for the HWHM is reached. This is assumed to be due to the drift of the piezo ring, while it must be noted that this is not possible to conclude indefinitely from the presented data. "Time" is to be understood as the chronological order in time, as the measurements are presented in the order in which they were recorded in the lab.

tends to drift with time. This drift is apparent when the constant voltage is applied as the signal tends to decrease with time after optimization of the transmission. The piezo drift is more pronounced when the measurement session is first started and the piezo becomes more stable when a constant voltage have been applied to it for some time. For this reason the measurements of the Fano resonance transmission profiles tend to be broader at first, and then gradually converge to the optimal value as more measurements are conducted. Note however, that this varies greatly depending on the adjustments made throughout a measurement session. Figure 47 shows linewidths of the resonance transmission profile, of an arbitrarily chosen double Fano cavity, as a function of "time". "Time" is referring to the fact that the measurements are plotted in chronological order with respect to the time of measurement.

### 3.3.3 Determining the cavity length

Now the double Fano cavity is aligned and the cavity-, laser- and guided-modes all coincide to a high enough degree to sustain a Fano resonance mode. However,

before doing the actual optical characterization, the cavity length must first be determined. In the end we want to plot the linewidth of the double Fano resonance spectra as a function of the cavity length, and in order to do so we must measure both.

Here we remember that the Fano cavity, when off-resonance, acts simply as a Fabry-Perot interferometer, which means that the off-resonance spectrum abides by the relations outlined in section 2.1. More specifically we know that the FSR relates to the cavity length according to

$$l = \frac{\lambda_0^2}{2FSR}, \quad (53)$$

where  $\lambda_0$  is the cavity resonance wavelength.

So, to have a qualitative measure of the cavity length while doing measurements in the lab, off-resonance spectra are recorded and by estimating the FSR from the live data the approximate cavity length is determined.

In order to obtain precise information on the length of a given cavity, we conduct more precise data analysis on the recorded off-resonance spectra. Figure 48 shows two examples of off-resonance spectra for two cavities of different length. The lengths are found as a fitting parameters from a least squares fit of the recorded data to the Fabry-Perot transmission function found in eq. (3).

### 3.3.4 Recording normalized spectra

The normalized spectra are now recorded in largely the same way as for the individual Fano mirrors in section 3.2. A series of measurements is necessary in order to obtain meaningful spectra that are normalized with respect to the light incident on the cavity. The needed measurements are the following:

1. The transmission through the Fano cavity recorded in photo detector  $P_T$ . The corresponding values for the measured intensities are denoted  $T$ .
2. The signal recorded in photo detector  $P_I$  during the transmission measurement. The corresponding values for the measured intensities are denoted  $T_I$ .
3. The signal recorded in photo detector  $P_T$  when no cavity is present in the setup. This is denoted  $P'_T$ . The corresponding values for the measured intensities are denoted  $T'$ .

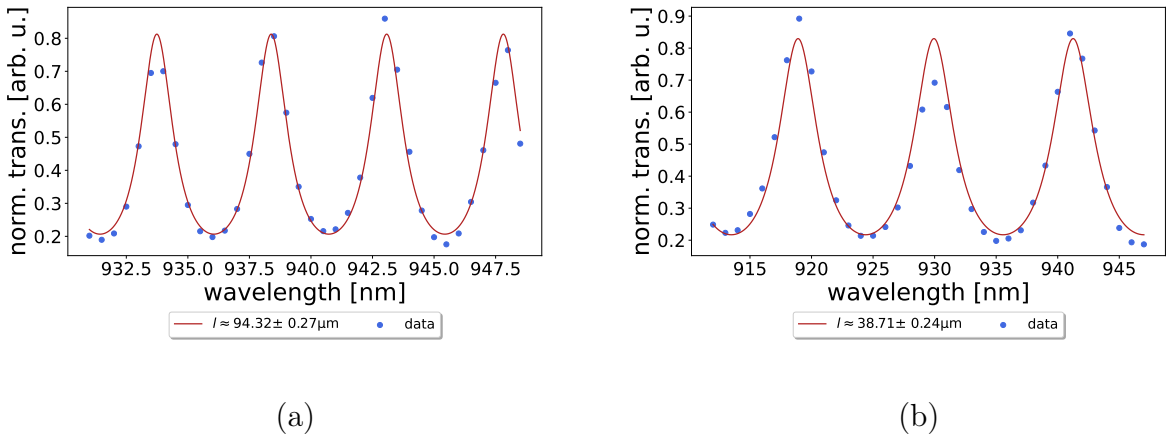


Figure 48: Off-resonance spectra of double Fano cavities of lengths  $94.32 \pm 0.27\mu m$  (a) and  $38.71 \pm 0.24\mu m$  (b). The lengths are found as fitting parameters from a least squares fit of the recorded data to the Fabry-Perot transmission function in eq. (3), and the errors presented are found as the square root of the diagonal of the covarians matrix corresponding to the fit [60]. Note that the FSR increases when the cavity length decreases, as predicted in eq. (53).

4. The signal recorded in detector  $P_I$  during the transmission measurement with no cavity present. This is similarly denoted  $P'_I$ . The corresponding values for the measured intensities are denoted  $T'_I$ .

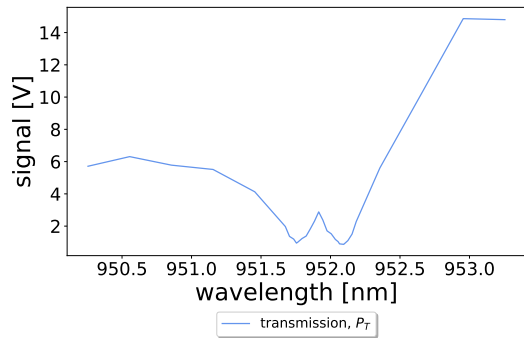
The normalized transmission values are then given as

$$T_{norm} = \frac{T/T_I}{T'/T'_I}, \quad (54)$$

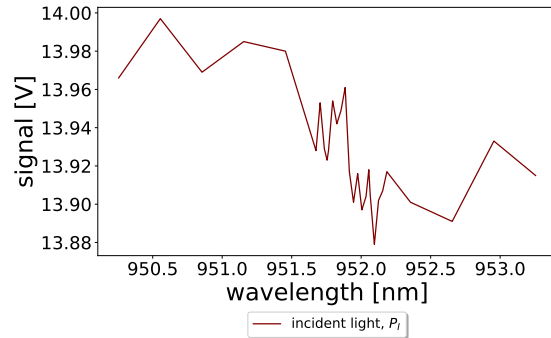
which is the exact formula used for the Fano mirror characterization, except for the subtraction of the background which has here been assumed negligible. Examples of the four measurements are seen in figure 49, and the normalized spectrum is correspondingly seen in figure 50.

### 3.3.5 Centering of the top grating

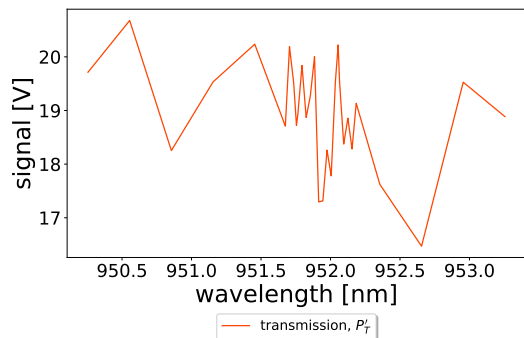
When aligning the top part of the cavity setup seen in figure 36, it is crucial to ensure that the beam passes through the center of the rotational mount. Even the slightest deviation from the center can cause the alignment to be tedious at best, but likely practically impossible. The reason for this is the need for invariance in the xy-plane when aligning the Fano mirror for the fixed polarization of the laser. If the deviation from the center is too large, it might



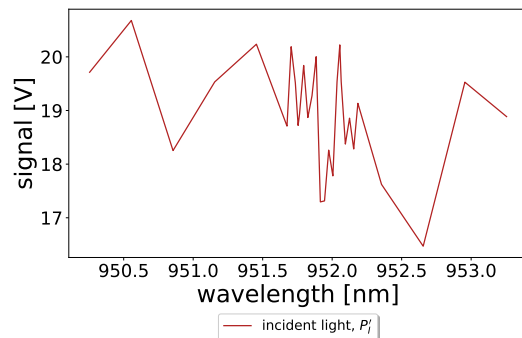
(a)



(b)



(c)



(d)

Figure 49: Examples of the four measurements used to produce the normalized transmission spectrum of the double Fano cavity (the same naturally applies for the single Fano cavity transmission). (a) shows the transmission through the double Fano cavity, (b) shows the incident light on the cavity, (c) shows the "transmission" when no cavity is present and (d) shows the light recorded by the incidence detector with no cavity present. All data is recorded for the same cavity of length  $l = 21.390 \pm 0.119\mu m$ . Note that the spectra in (c) and (d) seem identical. This is to be expected as they are simply measurements of a beam in each arm of a 50/50 beam splitter.

be impossible to tell whether the change in the transmitted intensity stems from moving further or closer to the optimal polarization, or if the Fano mirror is simply moving in and out of the beam. For this alignment a pinhole was designed to fit with high precision into the rotational mount in which it was fastened with a one inch (*SM1*) retainer ring from Thorlabs. A simple sketch of the pinhole is seen in figure 51a.

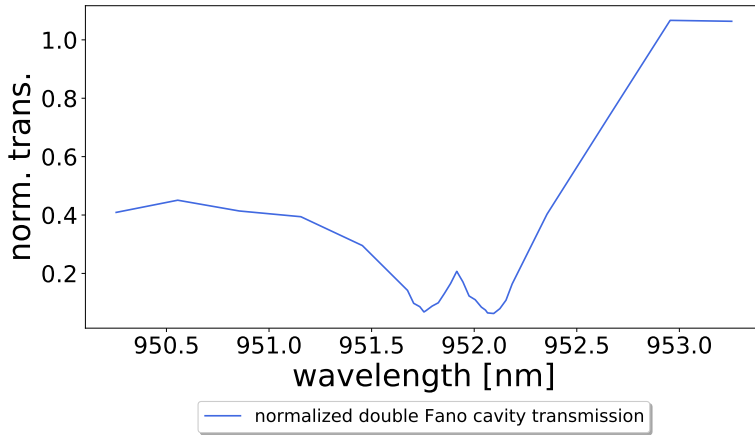


Figure 50: The normalized transmission spectrum for a double Fano cavity of length  $l = 21.390 \pm 0.119\mu m$  calculated from the data depicted in figures 49a-d using eq. (54).

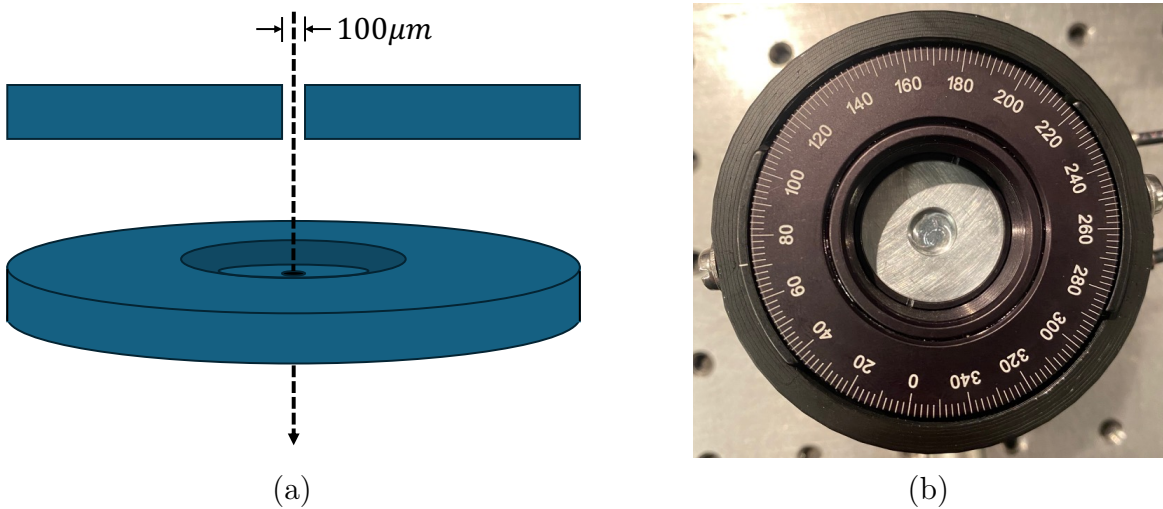


Figure 51: In (a) is a sketch of the pinhole used for centering the rotational-and kinetic mirror mounts in the incident beam. The side view of the pinhole is included to mark the pinhole diameter clearly while the angled view provides a visual representation of the actual component. (b) shows a picture of the rotational mount, seen from the top, with the pinhole inserted.

By moving the xy-stages in the cavity setup, it proved possible to achieve the centering of the rotational mount by moving the setup, with the pinhole inserted, until the transmission signal was maximized. Another test of the alignment was here to rotate the mount and thus pinhole and ensure that the signal intensity

was as close to rotationally invariant as possible. Figure 52 shows an arbitrary gaussian distribution resembling the transverse distribution of a laser beam in the TEM00 mode and two shaded regions imitating the position of the pinhole. The red shaded region shows an *unaligned* pinhole position while the green one is perfectly *aligned* in the center of the beam. It is shown on the figure that the red area covers an intensity corresponding to 15.8% of the maximum intensity, while this value for the aligned green region is approximately double at 30.53%.

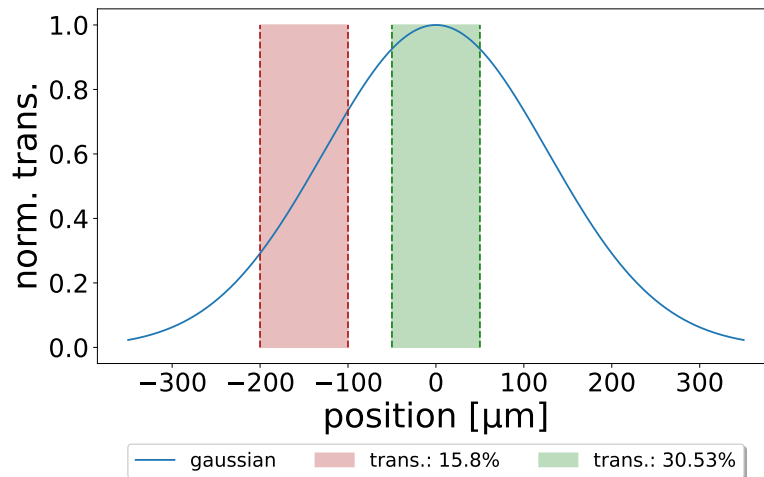


Figure 52: A gaussian distribution corresponding to the transverse distribution of a laser in the TEM00 mode. The red shaded region indicates a position for the pinhole with a transmission of 15.8% while the green one indicates a position with a transmission of 30.53%. The spatial dependence of the transmission through the pinhole is thus clearly displayed.

### 3.3.6 Estimating parallelism

A key difference between the single and double Fano cavity transmission spectra, is the off-resonance behavior. While the maximum transmission intensity for the single Fano will generally be lower than the Fano resonance peak, the opposite tends to be the case for the double Fano cavity. The direct reflectivities and transmissions  $r_d$  and  $t_d$  are similar, if not identical, for the two Fano mirrors, which means that the off-resonance Fabry-Perot-like transmission reaches a maximum of close to unity. The initial alignment of the cavity can thus be done by maximizing the off-resonance fringes. Due to the much broader peaks in this

spectral regime, the fringes will be much less sensitive than the resonance peak. For this reason additional optimization is likely necessary.

Nair et al. [61] has proposed an analytical formula to estimate the wedge angle by considering the maximum transmission  $T_{MAX}$  of these Fabry-Perot fringes.  $T_{MAX}$  is approximately given as

$$T_{MAX} \approx 1 - \left( \frac{F\pi w_0}{\lambda} \right)^2 \varepsilon^2, \quad (55)$$

for a cavity of identical resonators, and as this is not necessarily the case for an arbitrary double Fano cavity we make the substitution  $1 \rightarrow T_{MAX}^{optimal}$  to include the highest possible transmission given a set of compatible Fano mirrors. The expression now simply reads

$$T_{MAX} \approx T_{MAX}^{optimal} - \left( \frac{F\pi w_0}{\lambda} \right)^2 \varepsilon^2, \quad (56)$$

where  $T_{MAX}^{optimal}$  is the maximum transmission for a wedge angle of 0,  $w_0$  is the beam waist,  $\lambda$  is the wavelength,  $\varepsilon$  is the wedge angle in radians and  $F$  is the coefficient of finesse [38] given as

$$F = \frac{4R}{(1-R)^2}. \quad (57)$$

Rearranging this, for the wedge angle  $\varepsilon$  we get

$$\varepsilon \approx \sqrt{\left( T_{MAX}^{optimal} - T_{MAX} \right)} \left( \frac{\lambda}{F\pi w_0} \right). \quad (58)$$

An example of a normalized off-resonance transmission spectrum of a double Fano cavity is shown in figure 53. The blue line indicates a least squares fit of the data points to the Fabry-Perot transmission function seen in eq. (3), while the red line indicates the optimal transmission for the same Fano mirrors as was used for the measurement. The maximum transmission recorded and the optimal value was found as

$$T_{MAX} = 83.3\% \quad \text{and} \quad T_{MAX}^{optimal} = 97.1\%, \quad (59)$$

which yields for the wedge angle

$$\varepsilon \approx 0.24 \text{ mrad} = 0.014^\circ, \quad (60)$$

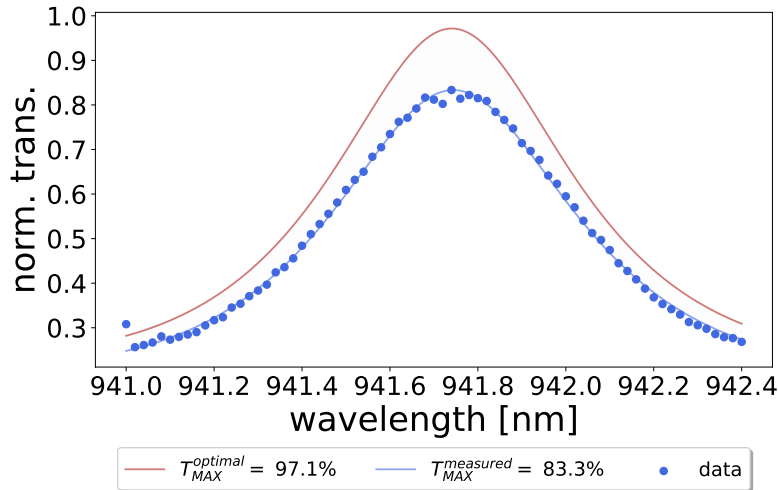


Figure 53: Example of a normalized off-resonance transmission peak of a double Fano cavity of direct reflectivities  $r_d = 57\%$  and  $r'_d = 57.5\%$  and direct transmissions  $t_d = t'_d = 81.4\%$ . The blue line is a least squares fit of the data to the Fabry-Perot transmission function while the red line is the optimal value of the same function. The red shaded area indicate the differnce between the two.

assuming a beam waist of  $w_0 = 160\mu m$  and direct reflectivities and transmissions  $r_d = 57\%$ ,  $r'_d = 57.5\%$  and  $t_d = t'_d = 81.4\%$ .

It is thus clear that while the sensitivity of the off-resonance Fabry-Perot fringes is lower than that of the Fano resonance peak, they still provide a significant measure of the parallelism and is thus useful for initial cavity alignment.

# 4 Results

The aim of this project has been to realize the double Fano cavity experimentally and investigate its transmission profile as a function of the incident wavelength. In this section I present the best results obtained and comment on these. Furthermore, I will outline challenges and obstacles that have been encountered, their implications on the data presented and my thoughts on immediate improvements for future experiments.

The results obtained have been so through an iterative process realizing the theory presented in previous sections. For this reason, the structure of this section will outline this process and thus begin by an in depth spectral analysis of the Fano mirrors used, as a pair matching in optical parameters, and especially the guided-mode resonance wavelength, is crucial in order to realize the Fano resonance. When moving on to the results regarding cavity characterization I will begin by briefly verifying the results for the single Fano cavity presented by Mitra et al. in [35]. Finally, I will show experimental results of the optical characterization of the double Fano cavity.

## 4.1 Fano mirror characterization

The first important step in realizing the double Fano cavity, is to locate a matching pair of Fano mirrors. A substantial spectral overlap is necessary in order to excite a Fano resonance including both guided-modes, as explained in section 2.4.5. For this reason the Fano mirrors considered were all fabricated externally by *Norcada* and from the same "batch", as these were initially considered to have a greater probability of having similar physical attributes. Many Fano mirrors were thus characterized during the process of finding a match, and the pair eventually chosen to move forward with were denoted *G1* and *G2*.

Figure 54 shows the individual measured normalized reflection and transmission spectra of G1 and G2 together with a least squares fit to the model derived in section 2.2. The corresponding optical parameters for each Fano mirror were found as the following.

Fitting parameters for G1:

$$\begin{aligned} \lambda_{0,G1} &= 951.764\text{nm}, \quad \lambda_{1,G1} = 951.901\text{nm}, \quad t_d = 0.814, \\ r_d &= 0.575, \quad \gamma_\lambda = 0.462\text{nm}, \quad \beta = 9 \cdot 10^{-7}\text{nm}^{-1}. \end{aligned} \tag{61}$$

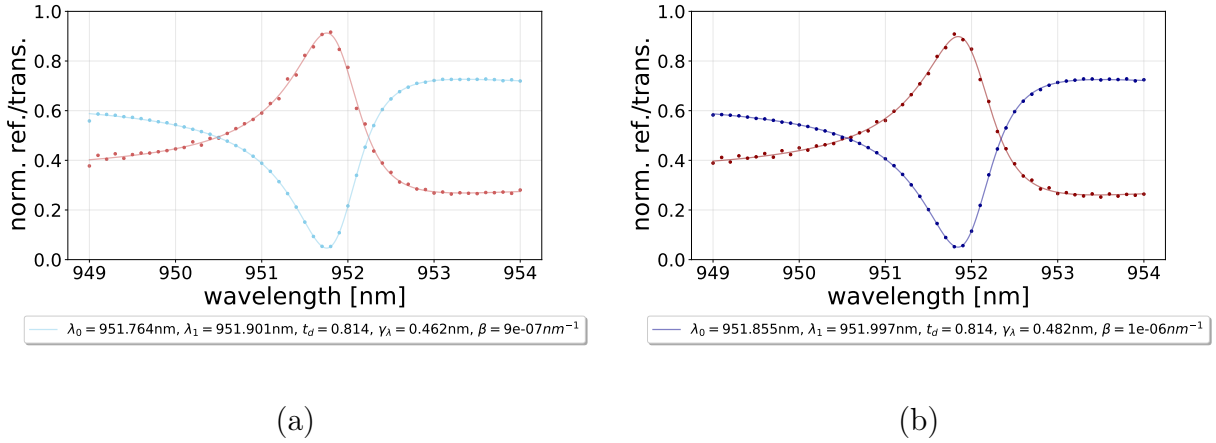


Figure 54: (a) shows the normalized reflection and transmission spectra of Fano mirror G1 along with its optical parameters found as fitting parameters from a least squares fit to the model derived in section 2.2. (b) shows the same for Fano mirror G2. Spectra of Fano mirrors that were characterized but not included in further experiments can be found in Appendix B.

Fitting parameters for G2:

$$\begin{aligned} \lambda_{0,G2} &= 951.855\text{nm}, \quad \lambda_{1,G2} = 951.997\text{nm}, \quad t_d = 0.814, \\ r_d &= 0.570, \quad \gamma_\lambda = 0.482\text{nm}, \quad \beta = 1 \cdot 10^{-6}\text{nm}^{-1}. \end{aligned} \quad (62)$$

In order to evaluate and compare the parameters to determine whether the two Fano mirrors are in fact a good match, they are both shown alongside each other in figure 55 for spectral comparison. Each their resonance wavelengths  $\lambda_0$  are indicated on the figure and the detuning can thus be estimated as

$$\Delta = |\lambda_{0,G2} - \lambda_{0,G1}| = 951.855\text{nm} - 951.764\text{nm} = 0.091\text{nm}. \quad (63)$$

Here we remember that the additional fitting parameters, namely  $t_d$ ,  $r_d$ ,  $\gamma_\lambda$  and  $\beta$ , are assumed identical in the model for the double Fano cavity outlined in section 2.4.2 and these are thus compared in a more qualitative manner. Whether the parameters in eqs. (61) and (62) can be assumed identical is completely individual to the given experiment and the corresponding acceptable margins. In order to move forward, G1 and G2 are assumed to only differ in guided-mode resonance wavelength.

As is shown in section 2.4.6, a spectral detuning leads to a spatial detuning, meaning that the cavity length corresponding to the guided-mode resonance

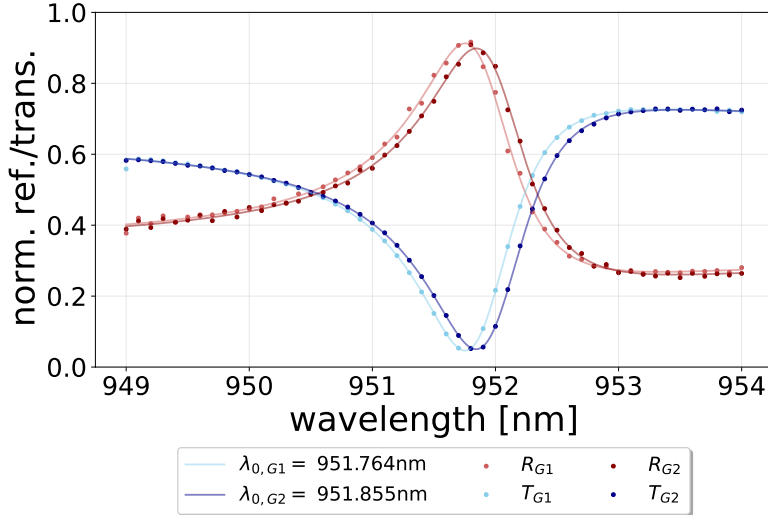


Figure 55: Spectral comparison of Fano mirrors G1 and G2. The spectra are the same shown in figure 54.

wavelength for G1 and G2 are not identical as they have a non-zero detuning  $\Delta$ . In order to sustain a Fano resonance it is equally important, and in fact equivalent to the spectral overlap, that the Fano mirrors have overlapping cavity transmission profiles as a function of the cavity length. Figure 56 shows the simulated double Fano transmission of a cavity consisting of G1 and G2 for lengths corresponding to their guided-mode resonance wavelengths. It is readily seen that the two transmission profiles overlap for the included example of a cavity of length  $l \approx 30\mu\text{m}$ .

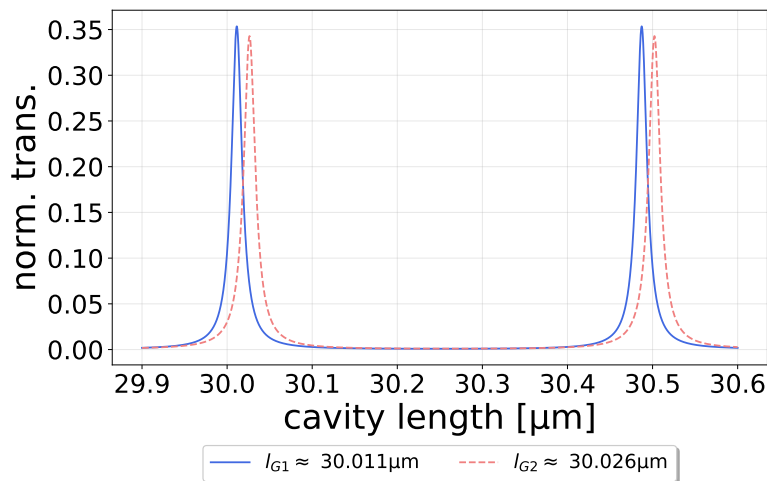


Figure 56: Simulated length scans of double Fano cavities with incident wavelengths of  $\lambda_{0,G1}$  and  $\lambda_{0,G2}$ . The corresponding lengths determined from the scans are denoted  $l_{G1}$  and  $l_{G2}$ , respectively.

## 4.2 The single Fano cavity

We recall that the single fano cavity consists of a Fano mirror and a broadband mirror in a plane-plane configurations where each mirror is perpendicular to the optical axis. The single Fano cavity configuration is briefly outlined in section 3.3 and otherwise shown in [35], it however resembles the double Fano cavity setup shown in figure 30, except only the bottom two xy-stages are used, and the top ones are therefore removed.

The mirror used is a high reflective (HR) broadband mirror with a reflectivity of 99.7%, meaning that effectively all intrinsic cavity losses can be assumed to be associated with the Fano mirror. The Fano mirror used is G1 characterized in section 4.1.

Figure 57 shows examples of off-resonance spectra of the single Fano cavity, with corresponding fits to the Fabry-Perot transmission function, in order to determine the cavity length from the measured FSR. Figure 57a shows the off-resonance spectrum for a cavity of length  $l = 57.40 \pm 1.55\mu m$ , while figure 57b shows the same for a cavity length of  $l = 211.98 \pm 3.16\mu m$ . The errors are determined as the errors of the fit, found as the squareroot of the diagonal of the corresponding covariance matrices.

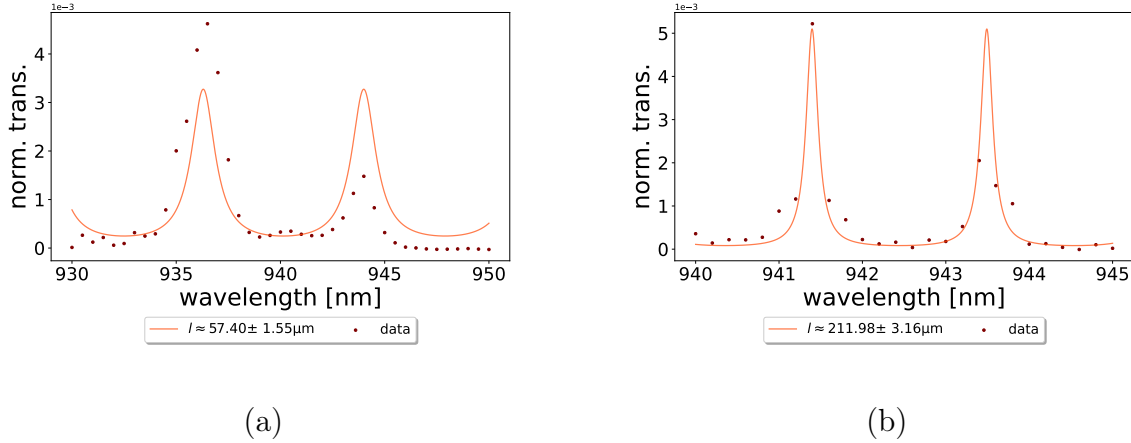


Figure 57: (a) shows an off-resonance wavelength scan of single Fano cavity consisting of a HR broadband mirror and G1 for a cavity length of  $l = 57.40 \pm 1.55\mu m$ . (b) shows this for a single Fano cavity of length  $l = 211.98 \pm 3.16\mu m$ . Each length is determined from these measurements by measuring the FSR and utilizing that  $l = \lambda_0^2 / (2 \cdot FSR)$ .

Figure 58 shows examples of resonance transmission spectra of the single Fano

cavity. The examples are taken for lengths corresponding to the ones found from the off-resonance spectra shown in figure 57 above. The figures are depicted with each their corresponding least squares fits to the generalized Fano model shown in eq. (33) in order to determine the linewidth (HWHM) of the profile. The errors of the linewidths are here found from the error of the fit and are mainly used to determine the quality of the measurement.

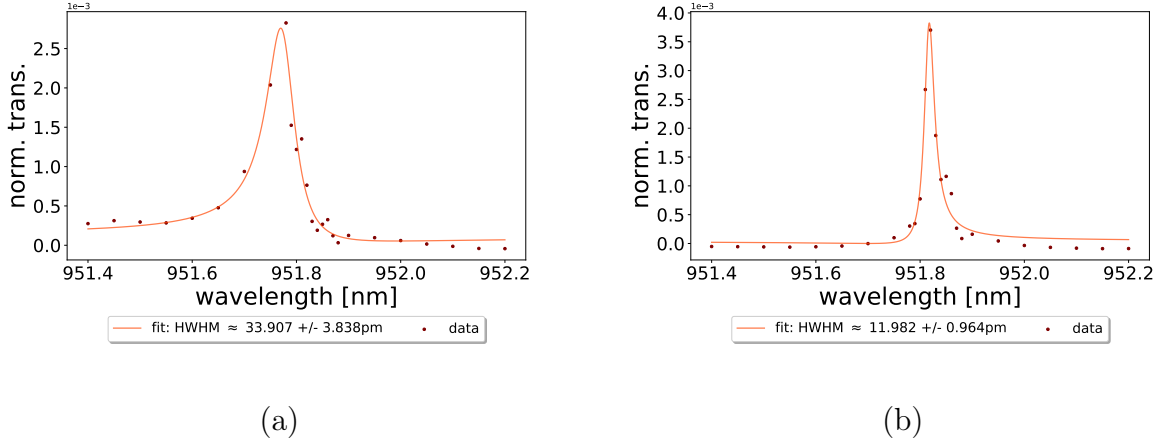


Figure 58: Single Fano resonance transmission profiles of a cavity consisting of a HR broadband mirror of reflectivity  $R = 99.7\%$  and Fano mirror G1. (a) shows the profile of a cavity of length  $l = 57.40 \pm 1.55\mu m$  and displays a linewidth of  $HWHM = 33.907 \pm 3.838\text{pm}$ . (b) shows the profile of a cavity of length  $l = 211.98 \pm 3.16\mu m$ , with a linewidth of  $HWHM = 11.982 \pm 0.964\text{pm}$ .

At each cavity length, the resonance transmission profile was recorded a number of times and the average value was taken to be the true found value of the linewidth. Figure 59 shows the result of a measurement series consisting of five cavity lengths approximately ranging from  $20\mu m \leq l \leq 400\mu m$ , where the error of each measurement is given as the standard deviation of the values of all measurements recorded at each cavity length[60]. The error depicted in the x-direction is found from the error of the fit of the Fabry-Perot transmission function to the off-resonance spectra. The blue dashed line indicates the linewidth of a broadband cavity of similar losses according to eq. (35) and the orange dashed line indicates the analytical linewidth of the single Fano cavity considered consisting of G1 and the HR broadband mirror estimated using eq. (36). The black points are linewidths found by fitting single Fano transmission profiles simulated using eq. (32) to the generalized Fano model in eq. (33) for comparison.

It is seen that the analytical model, the simulated linewidths and the measured linewidths coincide very well for the cavity lengths that are well-within the Fano regime and deviates slightly for longer lengths. This trend agrees nicely with what has previously been found for the single Fano cavity transmission[35] and is likely a consequence of the very narrow linewidths of the cavity in the standard regime, as this increases the sensitivity to any noise regarding the cavity length, e.g. mechanical vibrations in the setup.

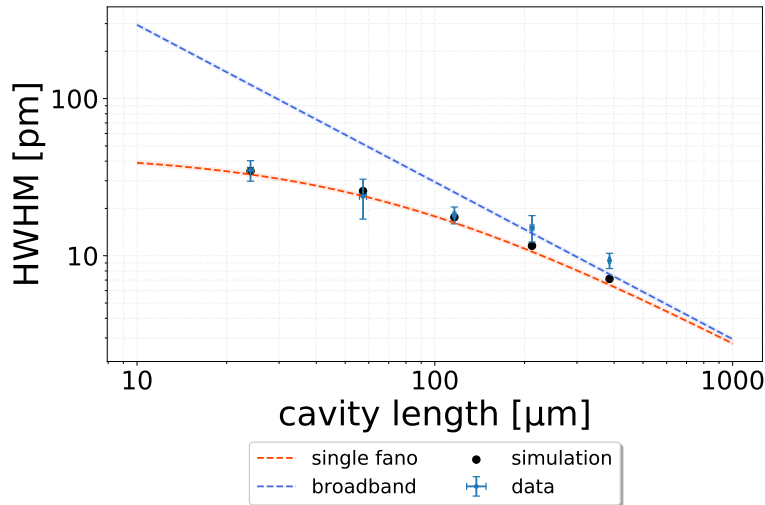


Figure 59: The linewidth (HWHM) as a function of resonant cavity length. The blue dashed line indicates the analytical linewidth for a broadband cavity, and the orange dashed line shows the corresponding analytical linewidth for a single Fano cavity of similar losses to the one realized experimentally. The blue points and corresponding errorbars shows the measured linewidths found as averages of all recorded values at each length and the error is found as the standard deviation of these values. The black points are the linewidths of simulated spectra. The spectra used to determine the points depicted can be found in Appendix F.

### 4.3 The double Fano cavity

In this section I will present of the results for the characterization of a double Fano cavity consisting of Fano mirrors G1 and G2. First we examine the simulated spectra of the double Fano transmission intensity profile as a function of the incident wavelength simulated with the parameters for G1 given in eq. (61) and for G2 given in eq. (62). Figures 60 and 61 shows the simulated spectra for cavity lengths according to  $l = l_{G1}$ ,  $l = l_{G2}$  and  $l = (l_{G1} + l_{G2})/2$  together with the reflection spectra for G1 and G2 also shown in figure 55.

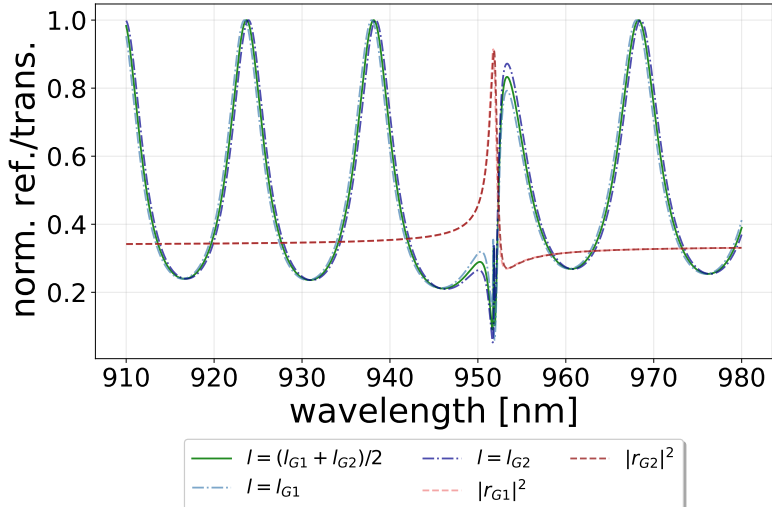


Figure 60: The simulated spectra of a double Fano cavity consisting of G1 and G2 for lengths  $l = l_{G1}$ ,  $l = l_{G2}$  and  $l = (l_{G1} + l_{G2})/2$ . The two red dashed lines are the normalized reflectivity intensities of G1 and G2, respectively, shown in figure 55. The range plotted is chosen as it resembles the tunable range of the Toptica laser used for the experiments of this project.

It is seen in figure 60 that the off-resonance level is expected to almost reach unity for a perfectly aligned cavity, for the given direct transmission/reflection coefficient amplitudes  $t_d$ ,  $t'_d$  and  $r_d$ ,  $r'_d$ . This result for the simulated spectra is indicative of the validity of the assumption that these are approximately identical meaning that  $t_{d,G1} \approx t_{d,G2}$  and  $r_{d,G1} \approx r_{d,G2}$ . Furthermore, the background perfectly resembles a low finesse Fabry-Perot cavity, as is expected from the theory.

Figure 61 shows the transmission spectra of the double Fano cavity zoomed on the resonance wavelengths considered according to the depicted cavity lengths.

Here it is seen how the transmission peak at resonance is expected to shift with the cavity length, and that the estimated detuning  $\Delta$  of the two Fano mirrors seems to be sufficiently small in order to realize the double Fano resonance profile. Lastly, it is seen what to expect in terms of the peak height of the resonance profile as this is an important merit when practically estimating the losses, and by extension the alignment, of the cavity in the lab.

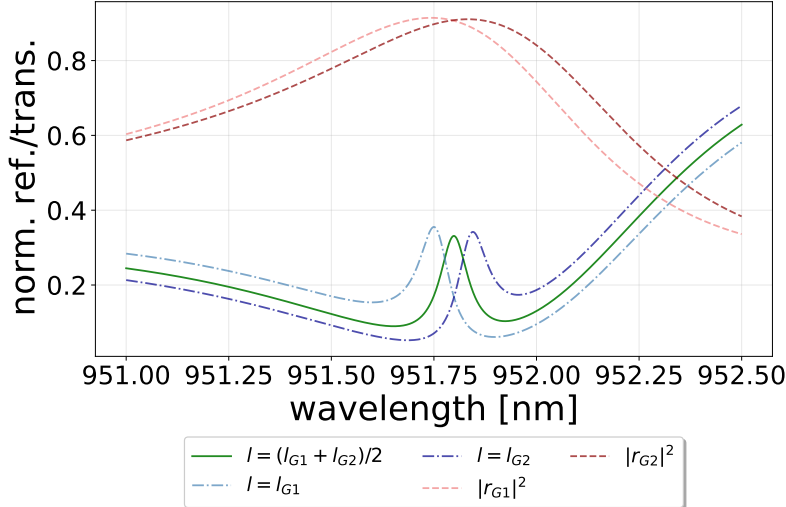


Figure 61: The simulated spectra of a double Fano cavity consisting of G1 and G2 for lengths  $l = l_{G1}$ ,  $l = l_{G2}$  and  $l = (l_{G1} + l_{G2})/2$  focused around the corresponding resonance wavelengths. The two red dashed lines are the normalized reflection intensities of G1 and G2, respectively. These are shown in figure 55.

The transmission profile for different cavity length where simulated in order to determine the optimal value. Figure 62 shows a colormap of the resonance profile as a function of wavelength and cavity length ranging  $l_{G1} \leq l \leq l_{G2}$ . The signal intensity is indicated by the brightness of the colormap, such that the resonance wavelength and cavity length is indicated by the "line" showing the resonance peak moving in terms of both parameters.

The colormap provides a qualitative and intuitive image of the behaviour of the double Fano transmission profile, but the optimal cavity length in order to optimize with respect to the linewidth is nearly impossible to determine from this alone. Figure 63 instead shows the linewidth of intracavity spectra as a function of the cavity length and shows that the optimal cavity length is

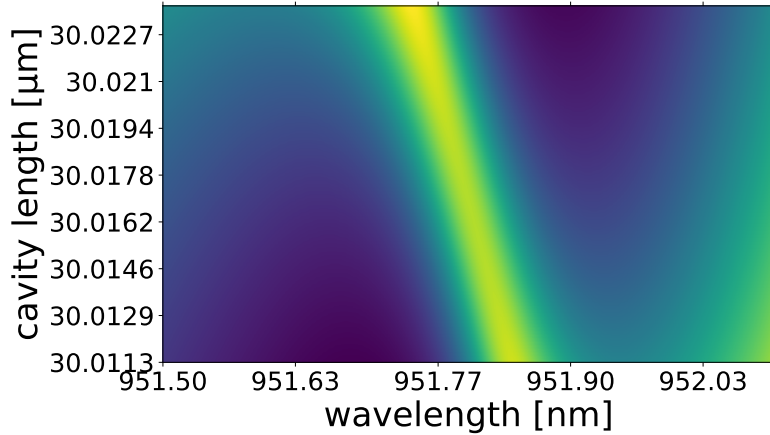


Figure 62: Colormap of the resonance transmission profile of the double Fano cavity consisting of G1 and G2. The brightness of the colormap indicates the intensity/peak height while the varied parameters are the wavelength and cavity length ranging  $l_{G1} \leq l \leq l_{G2}$ .

approximately given as  $l \approx (l_{G1} + l_{G2})/2$ . In reality, the asymmetric structure of the Fano mirror spectra results in an exact answer to the optimal cavity length that is more complicated, and likely impossible to realize in the lab. For this reason the approximate interpretation of the cavity length analysis is sufficient for practical purposes.

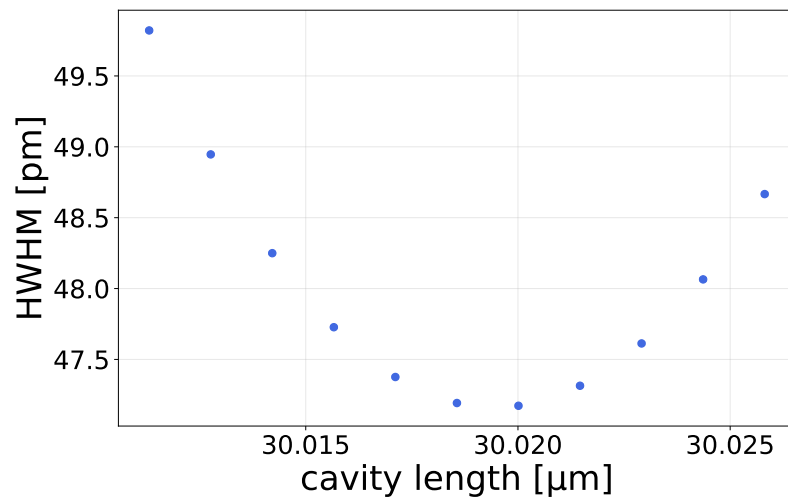


Figure 63: The simulated intracavity linewidth as a function of cavity length ranging  $l_{G1} \leq l \leq l_{G2}$ . Each linewidth is found by fitting simulated spectra to the generalized Fano model in eq. (33).

### 4.3.1 Realizing the double fano model

In order to realize the double Fano model in a satisfying way a relatively broad spectrum is examined as the off-resonance profile resembling a low-finesse Fabry-Perot transmission spectrum, with near-unity transmission levels at each Fabry-Perot resonance peak, is considered a defining feature of the double Fano cavity. In this section I will present three spectra obtained experimentally and compared with corresponding simulated spectra for lengths  $l = l_{G1}$ ,  $l = l_{G2}$  and  $l = (l_{G1} + l_{G2})/2$ . Furthermore, I present the same experimental spectra fitted to the double Fano cavity transmission model with varied fitting parameters. The first two spectra presented have been fitted with fitting parameters given by  $\lambda_{0,G1}$ ,  $\lambda_{1,G1}$ ,  $\lambda_{0,G2}$ ,  $\lambda_{1,G2}$ ,  $l$  and  $L$ , where  $l$  is the cavity length and  $L = 1 - |r|^2$  is the cavity losses. The last spectrum presented proved unable to agree well with the model given the aforementioned fitting parameters, and for this reason all Fano mirror parameters for both G1 and G2 are considered variable in this fit along with the cavity length  $l$  and cavity losses  $L$ .

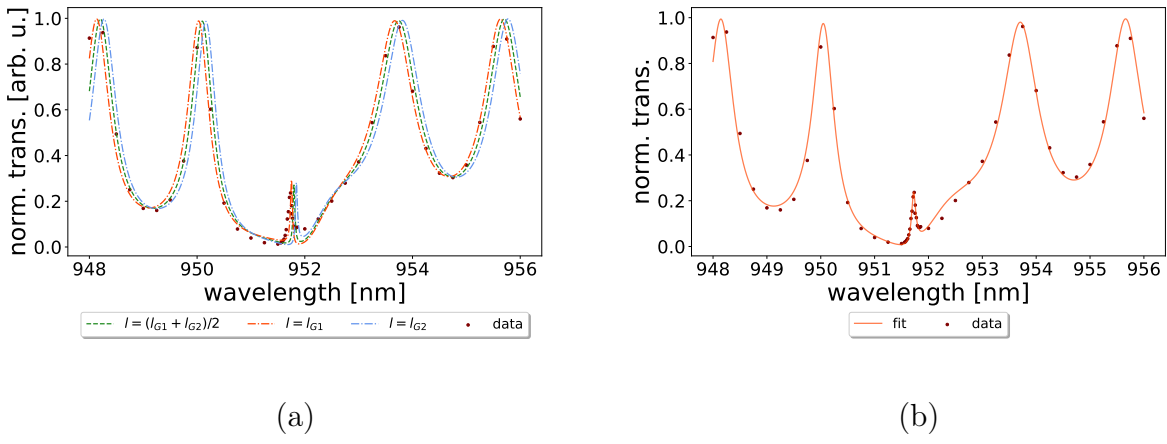


Figure 64: (a) shows recorded data of the double Fano cavity transmission compared with simulated spectra for cavity lengths of  $l_{G1} = 239.3975\mu m$ ,  $l_{G2} = 239.4317\mu m$  and  $(l_{G1} + l_{G2})/2 = 239.4146\mu m$ . (b) shows a least squares fit of the recorded data to the double Fano cavity transmission model in eq. (37).

Figure 64a show the comparison of data and simulation for a cavity of lengths given as  $l_{G1} = 239.3975\mu m$ ,  $l_{G2} = 239.4317\mu m$  and  $(l_{G1}+l_{G2})/2 = 239.4146\mu m$ . Figure 64b shows a least squares fit of the recorded data to the double Fano transmission function with fitting parameters found as

$$\lambda_{0,G1} = 951.509 \pm 0.036\text{nm}, \quad \lambda_{1,G1} = 951.586 \pm 0.107\text{nm} \quad (64)$$

for Fano mirror G1,

$$\lambda_{0,G2} = 951.782 \pm 0.041\text{nm}, \quad \lambda_{1,G2} = 951.934 \pm 0.058\text{nm} \quad (65)$$

for Fano mirror G2, and

$$l = 238.925 \pm 0.002\mu\text{m}, \quad L = 0.178 \pm 0.038 \quad (66)$$

for the cavity length and losses.

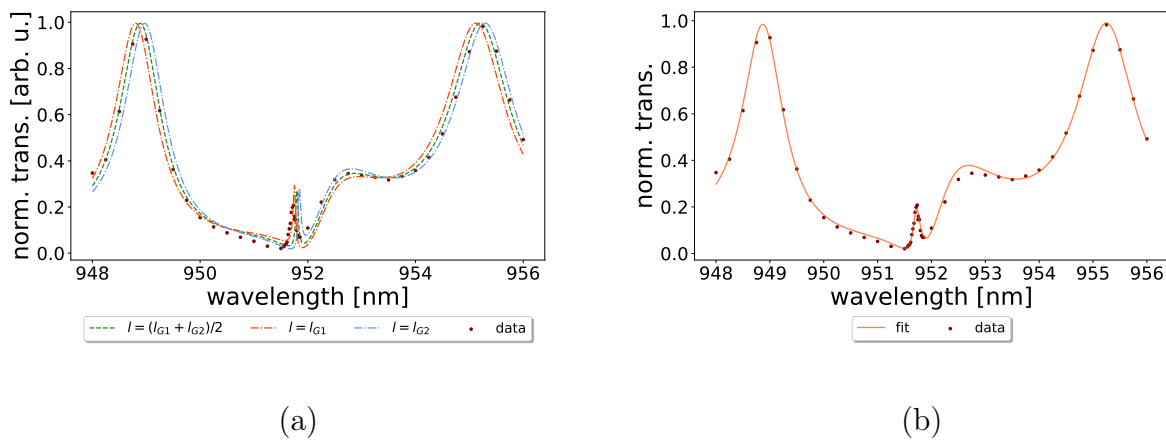


Figure 65: (a) shows recorded data of the double Fano cavity transmission compared with simulated spectra for cavity lengths of  $l_{G1} = 140.4152\mu\text{m}$ ,  $l_{G2} = 140.4401\mu\text{m}$  and  $(l_{G1} + l_{G2})/2 = 140.4277\mu\text{m}$ . (b) shows a least squares fit of the recorded data to the double Fano cavity transmission model in eq. (37).

Figure 65a shows the comparison of data and simulation for a cavity of lengths given as  $l_{G1} = 140.4152\mu\text{m}$ ,  $l_{G2} = 140.4401\mu\text{m}$  and  $(l_{G1}+l_{G2})/2 = 140.4277\mu\text{m}$ . Figure 65b shows a least squares fit of the recorded data to the double Fano transmission function with fitting parameters found as

$$\lambda_{0,G1} = 951.546 \pm 0.015\text{nm}, \quad \lambda_{1,G1} = 951.719 \pm 0.040\text{nm} \quad (67)$$

for Fano mirror G1,

$$\lambda_{0,G2} = 951.868 \pm 0.016\text{nm}, \quad \lambda_{1,G2} = 951.963 \pm 0.039\text{nm} \quad (68)$$

for Fano mirror G2, and

$$l = 139.953 \pm 0.001 \mu m, \quad L = 0.293 \pm 0.033 \quad (69)$$

for the cavity length and losses.

The additional optical parameters for G1 and G2,  $t_d$ ,  $\gamma_\lambda$  and  $\beta$ , are kept constant for the cavities of lengths  $l \approx 239 \mu m$  and  $l \approx 139 \mu m$ , and are thus given in eqs. (61) and (62). The choice of fixed and variable parameters in the least squares fit is justified by the angular dependence of the guided-mode resonance wavelength outlined in [42]. It is hence evident that  $\lambda_0$  and  $\lambda_1$  potentially shifts slightly for different measurements and is for this reason denoted a variable fitting parameter. The additional optical parameters mentioned above have shown to be constant, even for slight misalignments, and are therefore rightly fixed when fitting.

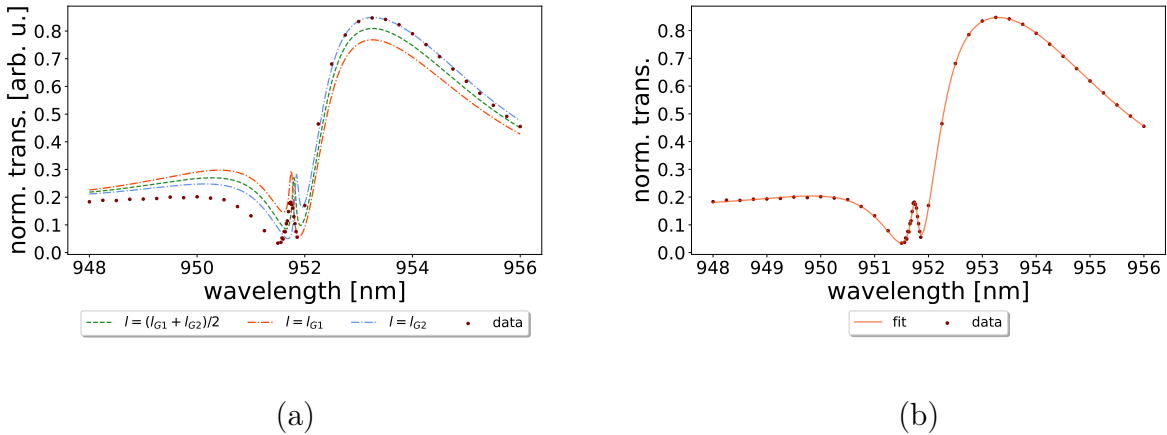


Figure 66: (a) shows recorded data of the double Fano cavity transmission compared with simulated spectra for cavity lengths of  $l_{G1} = 33.3424 \mu m$ ,  $l_{G2} = 33.3573 \mu m$  and  $(l_{G1} + l_{G2})/2 = 33.3499 \mu m$ . (b) shows a least squares fit of the recorded data to the double Fano cavity transmission function with fitting parameters related to each Fano mirror, and the cavity as follows.

Figure 66a shows the comparison of data and simulation for a cavity of lengths  $l_{G1} = 33.3424 \mu m$ ,  $l_{G2} = 33.3573 \mu m$  and  $(l_{G1} + l_{G2})/2 = 33.3499 \mu m$ . Figure 66b shows a least squares fit of the data to the double Fano transmission function with fitting parameters related to each Fano mirror, and the cavity as follows.

Fano mirror  $G1$  fitting parameters:

$$\begin{aligned}\lambda_{0,G1} &= 951.532 \pm 0.008\text{nm}, \quad \lambda_{1,G1} = 951.689 \pm 0.074\text{nm}, \quad t_d = 0.817 \pm 0.027, \\ \gamma_\lambda &= 0.421 \pm 0.134\text{nm}, \quad \beta = 1.047 \cdot 10^{-6} \pm 4.947 \cdot 10^{-8}\text{nm}^{-1}.\end{aligned}\tag{70}$$

Fano mirror  $G2$  fitting parameters:

$$\begin{aligned}\lambda_{0,G2} &= 951.853 \pm 0.004\text{nm}, \quad \lambda_{1,G2} = 951.919 \pm 0.017\text{nm}, \quad t_d = 0.754 \pm 0.033, \\ \gamma_\lambda &= 0.563 \pm 0.079\text{nm}, \quad \beta = 5.245 \cdot 10^{-7} \pm 2.823 \cdot 10^{-8}\text{nm}^{-1}.\end{aligned}\tag{71}$$

Cavity parameters (length and losses):

$$l = 30.984 \pm 0.006\mu\text{m}, \quad L = 0.017 \pm 0.184.\tag{72}$$

As all parameters describing each Fano mirror and the cavity configuration are kept as variables, it is not surprising that the fit in figure 66b agrees very well with the recorded data. However, even though this discredits the validity of this fit as an argument for the realization of the presented model, it is worth noting that most of the parameters agree well with the ones presented in figure 54 within the estimated errors. The only exceptions are  $\lambda_{0,G1}$ ,  $\lambda_{1,G1}$  and  $t_{d,G2}$ , and considering that the discrepancy of the guided-mode resonance wavelength can be argued to be due to alignment variations, this fit too presents promising results for the realization of the model.

## Comparison with simulations

In all cases shown above the data and corresponding simulation mostly shows remarkable overlap and agreement, as most data points are placed within, or very close to, the area enclosed by the simulations for the three considered cavity lengths. While this is only a qualitative measure, it indicates a high level of predictive strength of the model outlined in section 2.2 and eq. (37) and likewise for the experimental method used shown in section 3.3.

## Fits to the double Fano model

All optical parameters for G1 and G2 found as fitting parameters of the double Fano model are approximately in agreement with the ones found for G1 and G2

in section 4.1 which are used to simulate the transmission spectra and assumed the baseline for determining the validity of the values found in this section. While they are only approximately in agreement, it is noted that the values tend to shift slightly based on the alignment of the experimental setup. With this in mind the optical parameters found provide a satisfactory foundation, along with the comparisons to the simulations, to argue for the realization of the double Fano model proposed. It is my conclusion that the model performs very well in describing the recorded data.

### 4.3.2 The double fano linewidth

As for the single Fano cavity in section 4.2, we present resonance transmission spectra and compare the found linewidths with the ones of simulated spectra and the analytical model presented in eq. (38). The double Fano cavity realized is one comprised of Fano mirrors G1 and G2, characterized in section 4.1, in a plane-plane configuration placed normal to the optical axis. As the single Fano cavity was comprised of G1 and a HR broadband mirror, it is expected that the double Fano cavity produces spectra with broader linewidths due to the relatively higher losses. When comparing with the single Fano cavity linewidths, it must thus be noted that this is a single Fano cavity of similar losses as the double Fano cavity, and *not* the one presented in section 4.2.

Figure 67 shows examples of off-resonance spectra of the double Fano cavity, with corresponding fits to the Fabry-Perot transmission function in order to determine the cavity length from the measured FSR. Figure 67a shows the off-resonance spectrum for a cavity of length  $l = 17.04 \pm 0.23\mu m$ , while figure 67b shows the same for a cavity of length  $l = 539.10 \pm 2.33\mu m$ . The errors are determined as the errors of the fits, found as the squareroot of the diagonal of the corresponding covariance matrices.

Figure 68 shows examples of resonance transmission spectra of the double Fano cavity. The examples are taken for length corresponding to the ones found from the off-resonance spectra shown in figure 67 above. The figures are depicted with each their corresponding least squares fits to the generalized Fano model shown in eq. (33) in order to determine the linewidth (HWHM) of the profile. The errors of the linewidths are found from the error of each fit and are mainly used to determine the quality of the measurement.

Figure 69 shows the average of results for the linewidths of a number of recorded spectra taken for cavity lengths in the approximate range  $15\mu m \leq l \leq 1000\mu m$ .

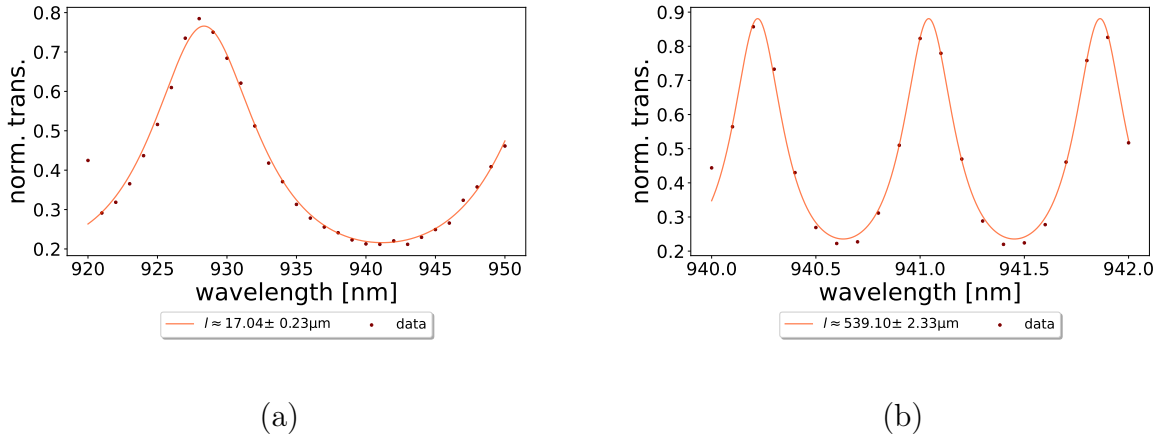


Figure 67: (a) shows an off-resonance wavelength scan of the double Fano cavity consisting of a G1 and G2 for a cavity length of  $l = 17.04 \pm 0.23\mu m$ . (b) shows this for a double Fano cavity of length  $l = 539.10 \pm 2.33\mu m$ . Each length is determined from these measurements by measuring the FSR and utilizing that  $l = \lambda_0^2 / (2 \cdot FSR)$ .

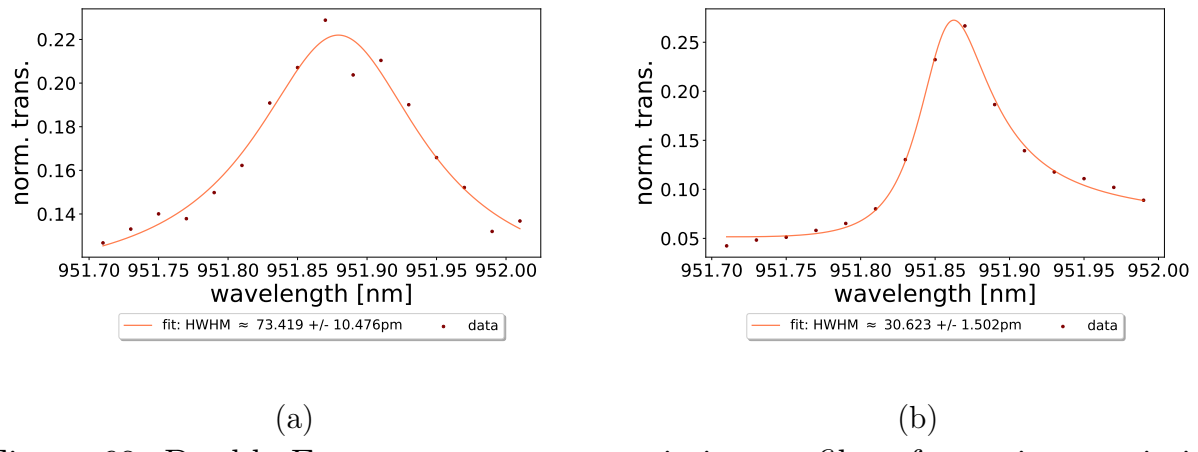


Figure 68: Double Fano resonance transmission profiles of a cavity consisting of Fano mirrors G1 and G2. (a) shows the profile of a cavity of length  $l = 17.04 \pm 0.23\mu m$  and displays a linewidth of  $HWHM = 73.419 \pm 10.476 pm$ . (b) shows the profile of a cavity of length  $l = 539.10 \pm 2.33\mu m$ , with a linewidth of  $HWHM = 30.623 \pm 1.502 pm$ .

The error of each data point depicted is determined as the standard deviation of all values found for the linewidth at that particular cavity length. The error in the x-direction, i.e. for the cavity lengths found from fits as the ones shown in figure 67 were of negligible size and are thus indicated rightly in the size

of the data points themselves. The blue dashed line depicts the analytical linewidth of a broadband cavity of losses similar to the double Fano cavity realized experimentally, the line is calculated using eq. (35). The orange dashed line similarly shows the analytical linewidth of the single Fano cavity calculated using eq. (36) for a cavity of similar losses. Lastly, the green dashed line indicates the analytical linewidth of the double Fano cavity transmission spectra comparable with the data points depicted. The black points are linewidths found by fitting double Fano transmission profiles simulated using eq. (37) to the generalized Fano model in eq. (33) for comparison.

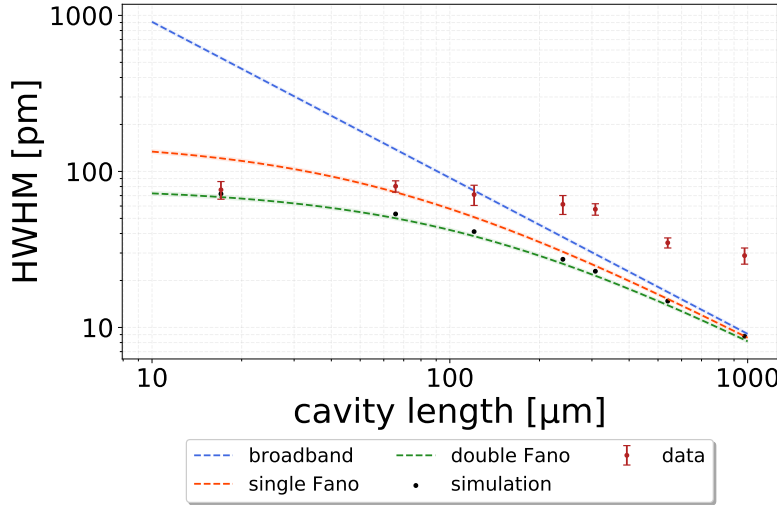


Figure 69: The linewidth (HWHM) as a function of resonant cavity length. The blue, orange and green dashed lines show the analytical linewidths of a broadband-, single Fano- and double Fano cavity of similar losses calculated using eqs. (35), (36) and (38). The optical parameters for G1 and G2 used for these calculations are determined from spectra re-recorded on the same day as the linewidth measurements for optimal comparison, this will be discussed in section 4.4. The dark red point and corresponding errorbars shows the measured linewidths found as averages of all recorded values at each length and the error is found as the standard deviation of these. The black points are the linewidths of simulated spectra. The spectra used to determine the points depicted can be found in Appendix G.

It is seen that the analytical and simulated linewidths are strongly correlated, which indicates that both describe the transmission spectra well. This is also indicated in section 4.3.1 where the realization of the double Fano model is

shown to correlate well with the spectra produced. However, when examining the measured linewidths of the double Fano cavity resonance transmission profile, it is clear that it deviates from the analytical and simulated ones. The double Fano cavity has shown to be very sensitive to vibrational and acoustic noise, and this becomes more apparent when increasing the cavity length. Note that the correlation between the analytical and measured linewidths becomes correspondingly stronger for decreasing cavity lengths, and that they overlap almost completely when considering the spectra at  $l \approx 17\mu m$ . This indicates that analytical double Fano cavity linewidths are roughly realizable inside the Fano regime. It is also noted that the behavior of the measured linewidth as a function of cavity length follows the trend of the analytical one, indicating that the Fano- and standard regimes are still applicable for the double Fano cavity.

While vibrational and acoustic noise definitely claims their part of the reason for the experienced broadening, the method used in order to align the double Fano cavity outlined in section 3.2.1 too has potential for improvement. When going through the process of aligning the cavity, one relies on the assumption that the top and bottom parts of the cavity setup can be removed and re-inserted without loss of alignment in either of the numerous degrees of freedom. This is of course not always the case and is therefore a cause of misalignment of the cavity and thus broadening.

Designing a setup and method with complete independent control of all degrees of freedom is therefore an area of improvement that could likely reduce the discrepancy of the analytical/simulated and measured linewidths of the double Fano cavity resonance transmission spectra.

## 4.4 Additional discussion

### 4.4.1 Vibrational noise

The aforementioned vibrational noise was apparent from the intial iteration of the double Fano cavity setup and it was quickly concluded that it was specifically related to the modifications made to the single Fano cavity setup in order to be able to control additional degrees of freedom needed.

Especially the translational degrees of freedom seemed to be the source of the vibrations, as the need to control these for the bottom and top Fano mirrors independently introduced the possibility of *uncoupled mechanical vibrations*. It is assumed that the noise was always apparent in the setup, but since the

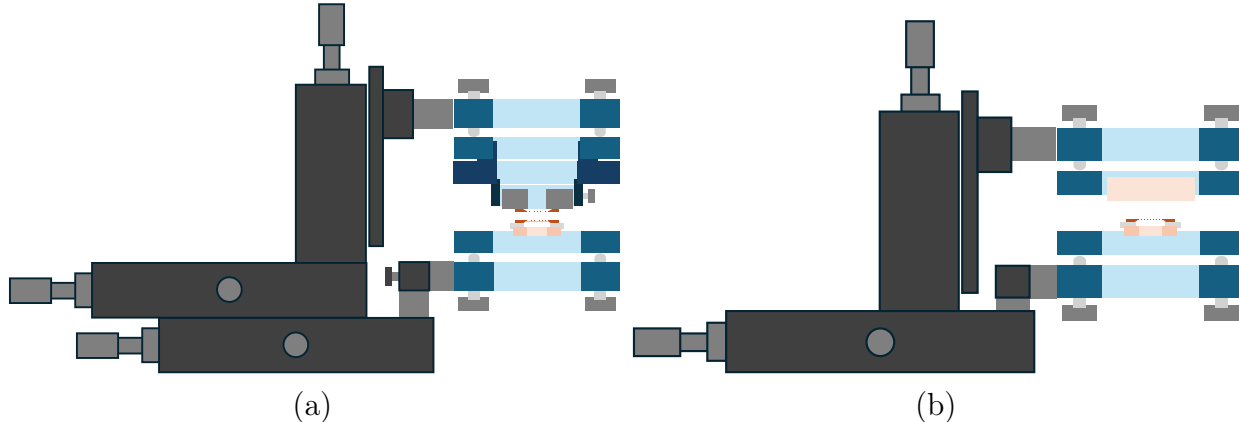


Figure 70: Simple sketches of the setups used to record the data shown in sections 4.2 and 4.3. (a) shows the double Fano cavity setup, and (b) shows the single Fano cavity setup.

broadband- and Fano mirrors of the single Fano cavity only ever had the need for relative motion in the z-direction, this was never expressed as a change in the cavity length, and this was thus constant during measurements. The linear stage used in the z-direction (*NFL5DP20*) was specifically chosen to include a piezo actuator for high resolution motion control for very short cavity lengths, and this proved to be virtually stable in terms of vibrations. While a number of different stages, with a longer maximum travel range, was tested for the xy-directions, none proved stable enough to completely cancel the uncoupled vibrations. Figure 70 shows sketches of the single- and double Fano cavity setups and it is here shown how the top and bottom of the setup was *uncoupled* through the addition of the xy-stages for aligning the top Fano mirror, while for the single Fano setup they were *coupled* as they were both attached to the same set of xy-stages.

Initially, the vibrations had an amplitude comparable with the free stroke of the piezo actuator. This means that the fringes stemming from scanning the cavity length would hardly change when turning off the alternating current applied to the actuator, and thus a stable measurement was deemed impossible. At this point it was unclear whether the noise was acoustic in nature or if the vibrations originated somehow from the optical table. In order to rule out, or reduce, acoustic vibrations the setup was enclosed inside a plexi-glas box which was further equipped with a piece of noise reducing foam. This addition proved helpful as it roughly reduced the amplitude of the noise by a factor of 2, thus making the spectral profile resolvable and measurements possible.

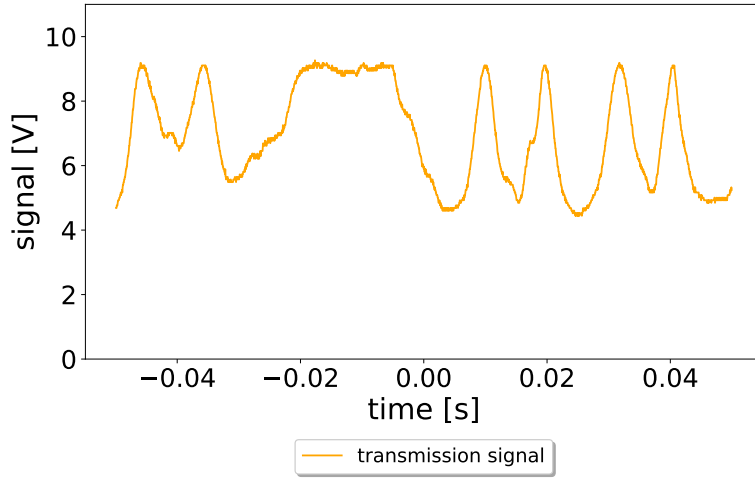


Figure 71: An example of the signal measured of the double Fano cavity transmission when manually scanning the piezo actuator to tune the cavity and guided-mode resonances. It is assumed that the cavity is resonant when the signal is maximized and that the fluctuations is due to vibrational noise. This naturally causes broadening and its effect is therefore apparent in the results presented.

Additional measures were taken in order to reduce any vibrations originating from the optical table by the addition of teflon slabs between the optical table and the first set of xy-stages, and between these and the second set of xy-stages. This further reduced the noise slightly and the resulting signal, shown as the raw data from the oscilloscope screen, is seen in figure 71.

It is assumed that the optimal cavity length is the one that produces the highest signal when the cavity length is constant. Keeping this in mind it is easily deduced from the figure that further noise reduction will increase the quality of the measured spectra. Since the intrinsically narrower linewidths produced by longer optical cavities (both standard- and Fano) makes these more sensitive to noise as the kind depicted in figure 71, this hints towards an explanation for the increased deviation from the analytical linewidth for longer cavity lengths seen in figure 69.

A brief decription of the plexi-glas box and teflon slabs are found in section 3.1.6.

Figure 72 shows the best obtained measurement series taken with the setup

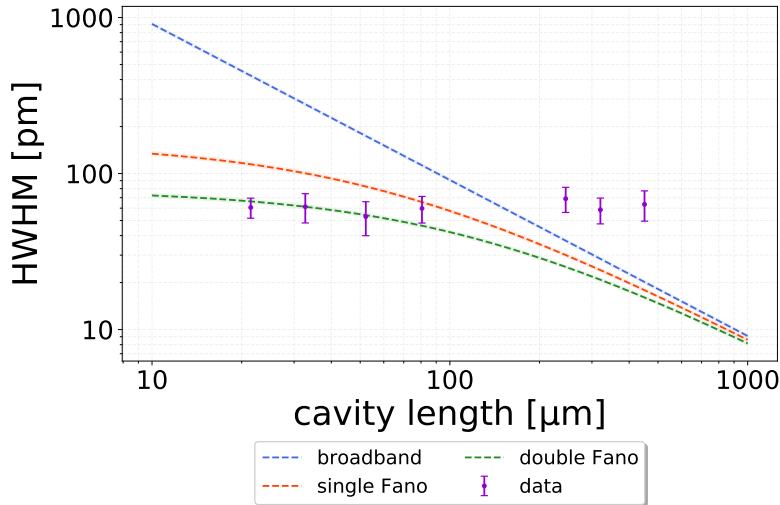


Figure 72: A measurement series showing the best obtained results for the double Fano cavity transmission linewidth as a function of resonant cavity length. This measurement series was recorded (before) the addition of the teflon slabs, which were added in an attempt to create a reflective interface to shield the cavity from vibrations propagating through the optical table. The spectra used to determine the points depicted can be found in Appendix G.

without teflon slabs, and while the cavity lengths considered does not range as far as the measurement series in figure 69, the trend of increased broadening in the standard regime is apparent. It also shows that even for the case of increased vibrational noise, it is possible to record spectra of linewidths in agreement with the analytical prediction, when inside the Fano regime. Note here that the errorbars on the figure are representative of the standard deviations of all values recorded at each cavity length, and thus the noisy measurement is seen to fluctuate more resulting in higher uncertainties.

#### 4.4.2 Guided-mode resonance shift

The spectra for G1 and G2 shown in figure 55 are taken individually and in the initial part of the project where finding a matching pair of Fano mirrors was the task at hand. Figure 73a shows, once again, the spectra of G1 and G2 taken individually, while figure 73b shows spectra taken for the two in the double Fano configuration at a later time.

It is apparent that while the spectra for G1 is virtually unchanged, the same

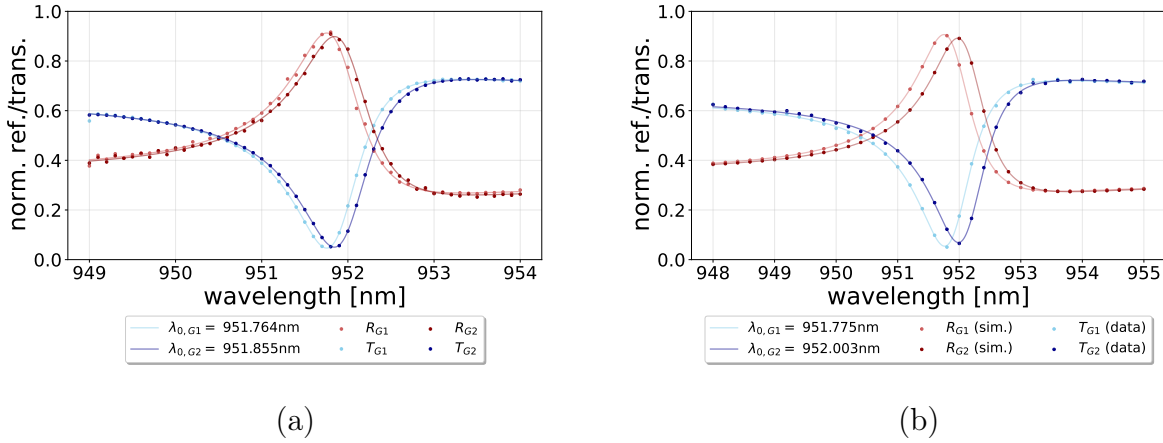


Figure 73: (a) shows spectra of G1 and G2 measured individually. (b) shows spectra of G1 and G2 in the double Fano configuration at a later time.

cannot be said for the spectra of G2 as this has clearly shifted to a slightly higher guided-mode resonance. This artifact has been observed several times in both this project and related projects in the same lab, as the resonance wavelength of *some* SiN sub-wavelength gratings tends to shift with time. An in-depth investigation of this behavior have to my knowledge not been conducted, however it is something that must be taken into account when evaluating recorded data. One considerable consequence of this is that all data presented must be recorded in the same measurement series, as measurements done on different days cannot be compared. It must be noted that the resonant guided-mode wavelength is very dependent on the alignment of a given Fano mirror, which could influence this behavior, it is however also apparent that the resonance tends to systematically shift to higher wavelengths only.

For optimal comparison, the parameters used to calculate the analytical linewidths in figures 69 and 72 are found as fitting parameters of spectra recorded on the same day as the measurements included in the each figure. The analytical linewidths have shown to only differ slightly for different spectra for G1 and G2, but the discrepancy is nonetheless not negligible and must hence be accounted for.

#### 4.4.3 Potential broadening due to walk-off effect

Another potential source of broadening is the so-called *walk-off effect* which is apparent, in this case, for the scenario of a wedge angle between G1 and G2. For a non-zero wedge angle the beam will be reflected inside the cavity and

propagate according to said wedge angle as simply sketched in figure 74. This would result in an effective change in the translational alignment of the beam relative to the Fano mirror/cavity, and thus broadening of the recorded spectra.

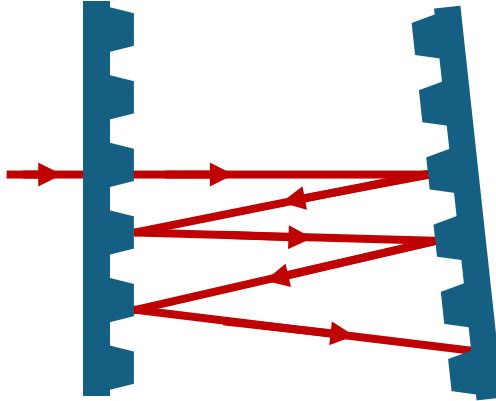


Figure 74: Sketch illustrating the walk-off effect between two Fano mirrors at a non-zero wedge angle.

A small, if not negligible, wedge angle is assumed for any experimentally realized cavity, but for the double Fano cavity with a non-zero detuning  $\Delta$  this might be enhanced by the method it self. In [42] it is shown that the resonance wavelength will increase for a Fano mirror of a non-zero incident angle at the cost of a higher (lower) minimum (maximum) transmission (reflectivity) when on resonance. The argument can be made that the optimal double Fano configuration for a non-zero detuning is not necessarily normal to the optical axis, but rather at a wedge angle which optimizes the spectral overlap of the two Fano mirrors. For this reason the angle between G1 and G2 might be increased when on-resonance measurements are recorded and hence the walk-off effect might contribute to the broadening seen in figure 69. The walk-off effect will, if apparent, naturally increase with the cavity length, as a simple geometric consequence of the configuration considered.

# 5 Conclusion

This project have been a textbook example of an iterative process of improving results one parameter at a time, with methods including both numerical predictions and an experimental trial-and-error approach. We have been able to achieve an almost complete overlap between the Fano theory for a plane-wave and the recorded data, and while broadening is still present in the resonance transmission spectra, I confidently conclude that the double Fano model have been successfully realized.

Using suspended *SiN* membranes patterned with sub-wavelength gratings, utilized as  $TM_0$  waveguides, we have successfully displayed an enhanced spectral sensitivity compared with a single Fano cavity of similar losses for short cavities, i.e. inside the Fano regime. It has been shown numerically that the double Fano cavity has the potential to produce linewidths similarly narrowed even for longer cavities, and the outlook of achieving this experimentaly is believed to belong in the near future.

The general behavior of the double Fano cavity has been thoroughly examined and documented through numerical simulations, once again assuming an incident plane-wave. The analytical model describing the linewidth of single- and double Fano cavities have likewise been studied and verified through both experimental and numerical results.

The realization of the double Fano cavity provides promise for a number of potential applications. These include, but are not limited to Fano cavity optomechanics, optical sensing and Fano lasers, and will be briefly outlines individually in the outlook section below.

## 5.1 Outlook

### 5.1.1 Matching analytical and experimental linewidths

I believe that the task of matching the analytical linewidth of the double Fano resonance transmission spectra with experimental data is one that consists of improving the method used and attempting to isolate the setup from vibrational noise stemming from outside sources. For this reason it is believed that this outlook is one that will be fulfilled in the near future.

### 5.1.2 Optomechanics with the double Fano cavity

This project have been dealing exclusively with the optical properties of the Fano mirrors. They are however often chosen for experiments in the field of cavity electrodynamics for their remarkable mechanical properties displaying high mechanical quality factors. Inside the Fano regime where the double Fano cavity linewidth is much narrower than for a similar broadband cavity of the same length, the radiation pressure is also high enough to excite mechanical modes in the high-Q *SiN* membranes. If placed inside a vacuum, the double Fano cavity is therefore an obvious candidate for studying optomechanical effects, e.g. the optical spring effect[36].

### 5.1.3 Sensing applications of the double Fano cavity

Various sensing applications using the bare *SiN* membranes are already being studied extensively. The isothermic compression of a gas in the free molecule regime inside a so-called membrane "sandwich" modifies the mechanical properties of the membranes due to the *squeeze film effect*. Figure 75 shows an example as a simple sketch of a double Fano cavity in a membrane "sandwich" configuration which can be utilized to measure absolute vapor pressure[22]. The change in mechanical properties of the Fano mirrors can then be recorded optically[20, 21].

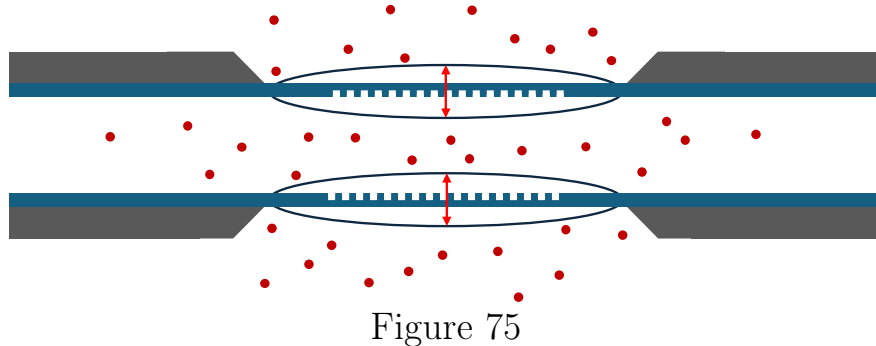


Figure 75

### 5.1.4 Fano laser based on bound states in the continuum

Firstly, a bound state in the continuum (BIC) is a state that remains localized while existing alongside a continuous spectrum of states that can provide and take away energy. They defy the general idea that states are either discrete or exist in a continuum. They are a relatively new discovery in the field of quantum mechanics, but have since been discovered to exist as a general wave phenomenon and can thus be utilized in numerous applications[62].

It has been proposed to utilize these BICs based on interference inside a cavity closely related to the double Fano cavity. This principle would allow for the construction of an ultra-coherent nanoscale laser, combating the limitation of quantum fluctuations, with potential applications in on-chip communication, photonic integrated circuits, bio/chemical sensing and quantum computing[63].

# References

- [1] S. Haroche. “A short history of Cavity Quantum Electrodynamics”. In: *Optical Society of America* (2007).
- [2] J. J. Sakurai and J. Napolitano. *Modern Quantum Mechanics (3rd ed.)* Cambridge University Press, 2020.
- [3] Juliette Monsel et al. “Dissipative and dispersive cavity optomechanics with a frequency-dependent mirror”. In: *Phys. Rev. A* 109 (4 Apr. 2024), p. 043532. DOI: 10.1103/PhysRevA.109.043532. URL: <https://link.aps.org/doi/10.1103/PhysRevA.109.043532>.
- [4] J. C. Sankey et al. “Strong and tunable nonlinear optomechanical coupling in a low-loss system”. In: *Nature Physics* 6.9 (June 2010), pp. 707–712. ISSN: 1745-2481. DOI: 10.1038/nphys1707. URL: <http://dx.doi.org/10.1038/nphys1707>.
- [5] Kerry J. Vahala. “Optical microcavities”. In: *Nature* 424.6950 (2003), pp. 839–846.
- [6] J. D. Thompson et al. “Strong dispersive coupling of a high-finesse cavity to a micromechanical membrane”. In: *Nature* 452.7183 (2008), pp. 72–75.
- [7] A M Jayich et al. “Dispersive optomechanics: a membrane inside a cavity”. In: *New Journal of Physics* 10.9 (Sept. 2008), p. 095008. ISSN: 1367-2630. DOI: 10.1088/1367-2630/10/9/095008. URL: <http://dx.doi.org/10.1088/1367-2630/10/9/095008>.
- [8] D. J. Wilson et al. “Cavity Optomechanics with Stoichiometric SiN Films”. In: *Phys. Rev. Lett.* 103 (20 Nov. 2009), p. 207204. DOI: 10.1103/PhysRevLett.103.207204. URL: <https://link.aps.org/doi/10.1103/PhysRevLett.103.207204>.
- [9] Andrew T. Land et al. “Sub-ppm Nanomechanical Absorption Spectroscopy of Silicon Nitride”. In: *Nano Letters* 24.25 (May 2024), pp. 7578–7583. ISSN: 1530-6992. DOI: 10.1021/acs.nanolett.4c00737. URL: <http://dx.doi.org/10.1021/acs.nanolett.4c00737>.
- [10] Yannick Seis et al. “Ground state cooling of an ultracoherent electromechanical system”. In: *Nature Communications* 13.1 (2022), p. 1507.
- [11] Andrea Cupertino et al. “Centimeter-scale nanomechanical resonators with low dissipation”. In: *Nature Communications* 15.1 (2024), p. 4255.

- [12] T. Bagci et al. “Optical detection of radio waves through a nanomechanical transducer”. In: *Nature* 507.7490 (2014), pp. 81–85.
- [13] R. W. Andrews et al. “Bidirectional and efficient conversion between microwave and optical light”. In: *Nature Physics* 10.4 (2014), pp. 321–326.
- [14] Mitul Dey Chowdhury, Aman R. Agrawal, and Dalziel J. Wilson. “Membrane-Based Optomechanical Accelerometry”. In: *Phys. Rev. Appl.* 19 (2 Feb. 2023), p. 024011. DOI: 10.1103/PhysRevApplied.19.024011. URL: <https://link.aps.org/doi/10.1103/PhysRevApplied.19.024011>.
- [15] Jack Manley et al. “Searching for Dark Matter with an Optomechanical Accelerometer”. In: *Conference on Lasers and Electro-Optics*. Optica Publishing Group, 2021, STh2Q.2. DOI: 10.1364/CLEO\_SI.2021.STh2Q.2. URL: [https://opg.optica.org/abstract.cfm?URI=CLEO\\_SI-2021-STh2Q.2](https://opg.optica.org/abstract.cfm?URI=CLEO_SI-2021-STh2Q.2).
- [16] Elías Ferreiro-Vila et al. “Micro-Kelvin Resolution at Room Temperature Using Nanomechanical Thermometry”. In: *ACS Omega* 6.36 (Sept. 2021), pp. 23052–23058.
- [17] Chang Zhang et al. “Radiative Heat Transfer in Freestanding Silicon Nitride Membranes”. In: *Phys. Rev. Appl.* 14 (2 Aug. 2020), p. 024072. DOI: 10.1103/PhysRevApplied.14.024072. URL: <https://link.aps.org/doi/10.1103/PhysRevApplied.14.024072>.
- [18] Bhagya Nair. “Towards collective optomechanics with nanomembranes”. PhD thesis. Department of Physics and Astronomy - Aarhus University, 2017.
- [19] Sepideh Naserbakht and Aurélien Dantan. “Squeeze film pressure sensors based on SiN membrane sandwiches”. In: *Sensors and Actuators A: Physical* 298 (2019), p. 111588. ISSN: 0924-4247. DOI: <https://doi.org/10.1016/j.sna.2019.111588>. URL: <https://www.sciencedirect.com/science/article/pii/S0924424719310787>.
- [20] S. Al-Sumaidae et al. “Pressure sensing with high-finesse monolithic buckled-dome microcavities”. In: *Appl. Opt.* 60.29 (Oct. 2021), pp. 9219–9224. DOI: 10.1364/AO.438942. URL: <https://opg.optica.org/ao/abstract.cfm?URI=ao-60-29-9219>.

- [21] G. J. Hornig et al. “Ultrasound sensing at thermomechanical limits with optomechanical buckled-dome microcavities”. In: *Opt. Express* 30.18 (Aug. 2022), pp. 33083–33096. DOI: 10.1364/OE.463588. URL: <https://opg.optica.org/oe/abstract.cfm?URI=oe-30-18-33083>.
- [22] Mohsen Salimi et al. “Squeeze film absolute pressure sensors with sub-millipascal sensitivity”. In: *Sensors and Actuators A: Physical* 374 (Aug. 2024), p. 115450. ISSN: 0924-4247. DOI: 10.1016/j.sna.2024.115450. URL: <http://dx.doi.org/10.1016/j.sna.2024.115450>.
- [23] Utku Kemiktarak et al. “Mechanically compliant grating reflectors for optomechanics”. In: *Applied Physics Letters* 100.6 (Feb. 2012). ISSN: 1077-3118. DOI: 10.1063/1.3684248. URL: <http://dx.doi.org/10.1063/1.3684248>.
- [24] Utku Kemiktarak et al. “Cavity optomechanics with sub-wavelength grating mirrors”. In: *New Journal of Physics* 14.12 (Dec. 2012), p. 125010. DOI: 10.1088/1367-2630/14/12/125010. URL: <https://dx.doi.org/10.1088/1367-2630/14/12/125010>.
- [25] Catvu H. Bui et al. “High-reflectivity, high-Q micromechanical membranes via guided resonances for enhanced optomechanical coupling”. In: *Applied Physics Letters* 100.2 (Jan. 2012). ISSN: 1077-3118. DOI: 10.1063/1.3658731. URL: <http://dx.doi.org/10.1063/1.3658731>.
- [26] R. A. Norte, J. P. Moura, and S. Gröblacher. “Mechanical Resonators for Quantum Optomechanics Experiments at Room Temperature”. In: *Phys. Rev. Lett.* 116 (14 Apr. 2016), p. 147202. DOI: 10.1103/PhysRevLett.116.147202. URL: <https://link.aps.org/doi/10.1103/PhysRevLett.116.147202>.
- [27] Christoph Reinhardt et al. “Ultralow-Noise SiN Trampoline Resonators for Sensing and Optomechanics”. In: *Physical Review X* 6.2 (Apr. 2016). ISSN: 2160-3308. DOI: 10.1103/physrevx.6.021001. URL: <http://dx.doi.org/10.1103/PhysRevX.6.021001>.
- [28] Xu Chen et al. “High-finesse Fabry–Perot cavities with bidimensional Si<sub>3</sub>N<sub>4</sub> photonic-crystal slabs”. In: *Light: Science & Applications* 6.1 (2017), e16190–e16190.
- [29] Feng Zhou et al. *Cavity optomechanical bistability with an ultrahigh reflectivity photonic crystal membrane*. 2022. arXiv: 2211.10485 [physics.optics]. URL: <https://arxiv.org/abs/2211.10485>.

- [30] Jipeng Xu et al. “Millimeter-scale ultrathin suspended metasurface integrated high-finesse optomechanical cavity”. In: *Optics Letters* 47 (Oct. 2022), pp. 5481–5484. DOI: 10.1364/OL.465567.
- [31] You Sang et al. “Spatial Nonreciprocal Transmission and Optical Bistability Based on Millimeter-Scale Suspended Metasurface”. In: *Advanced Optical Materials* 10 (Sept. 2022), p. 2201523. DOI: 10.1002/adom.202201523.
- [32] Georg Enzian et al. “Phononically shielded photonic-crystal mirror membranes for cavity quantum optomechanics”. In: *Optics Express* 31.8 (Apr. 2023), p. 13040. ISSN: 1094-4087. DOI: 10.1364/oe.484369. URL: <http://dx.doi.org/10.1364/OE.484369>.
- [33] Shanhui Fan and J. D. Joannopoulos. “Analysis of guided resonances in photonic crystal slabs”. In: *Physical Review B* 65 (2002).
- [34] Shanhui Fan, Wonjoo suh, and J. D. Joannopoulos. “Temporal coupled-mode theory for the Fano resonance in optical resonators”. In: *Optical Society of America* 20.3 (2003).
- [35] T. Mitra et al. “Narrow-linewidth Fano microcavities with resonant subwavelength grating mirror”. In: *Optics Express* 32.9 (2024).
- [36] Sushanth Kini Manjeshwar et al. “Integrated microcavity optomechanics with a suspended photonic crystal mirror above a distributed Bragg reflector”. In: *Opt. Express* 31.19 (Sept. 2023), pp. 30212–30226. DOI: 10.1364/OE.496447. URL: <https://opg.optica.org/oe/abstract.cfm?URI=oe-31-19-30212>.
- [37] Marc Eichhorn. *Laser Physics - From Principles to Practical Work in the Lab*. Springer International Publishing Switzerland, 2014.
- [38] Frank L. Pedrotti, Leno M. Pedrotti, and Leno S. Pedrotti. *Introduction to Optics, 3rd edition*. Cambridge University Press, 2018.
- [39] U. Fano. “Effects of Configuration Interaction on Intensities and Phase Shifts\*”. In: *Physical Review* 124.6 (1961).
- [40] Dmitry A. Bykov and Leonid L. Doskolovich. “Spatiotemporal coupled-mode theory of guided-mode resonant gratings”. In: *Optical Society of America* 14.3 (2015).
- [41] A. A. Darki et al. “Profilometry and stress analysis of suspended nanosstructured thin films”. In: *Journal of Applied Physics* (2021).

- [42] A. Parthenopoulos et al. “Optical spatial differentiation with suspended subwavelength gratings”. In: *Optics Express* 29.5 (2021).
- [43] E. Popov, L. Mashev, and D. Maystre. “Theoretical Study of the Anomalies of Coated Dielectric Gratings”. In: *Optica Acta: International Journal of Optics* 33.5 (1986).
- [44] URL: <https://pages.nist.gov/ScatterMIST/docs/index.htm>.
- [45] C. Toft-Vandborg et al. “Collimation and finite-size effects in suspended resonant guided-mode gratings”. In: *Journal of the Optical Society of America* 38.11 (2021).
- [46] Ali Akbar Darki. “Nanostructured trampolines for photonics and sensing”. PhD thesis. Department of Physics and Astronomy - Aarhus University, 2022.
- [47] A. Naesby and A. Dantan. “Microcavities with suspended subwavelength structured mirrors”. In: *Optics Express* 26.23 (2018).
- [48] URL: <https://www.toptica.com/products/tunable-diode-lasers/ecdl-dfb-lasers/dl-pro>.
- [49] URL: <https://www.thorlabs.com/thorproduct.cfm?partnumber=P3-780PM-FC-10>.
- [50] URL: <https://www.edmundoptics.com/knowledge-center/application-notes/optics/understanding-waveplates/>.
- [51] URL: <https://www.thorlabs.com/thorproduct.cfm?partnumber=PT1#ad-image>.
- [52] URL: [https://www.thorlabs.com/newgroupage9.cfm?objectgroup\\_id=11015](https://www.thorlabs.com/newgroupage9.cfm?objectgroup_id=11015).
- [53] URL: <http://www.noliac.com/card/show/nac2123/>.
- [54] URL: <https://www.thorlabs.com/thorproduct.cfm?partnumber=NFL5DP20/M>.
- [55] URL: <https://www.keysight.com/us/en/product/DSOX2024A/oscilloscope-200-mhz-4-analog-channels.html>.
- [56] URL: <https://www.keysight.com/us/en/assets/7018-05928/data-sheets/5992-2572.pdf>.
- [57] URL: [https://www.thorlabs.com/newgroupage9.cfm?objectgroup\\_id=3341](https://www.thorlabs.com/newgroupage9.cfm?objectgroup_id=3341).

- [58] S. Yu. Sadov and K. A. McGreer. “Polarization dependence of diffraction gratings that have total internal reflection facets”. In: *J. Opt. Soc. Am. A* 17.9 (2000).
- [59] M. Forster et al. “213 nm and 532 nm solid state laser treatment of biogenetical fibrous materials”. In: (2010).
- [60] Ifan G. Hughes and Thomas P.A. Hase. *Measurements and their Uncertainties - A Practical Guide to Modern Error Analysis*. Oxford University Press, 2010.
- [61] B. Nair, A. Naesby, and A. Dantan. “Optomechanical characterization of silicon nitride membrane arrays”. In: *Optics Letter* 42.7 (2017).
- [62] Chia Wei Hsu et al. “Bound states in the continuum”. In: *Nature Reviews Materials* 1.9 (2016), p. 16048.
- [63] Yi Yu et al. “Ultra-coherent Fano laser based on a bound state in the continuum”. In: *Nature Photonics* 15.10 (2021), pp. 758–764.

# Appendix

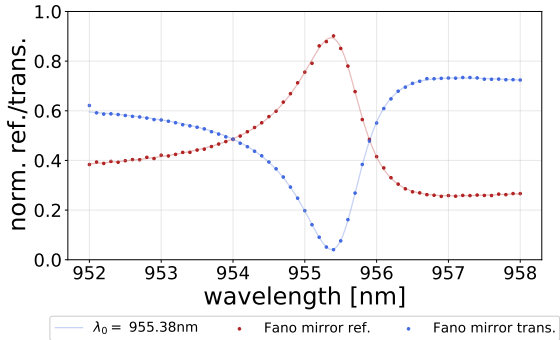
## A GitHub

During this project I have stored all my data and produced code in a public GitHub repository. The repository is named "optomechanics" after the group at the Department of Physics and Astronomi at Aarhus University in which I have made this Master's project.

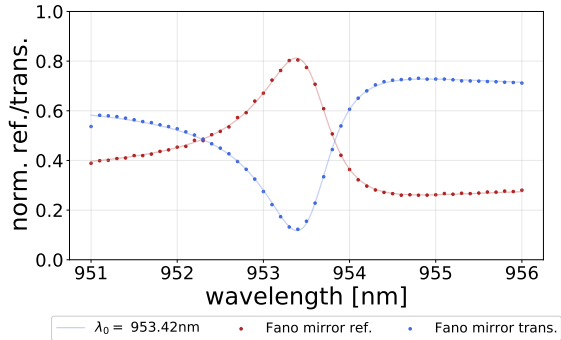
Links/terminal commands to clone repository:

- HTTPS: <https://github.com/Mikkelodeonn/optomechanics.git>
- SSH: `git@github.com:Mikkelodeonn/optomechanics.git`
- GitHub CLI: `gh repo clone Mikkelodeonn/optomechanics`

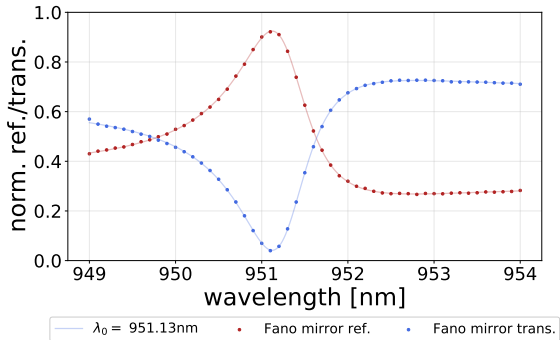
## B Additional Fano mirror spectra



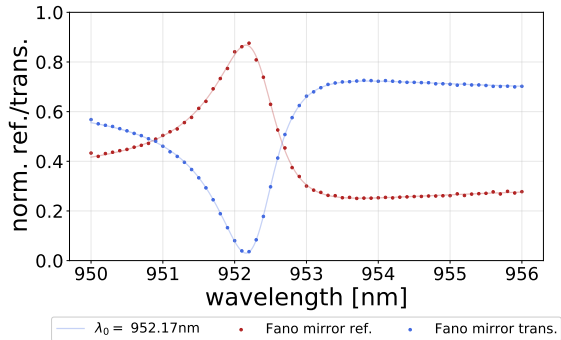
(a)



(b)



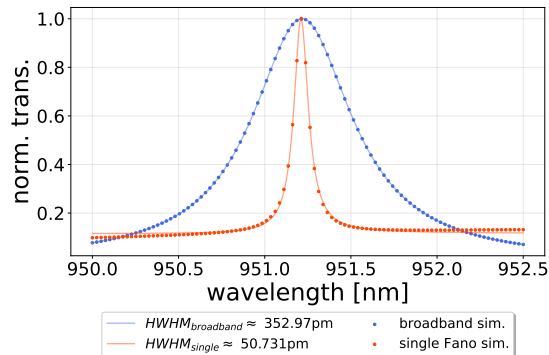
(c)



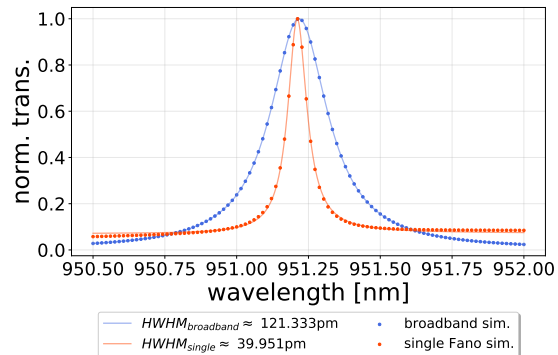
(d)

## C Simulated broadband and single Fano cavity resonance transmission spectra

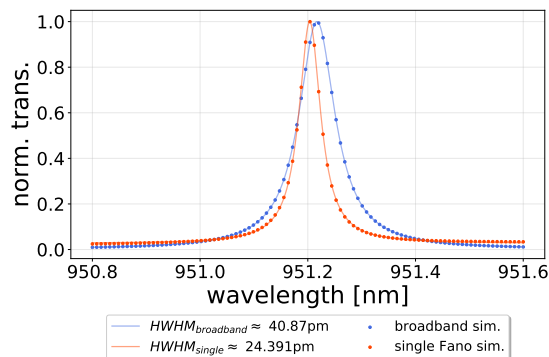
(Figure 12a in section 2.3.2)



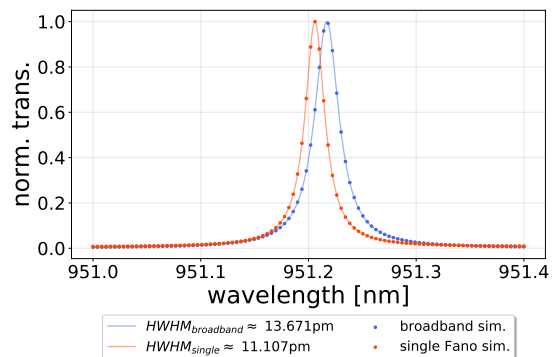
(a)



(b)



(c)



(d)

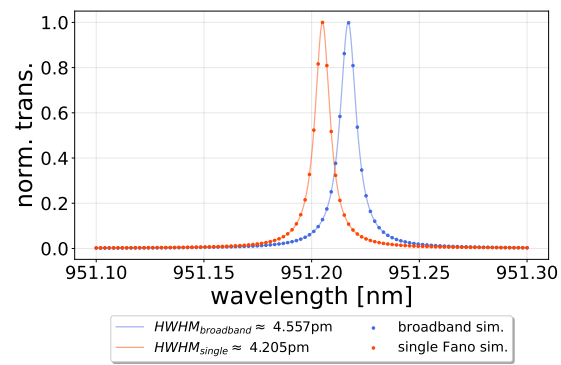


Figure 77

## D Simulated single and double Fano cavity resonance transmission spectra

(Figure 16a in section 2.4.3)

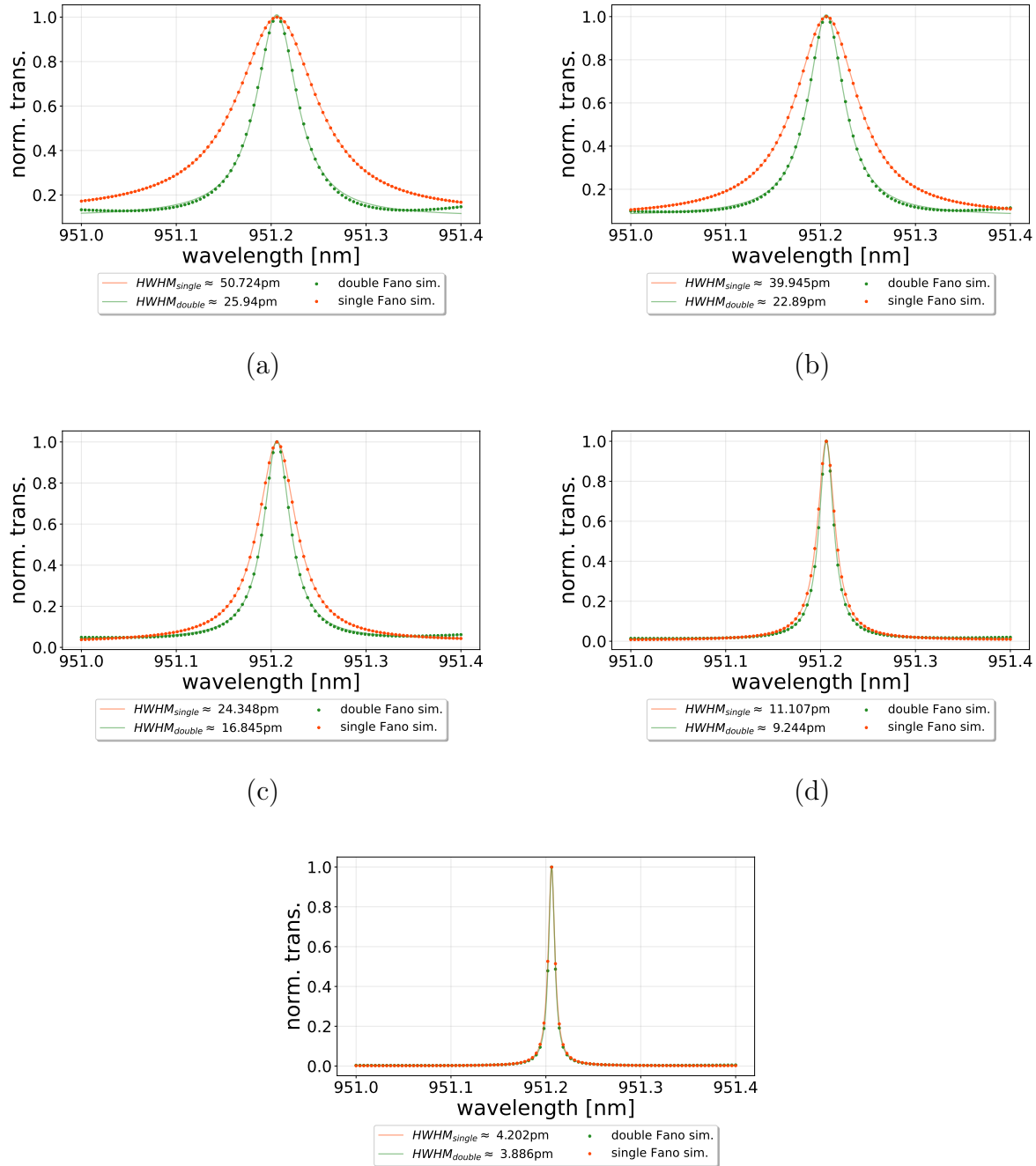
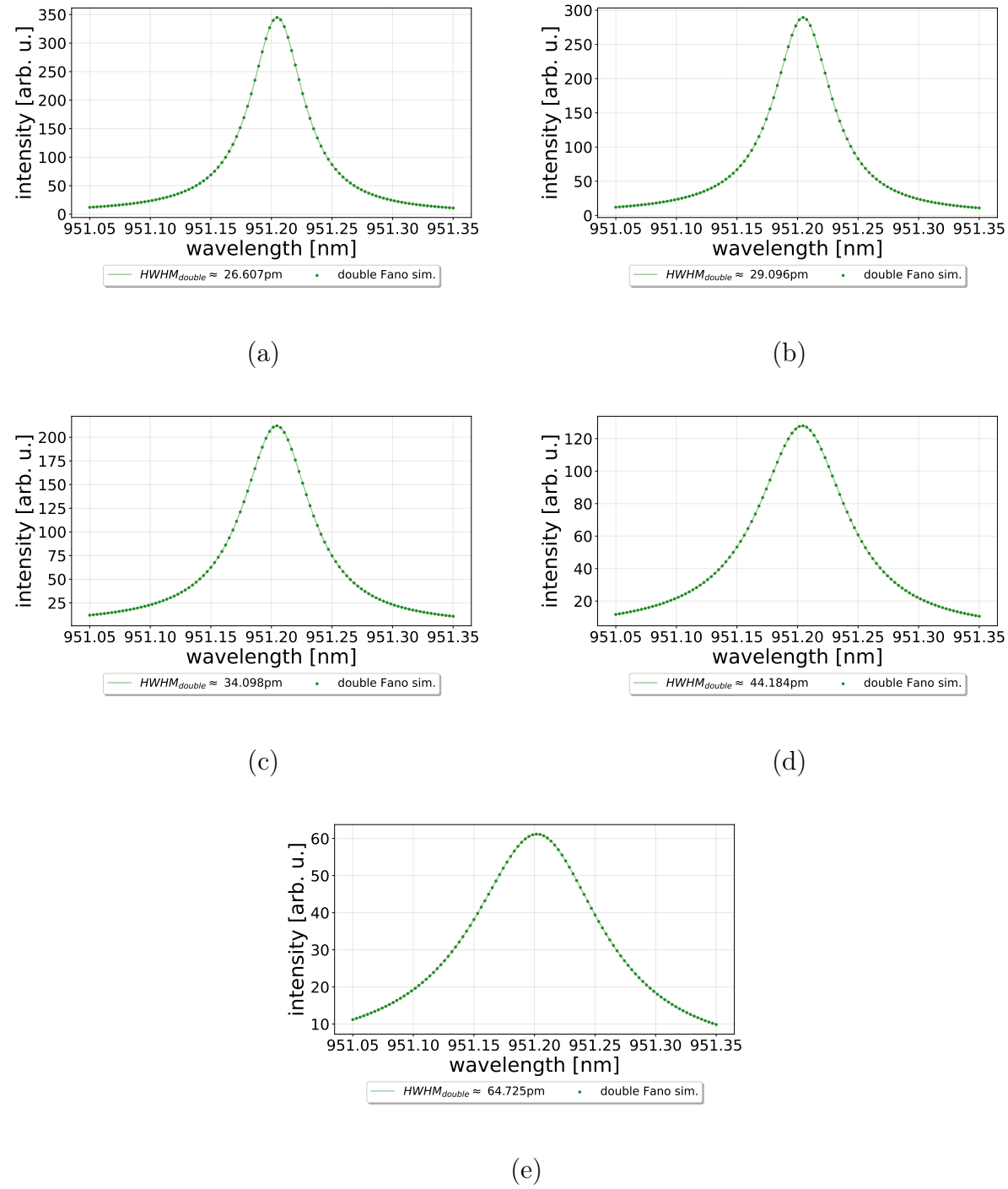


Figure 78

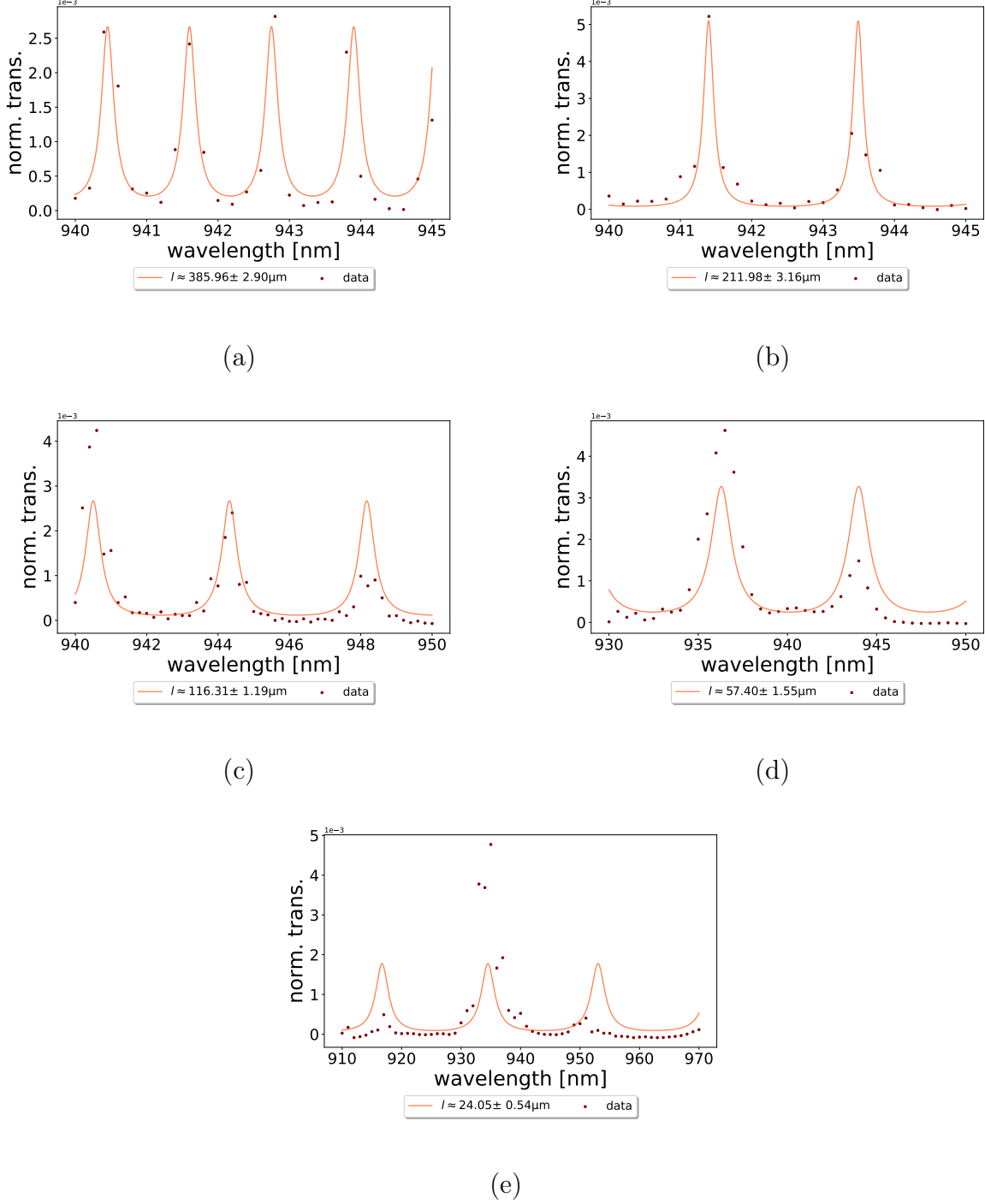
## E Simulated double Fano cavity resonance transmission spectra for different values of the resonant loss term

(Figure 18 in section 2.4.4)

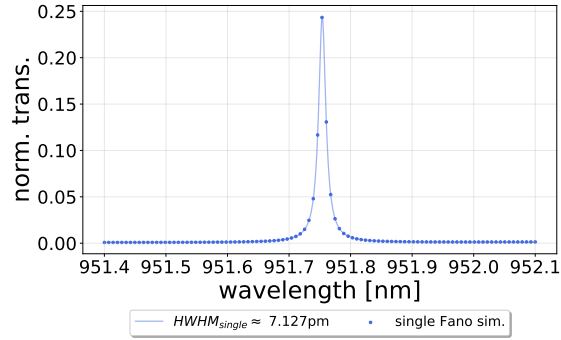


## F Measured single Fano transmission data (Figure 59 in section 4.2)

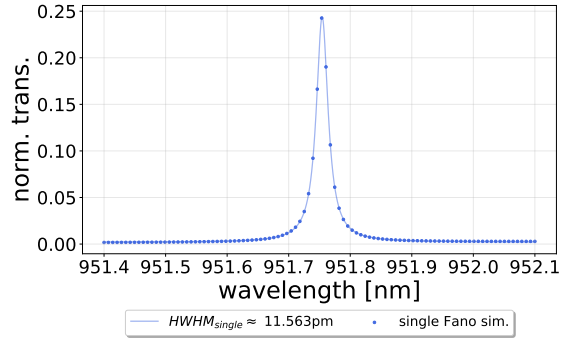
### Off-resonance spectra (determining the cavity length)



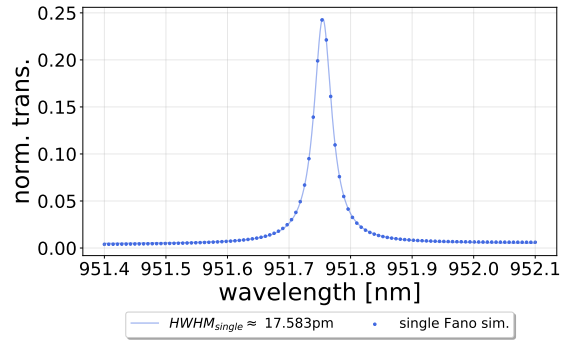
## Simulated spectra



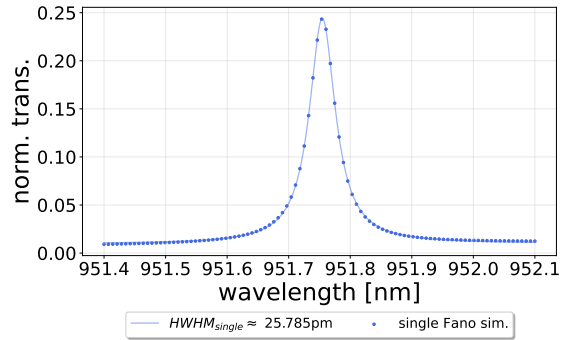
(a)



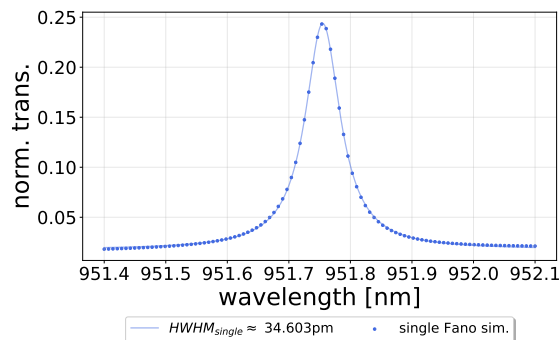
(b)



(c)

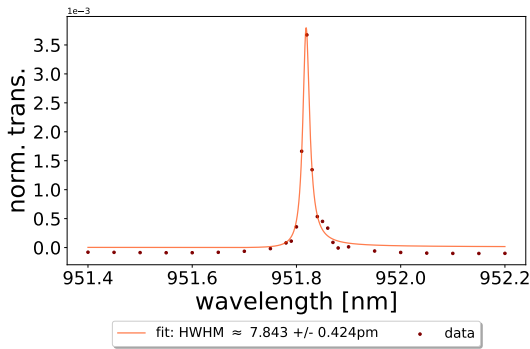


(d)

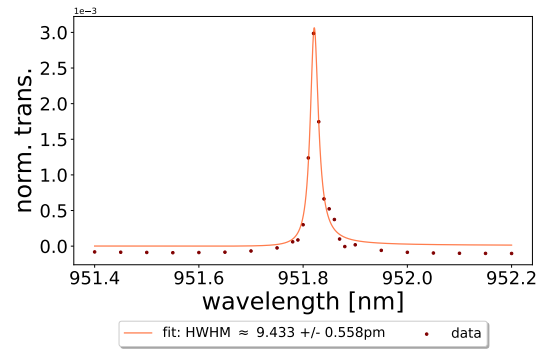


(e)

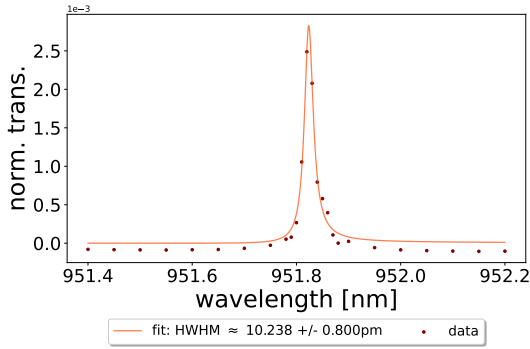
cavity length:  $l \approx 386\mu m$



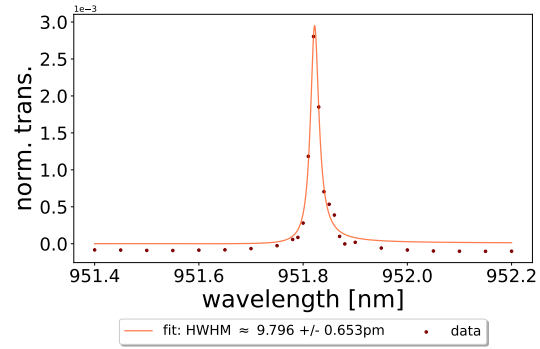
(a)



(b)

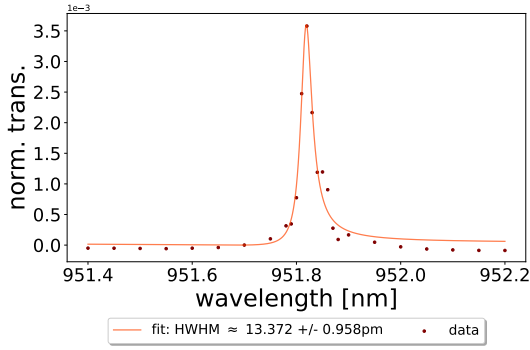


(c)

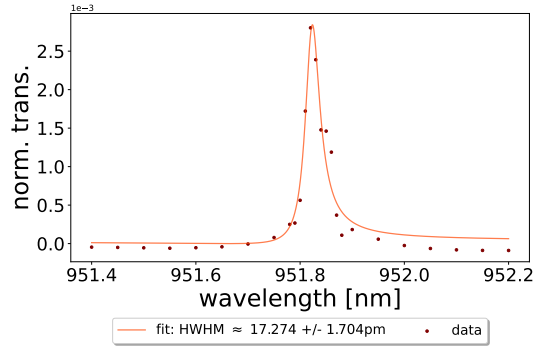


(d)

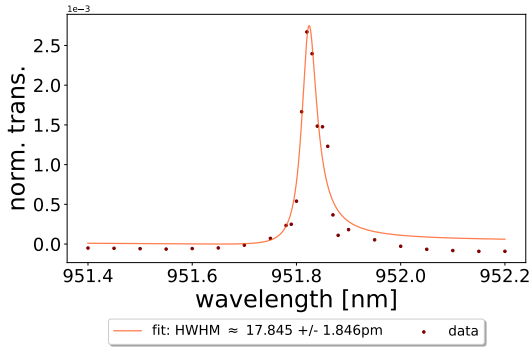
cavity length:  $l \approx 212\mu m$



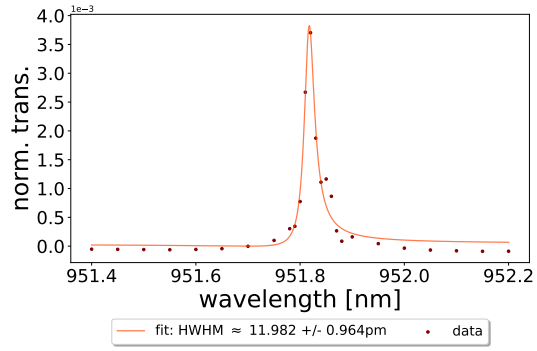
(a)



(b)

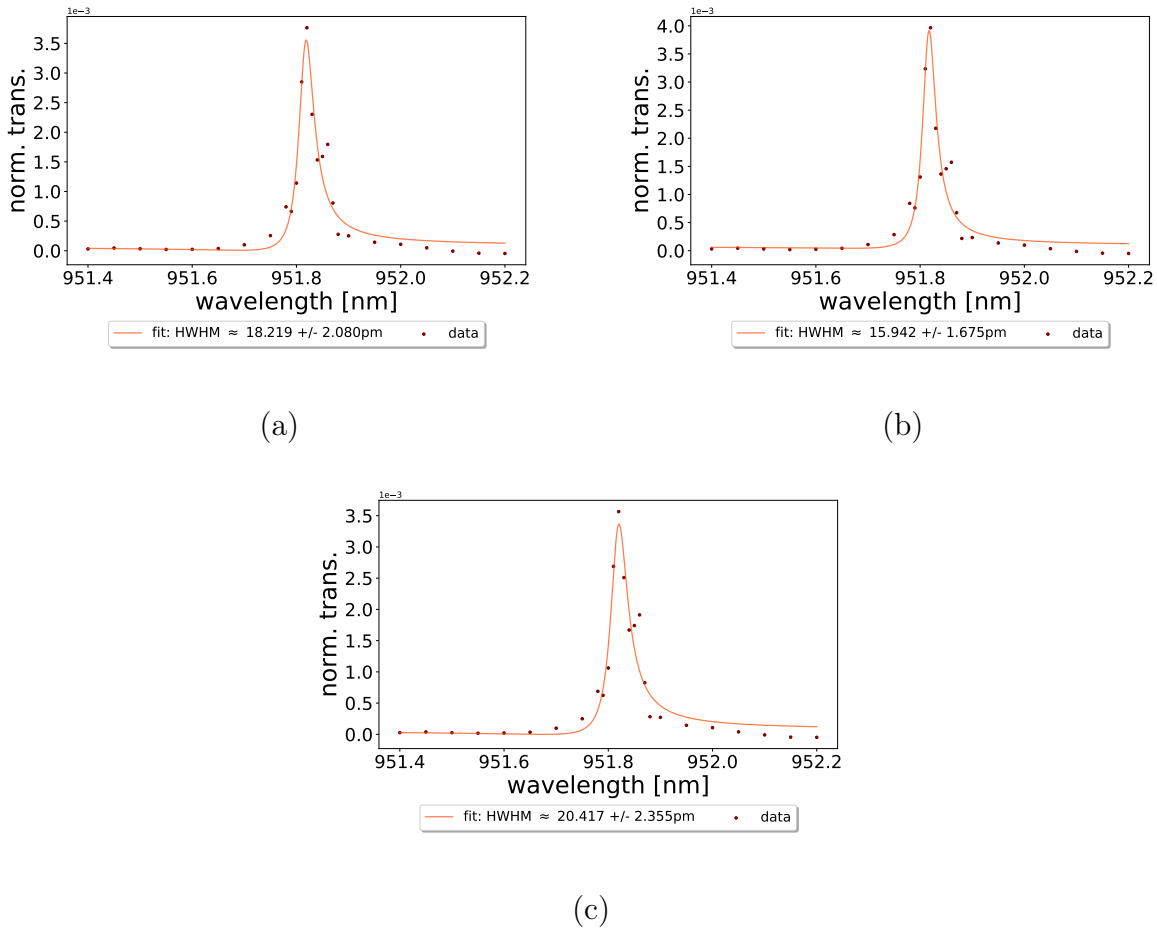


(c)

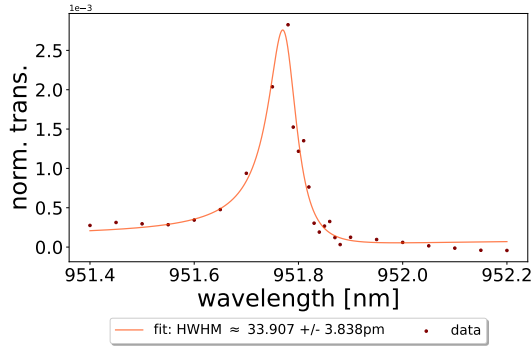


(d)

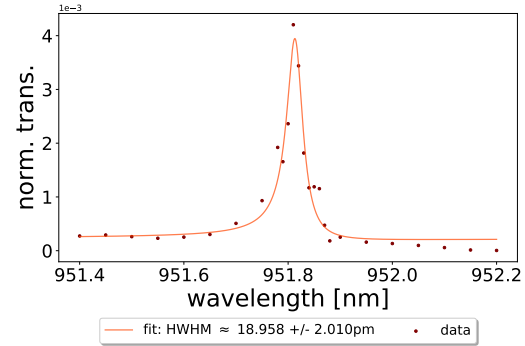
cavity length:  $l \approx 116\mu m$



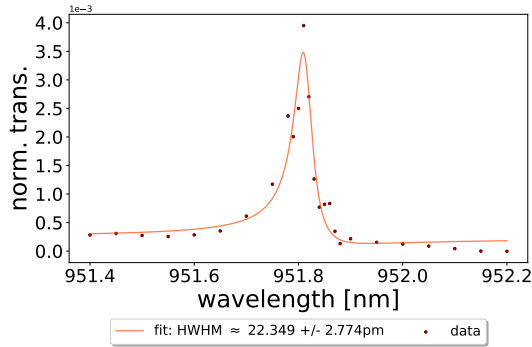
cavity length:  $l \approx 57\mu m$



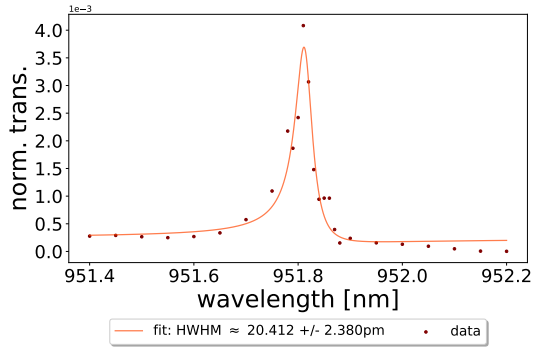
(a)



(b)

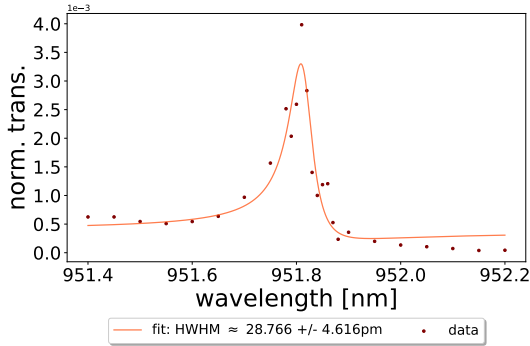


(c)

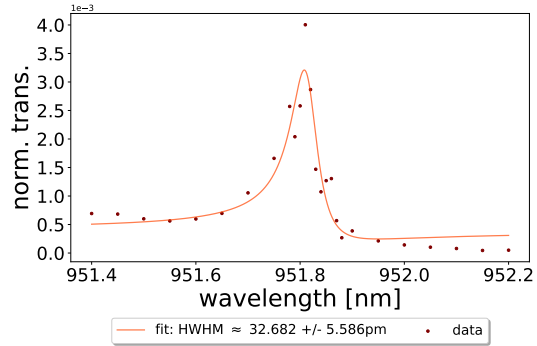


(d)

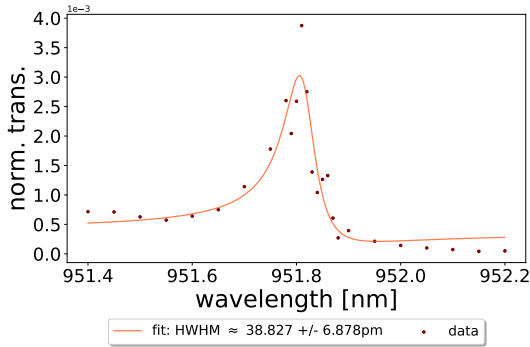
cavity length:  $l \approx 24\mu m$



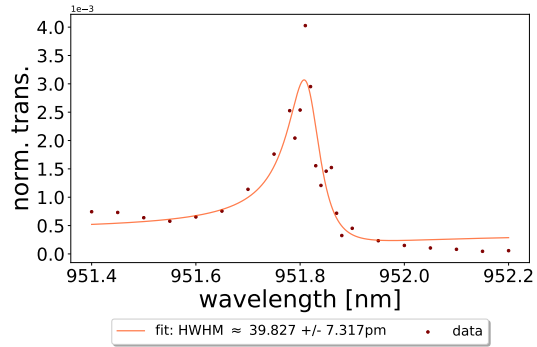
(a)



(b)



(c)

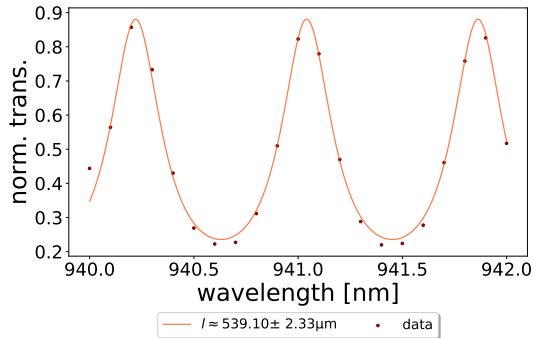
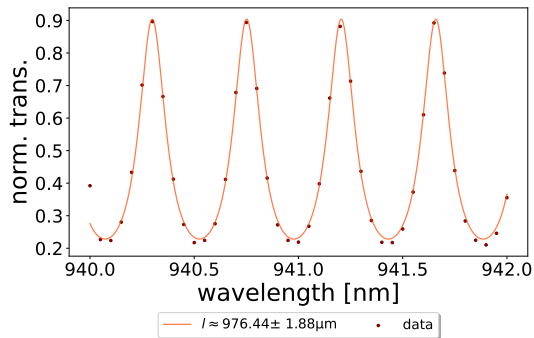


(d)

## G Measured double Fano transmission data

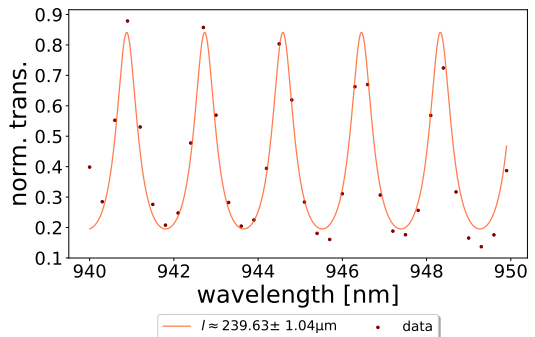
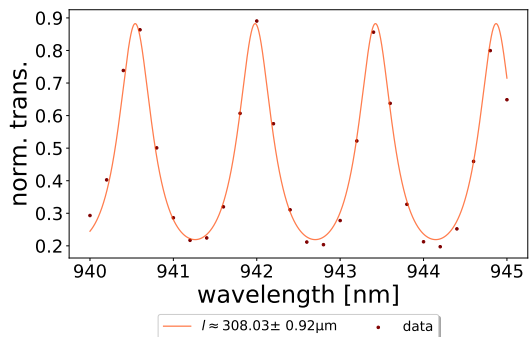
(Figure 69 in section 4.3)

Off-resonance spectra (determining the cavity length)



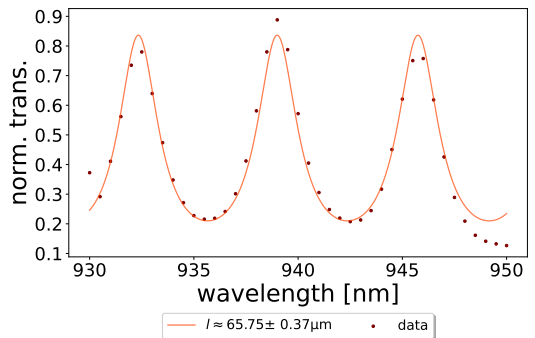
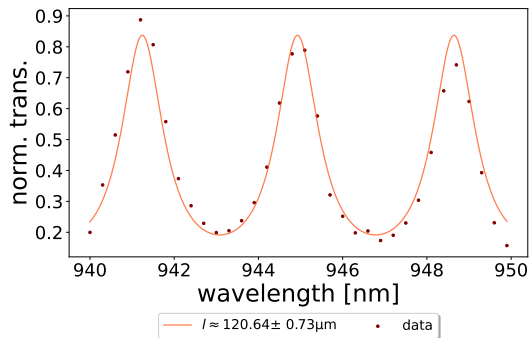
(a)

(b)



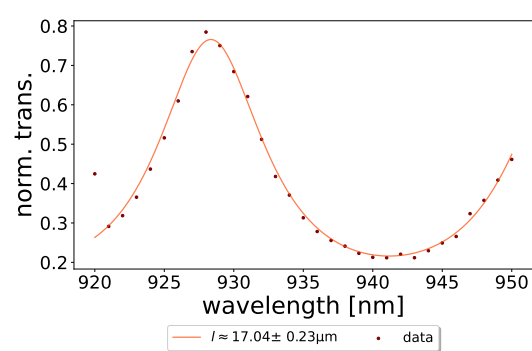
(c)

(d)



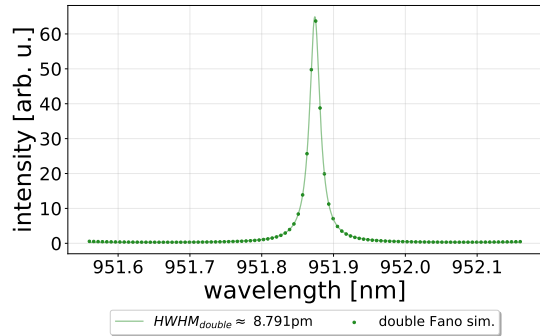
(e)

(f)

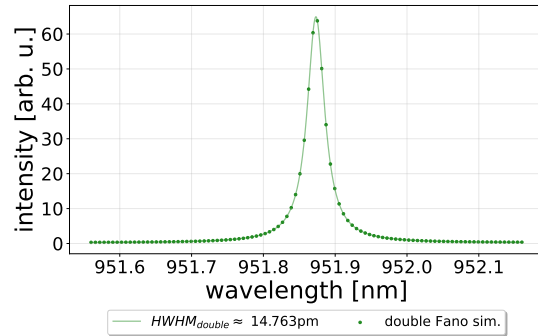


(g)

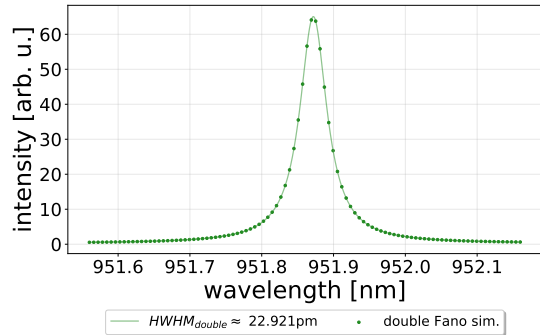
## Simulated spectra



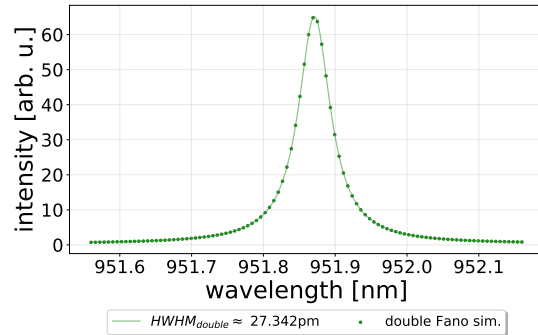
(a)



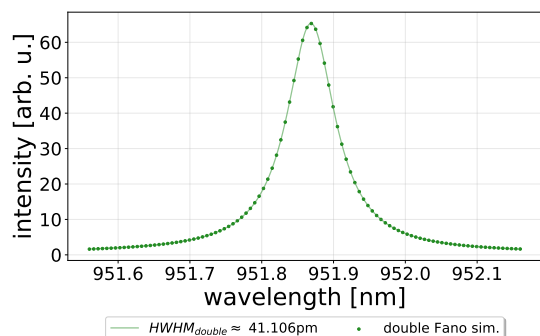
(b)



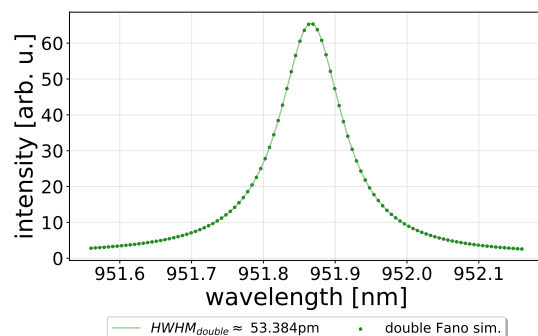
(c)



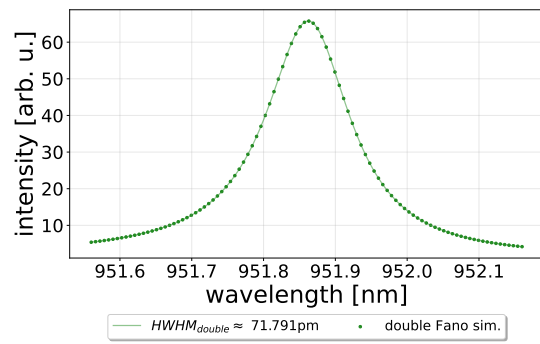
(d)



(e)

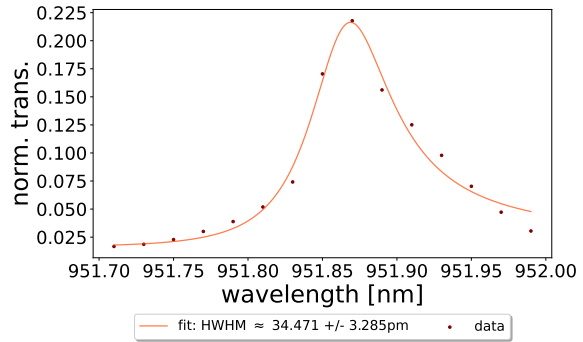


(f)

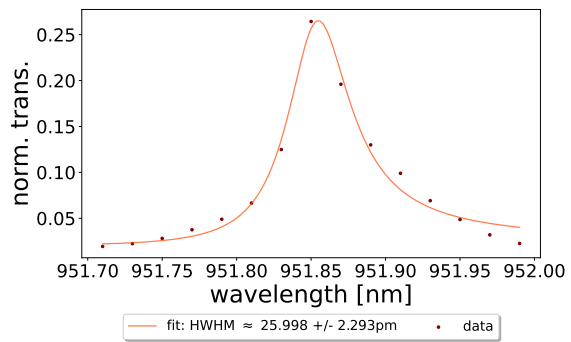


(g)

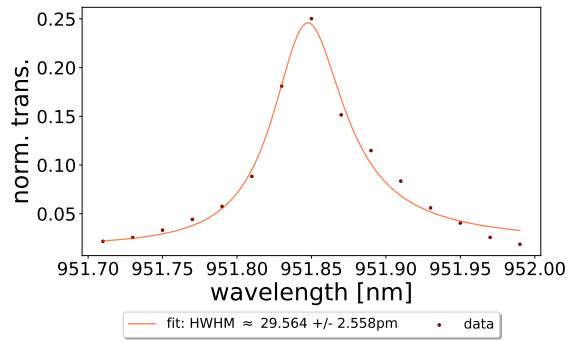
cavity length:  $l \approx 976\mu m$



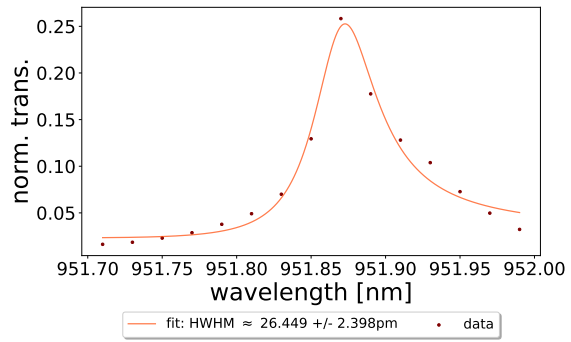
(a)



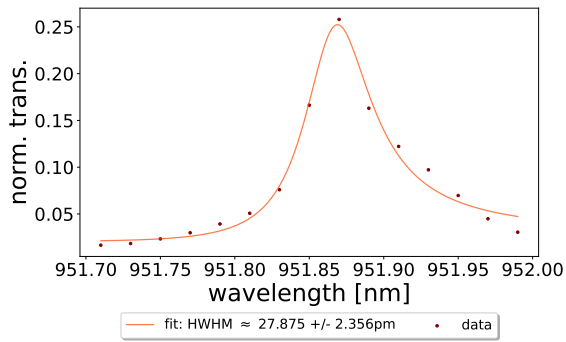
(b)



(c)

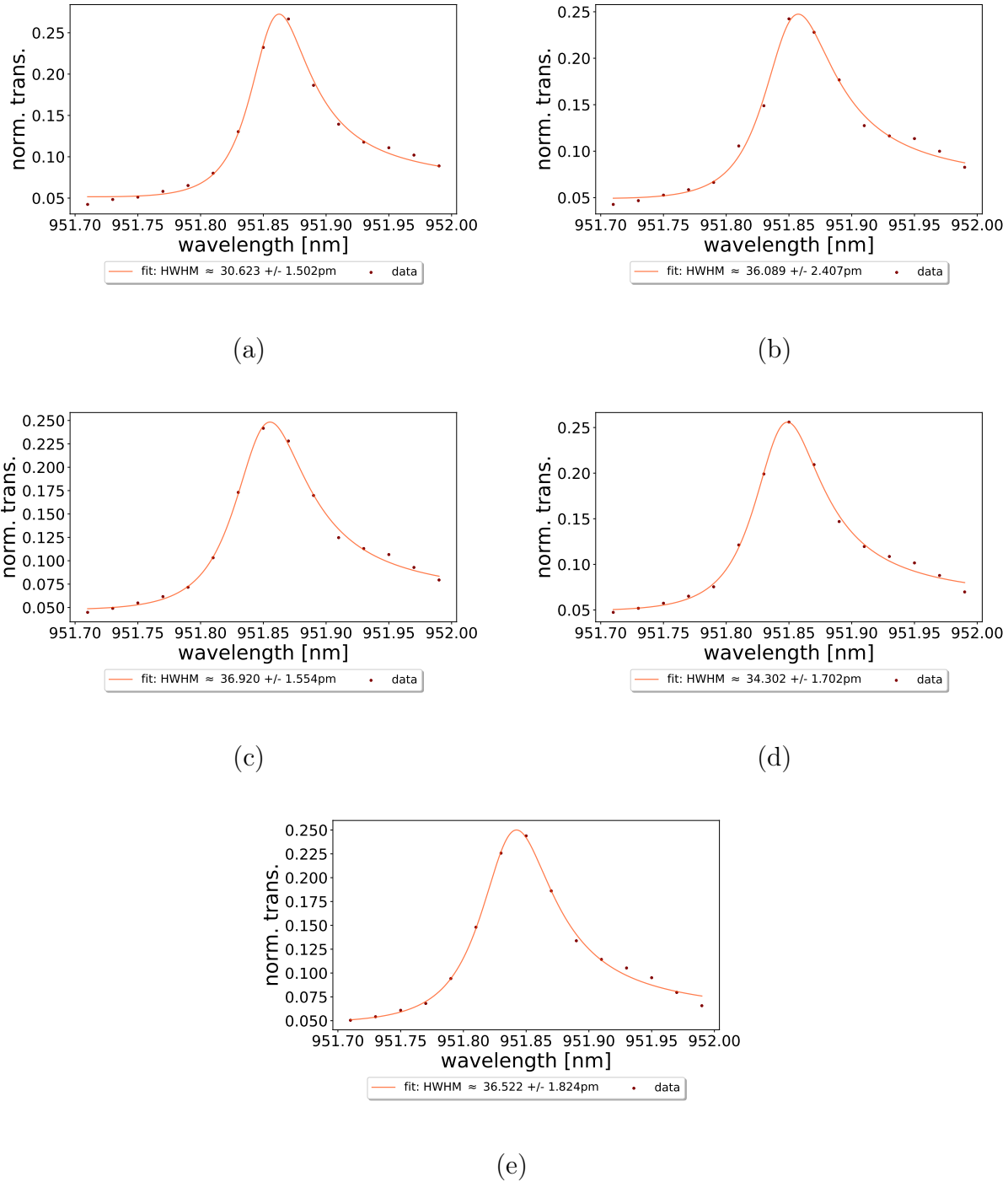


(d)

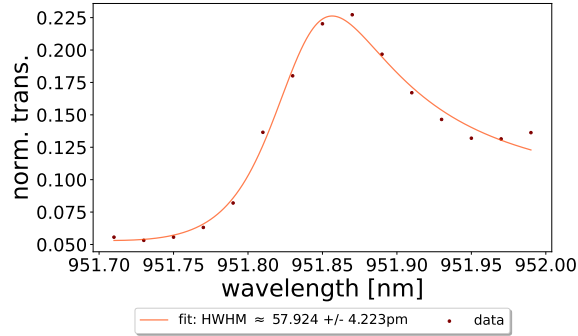


(e)

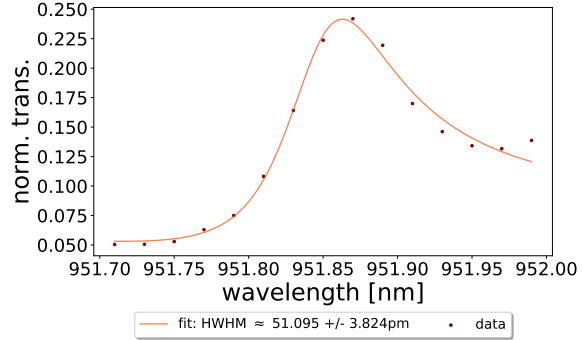
cavity length:  $l \approx 539\mu m$



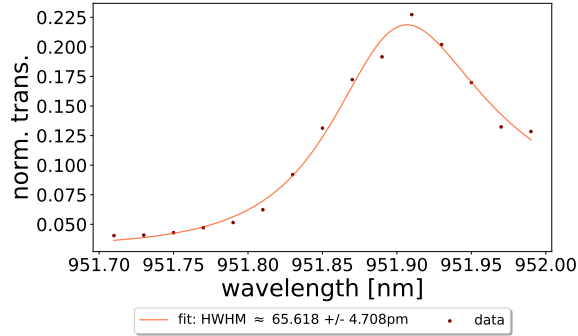
cavity length:  $l \approx 308\mu m$



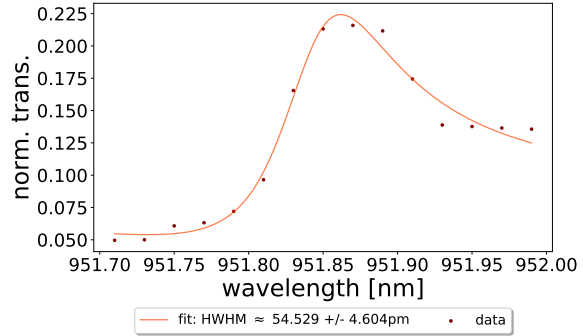
(a)



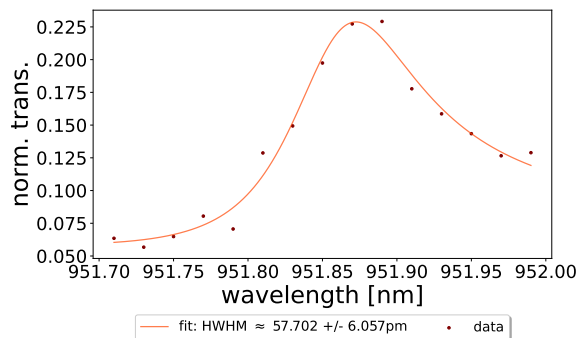
(b)



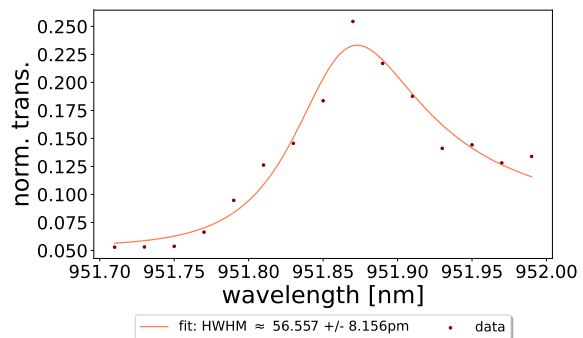
(c)



(d)

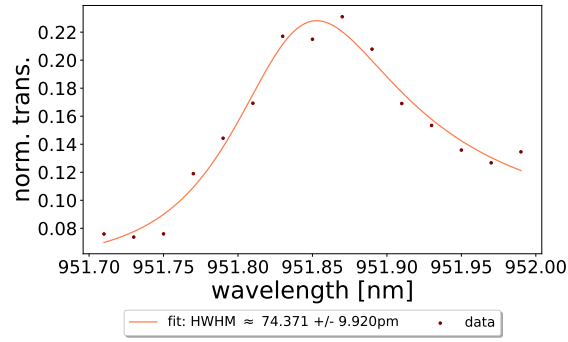


(e)

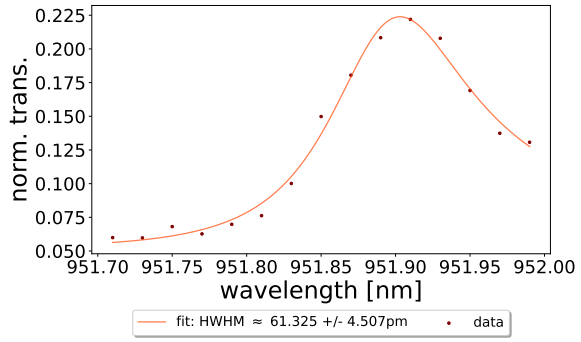


(f)

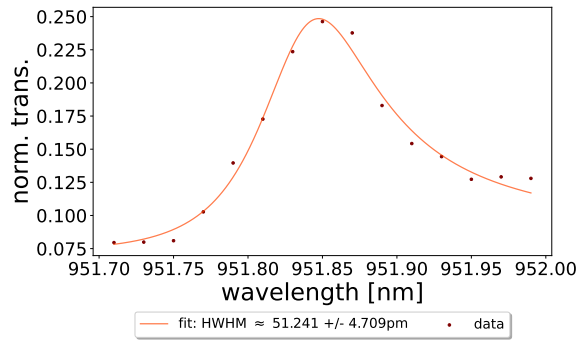
cavity length:  $l \approx 239\mu m$



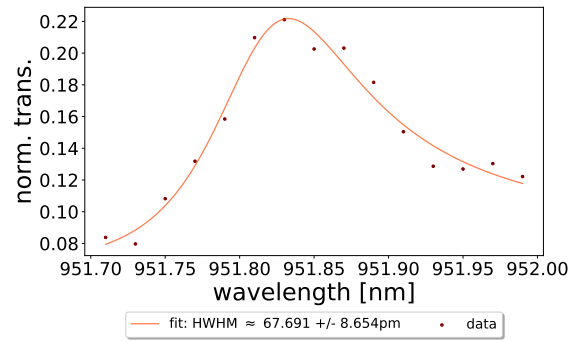
(a)



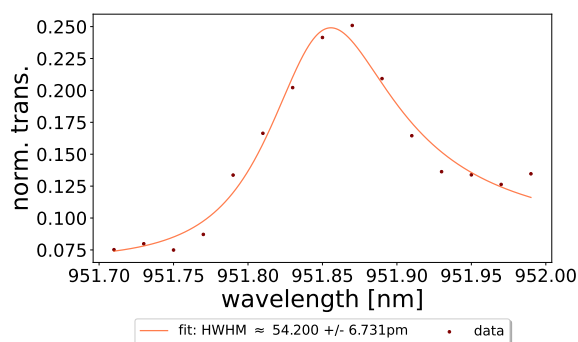
(b)



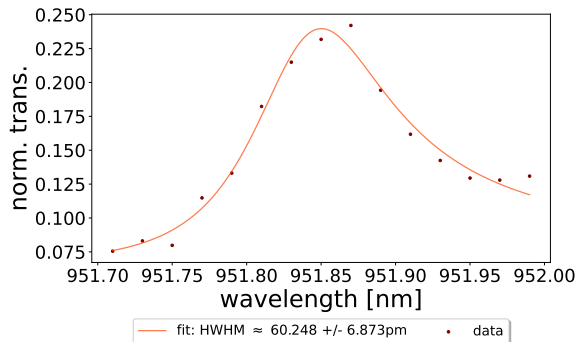
(c)



(d)

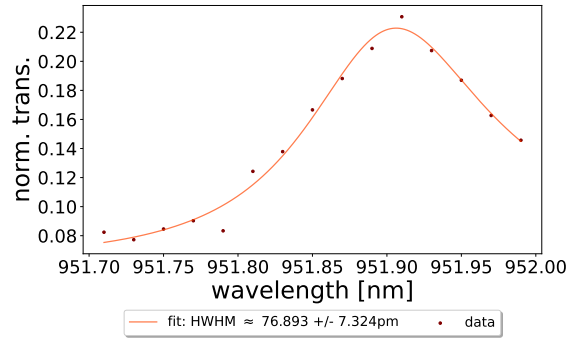


(e)

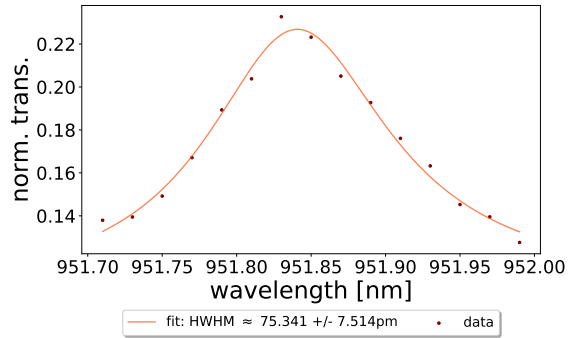


(f)

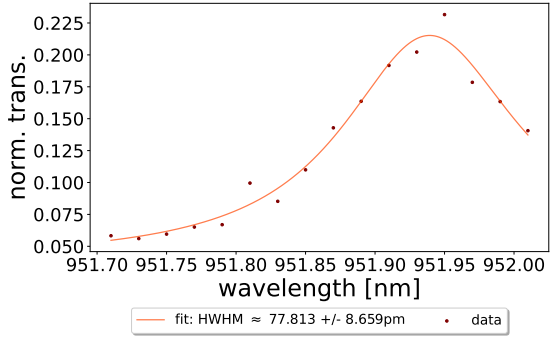
cavity length:  $l \approx 121\mu m$



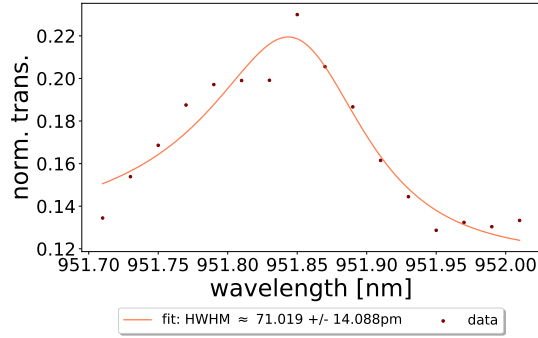
(a)



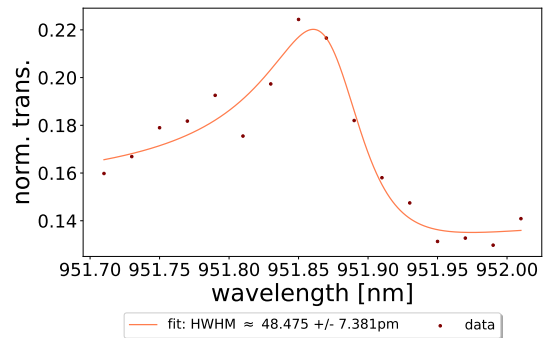
(b)



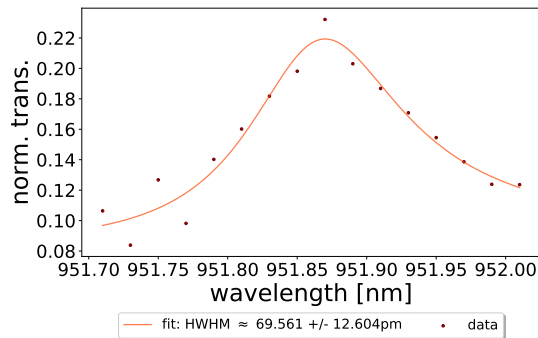
(c)



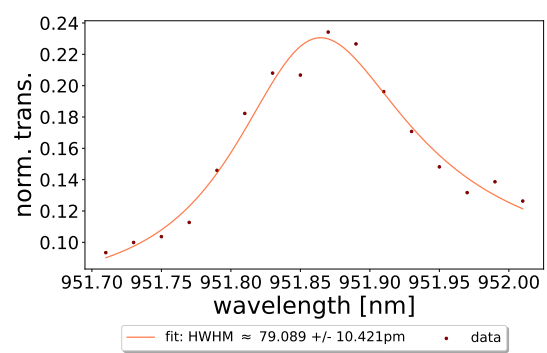
(d)



(e)

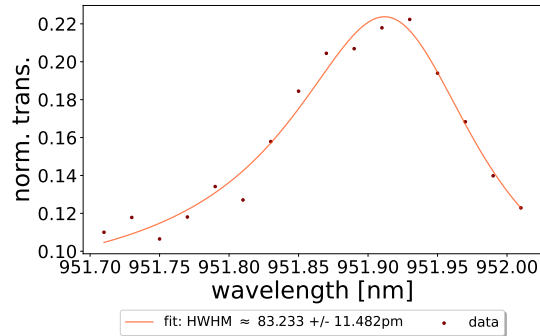


(f)

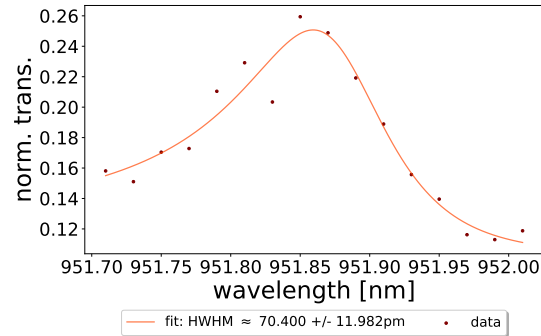


(g)

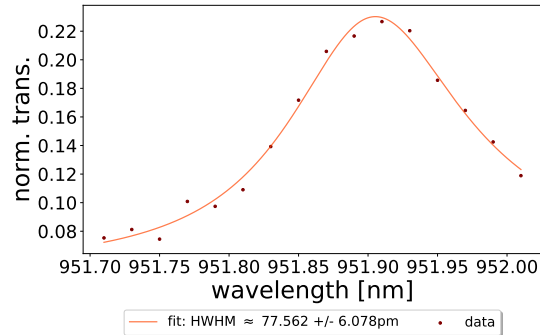
cavity length:  $l \approx 66\mu m$



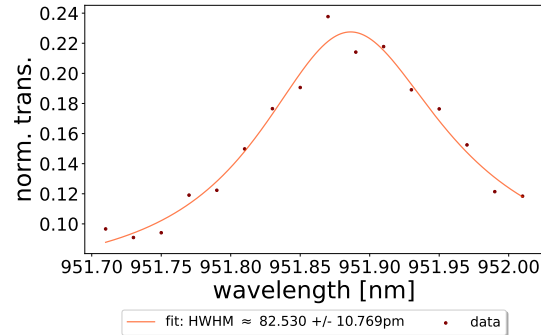
(a)



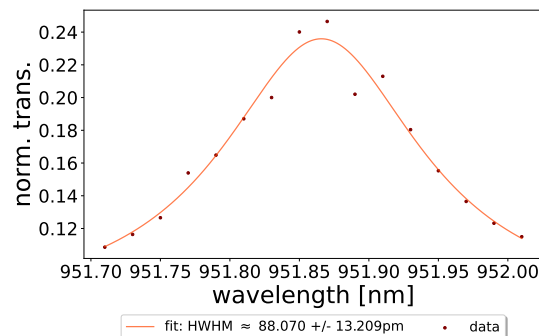
(b)



(c)

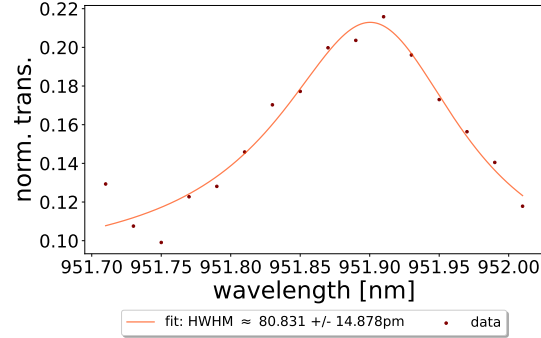
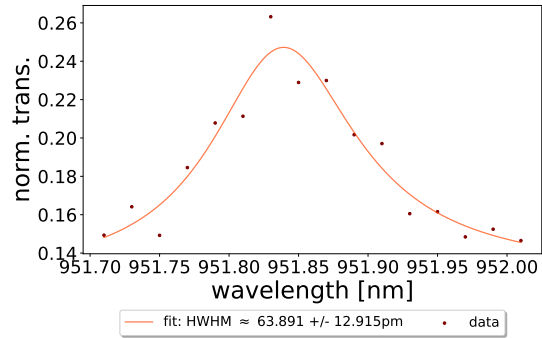


(d)



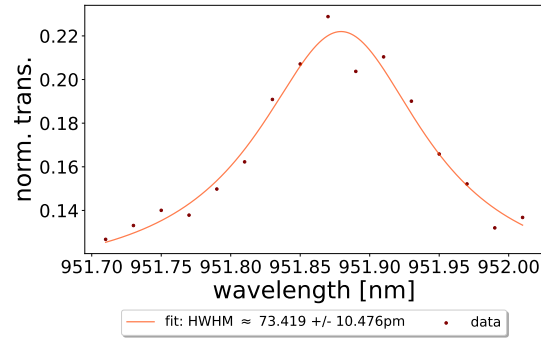
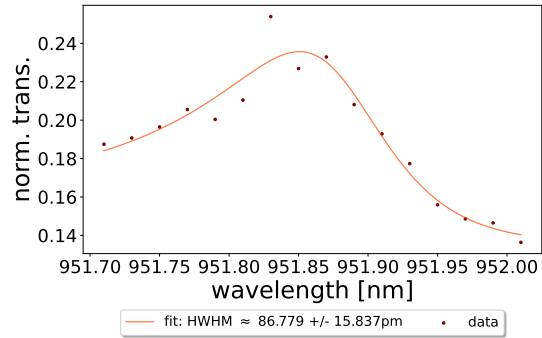
(e)

cavity length:  $l \approx 17\mu m$



(a)

(b)

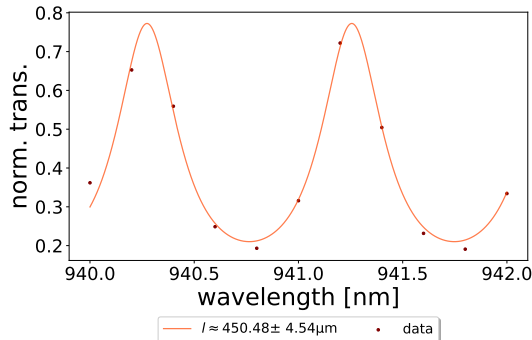


(c)

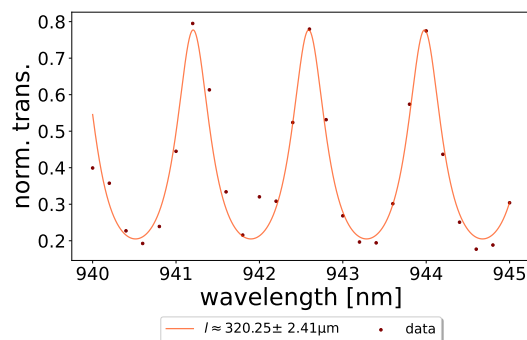
(d)

(Figure 72 in section 4.4)

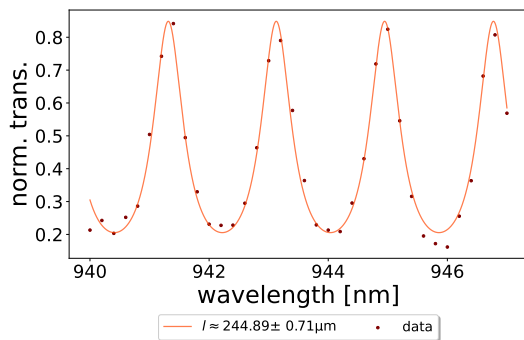
### Off-resonance spectra (determining the cavity length)



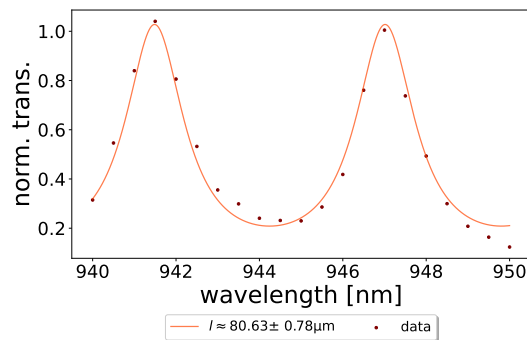
(a)



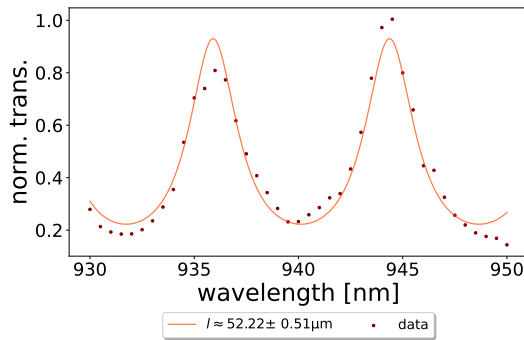
(b)



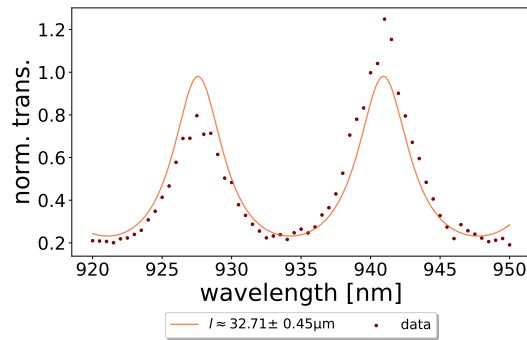
(c)



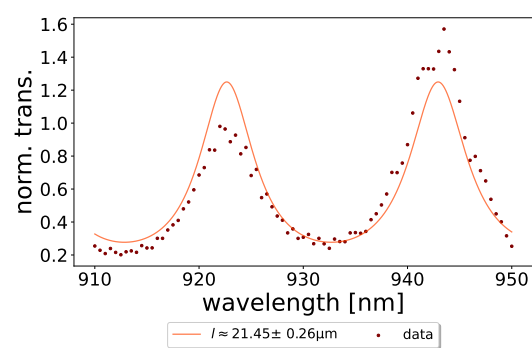
(d)



(e)

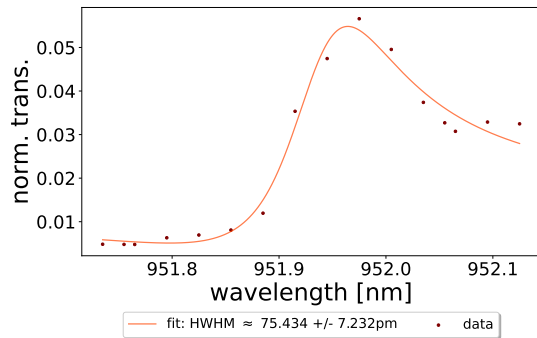
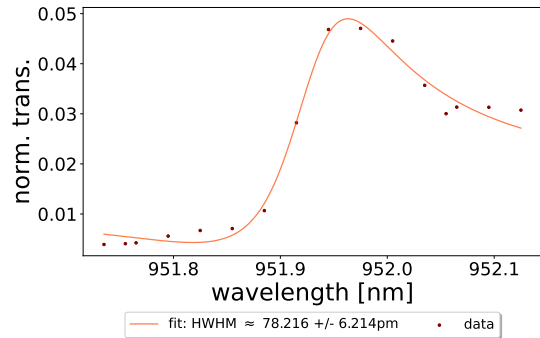


(f)



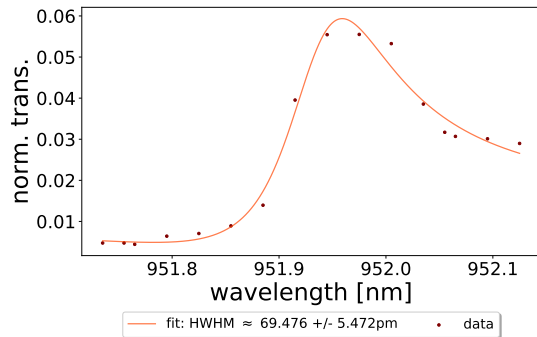
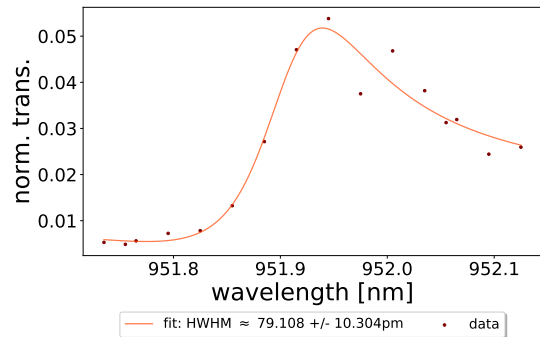
(g)

cavity length:  $l \approx 450\mu m$



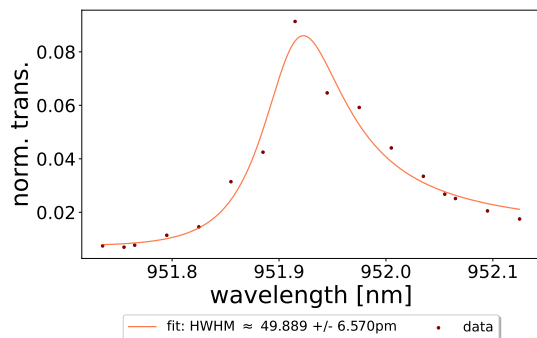
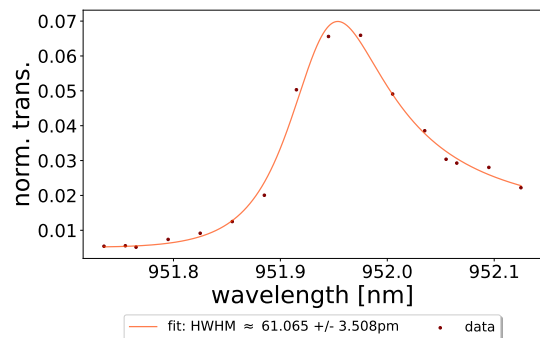
(a)

(b)



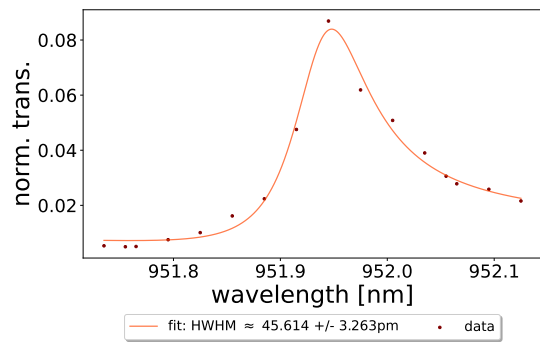
(c)

(d)

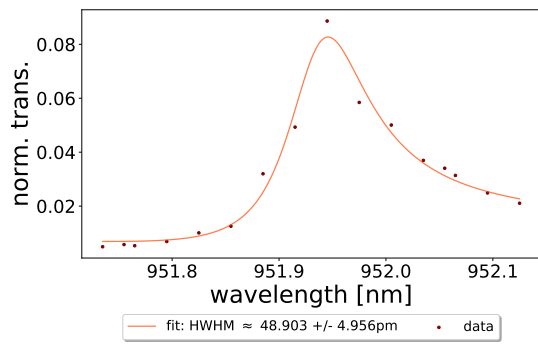


(e)

(f)

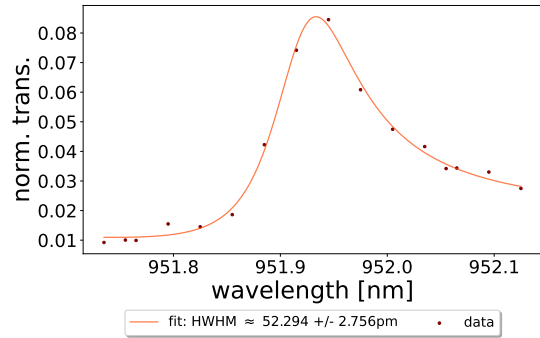


(g)

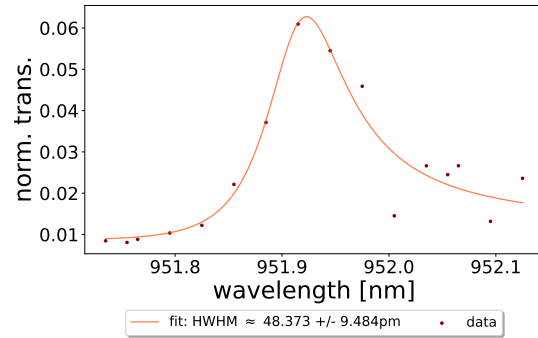


(h)

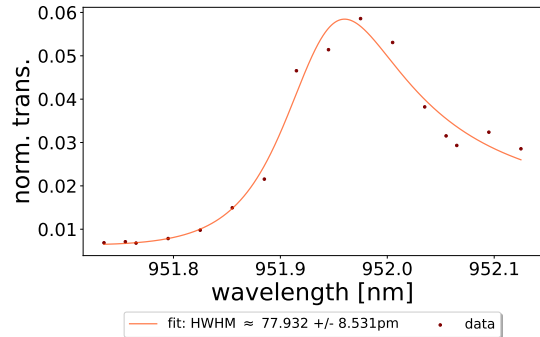
cavity length:  $l \approx 320\mu m$



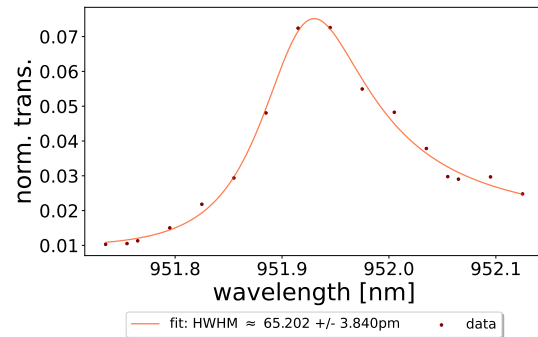
(a)



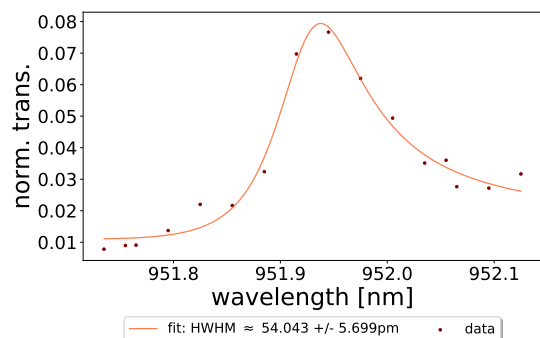
(b)



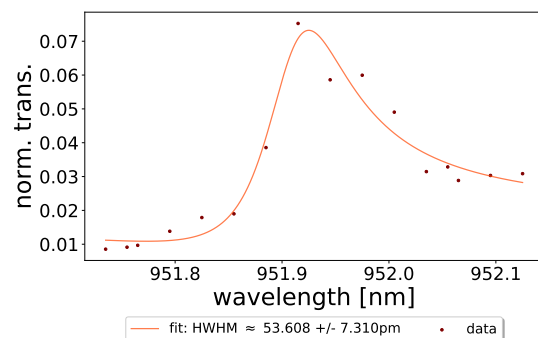
(c)



(d)

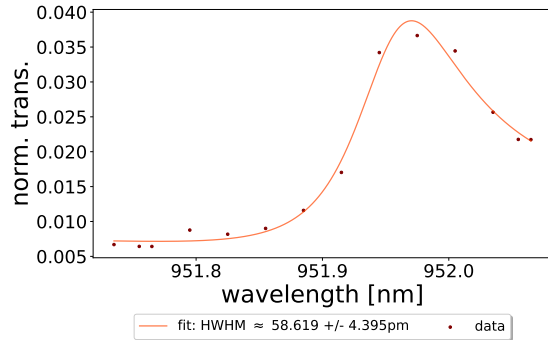


(e)

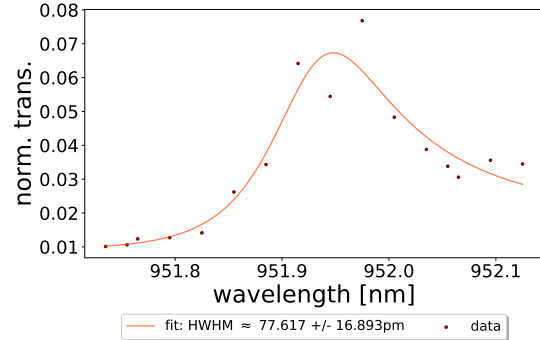


(f)

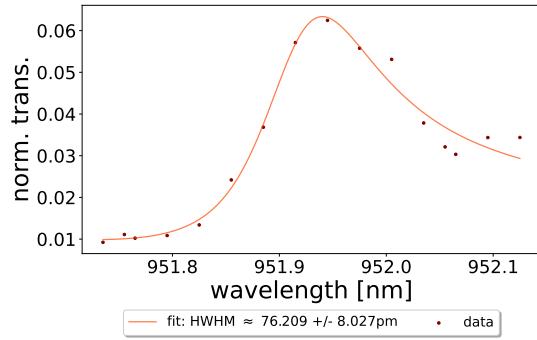
cavity length:  $l \approx 245\mu m$



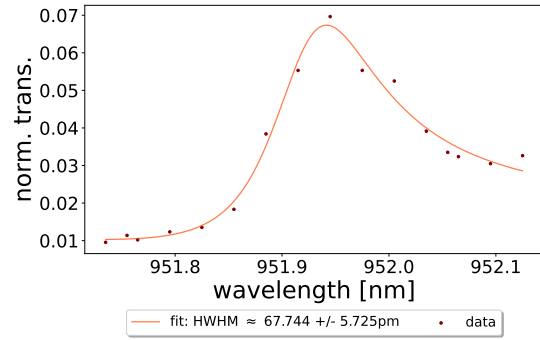
(a)



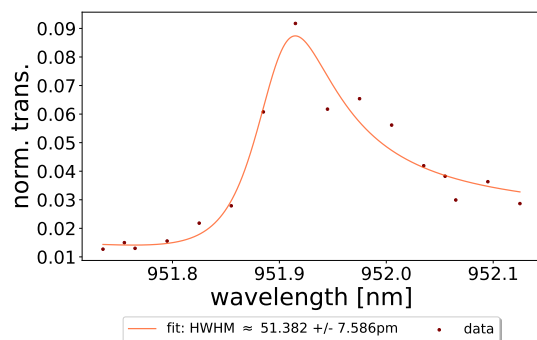
(b)



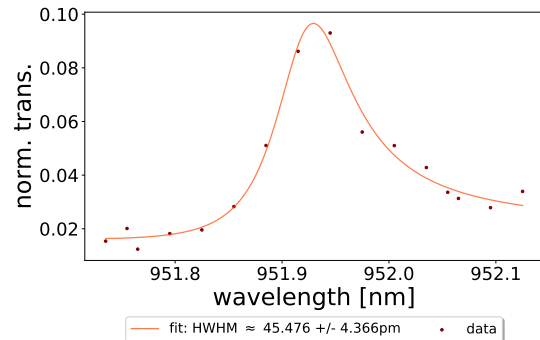
(c)



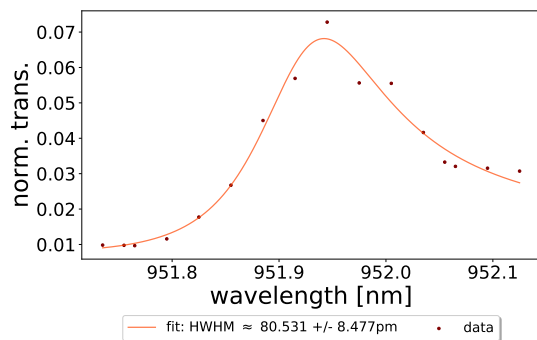
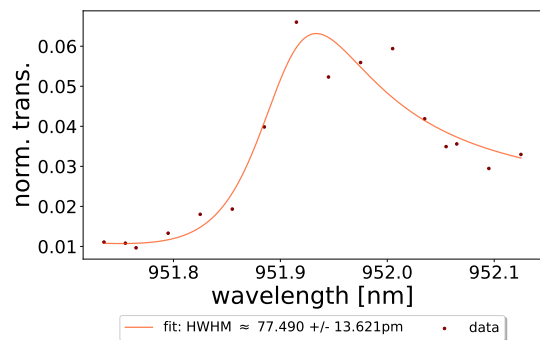
(d)



(e)

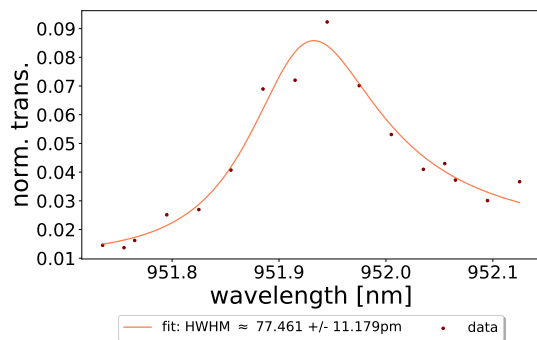
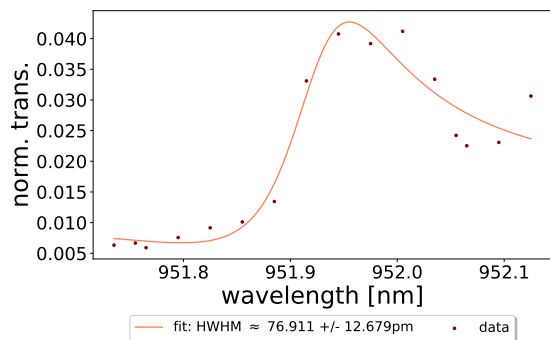


(f)



(g)

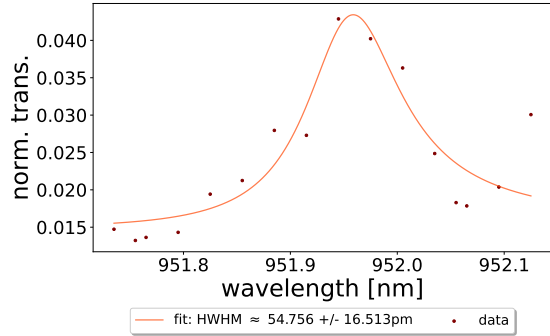
(h)



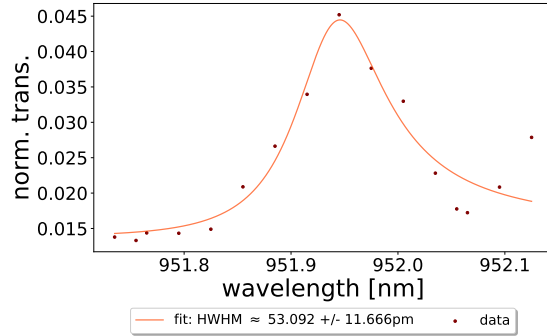
(i)

(j)

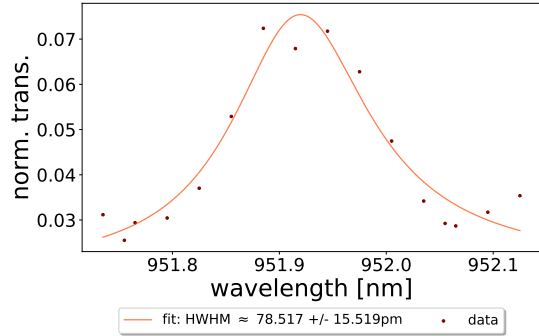
cavity length:  $l \approx 81\mu m$



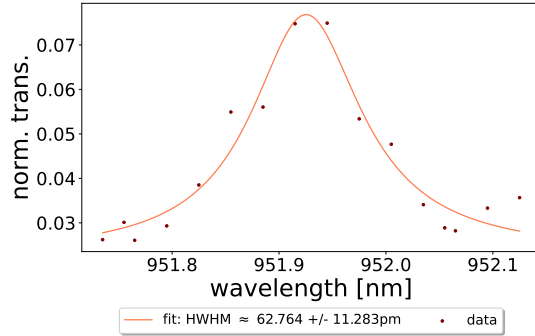
(a)



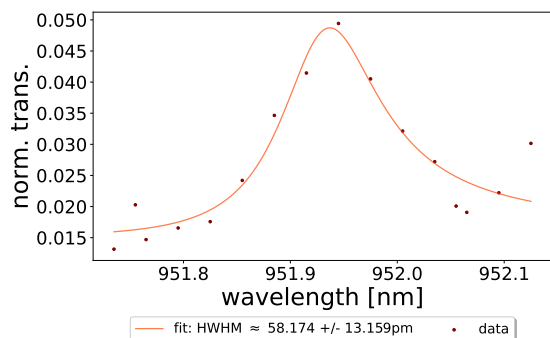
(b)



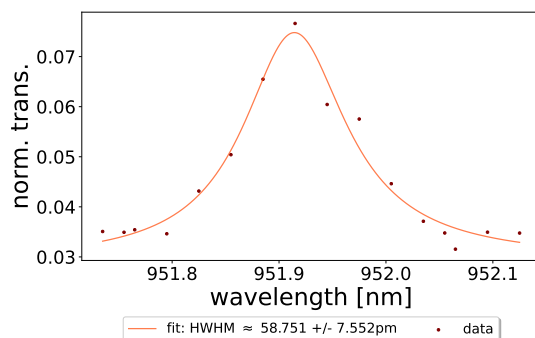
(c)



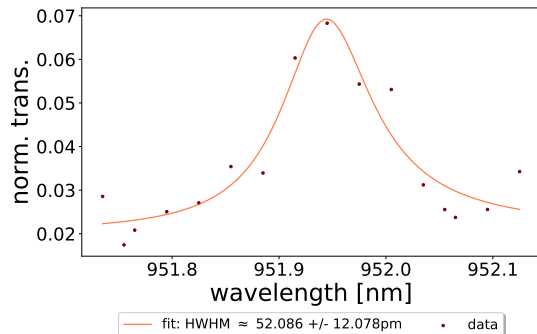
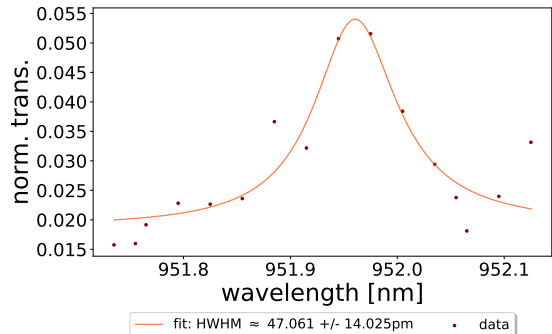
(d)



(e)

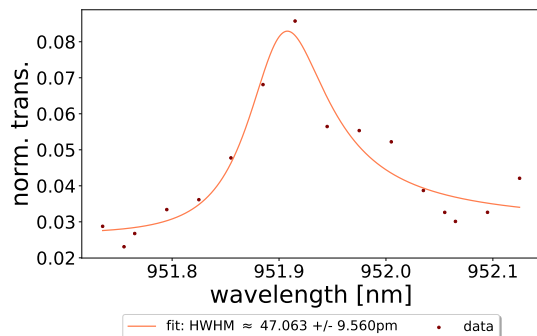
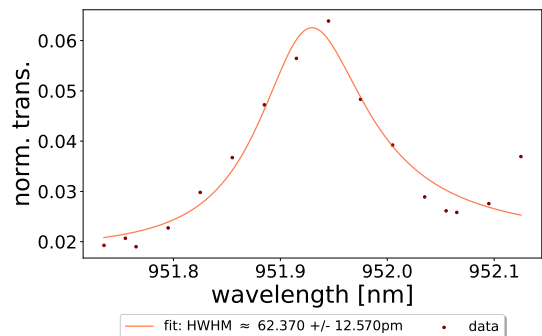


(f)



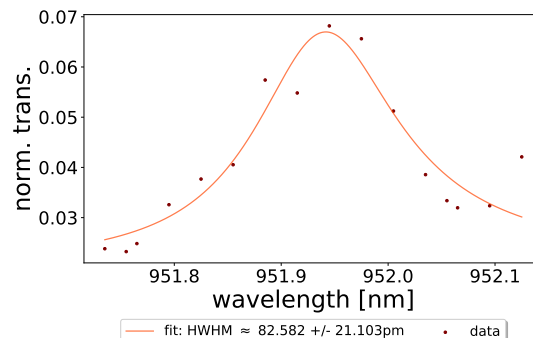
(g)

(h)



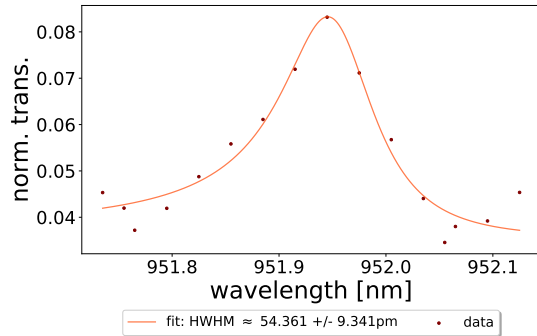
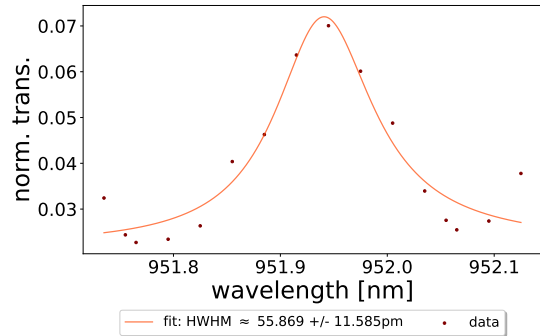
(i)

(j)



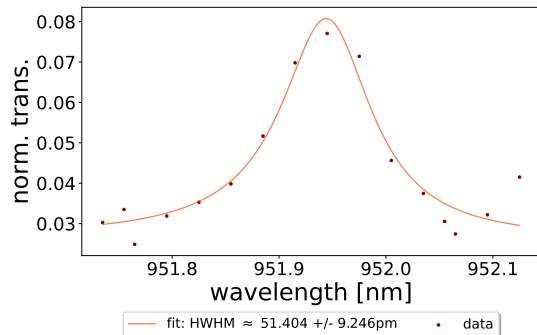
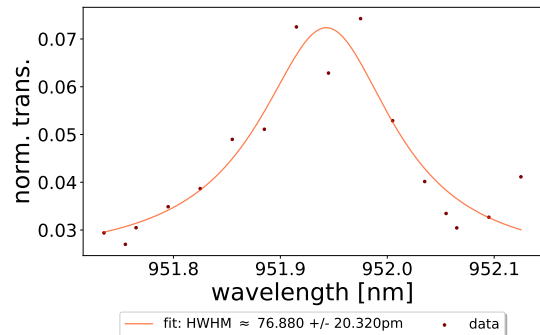
(k)

cavity length:  $l \approx 52\mu m$



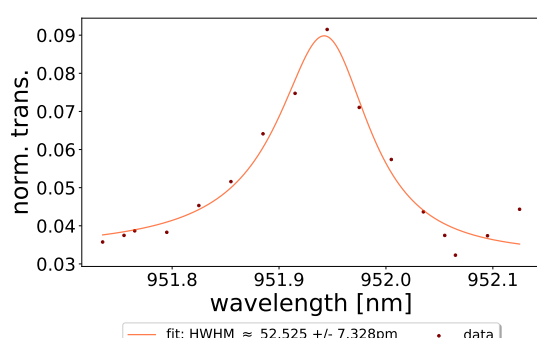
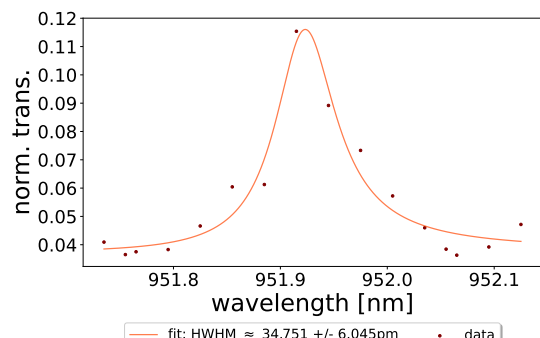
(a)

(b)



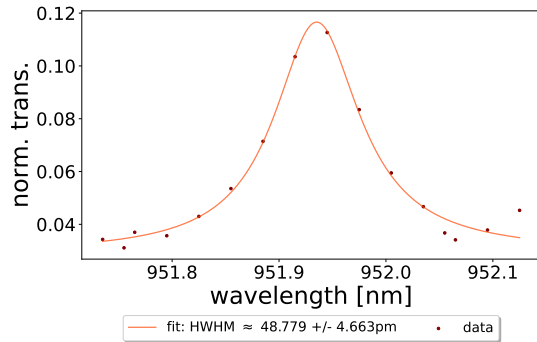
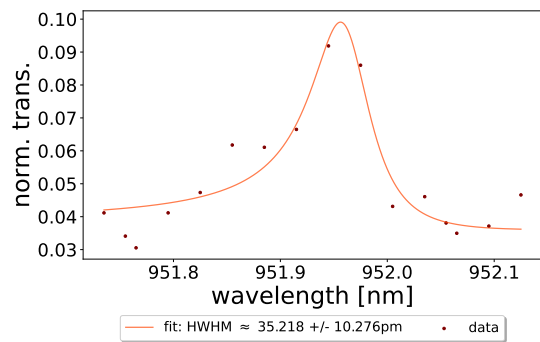
(c)

(d)



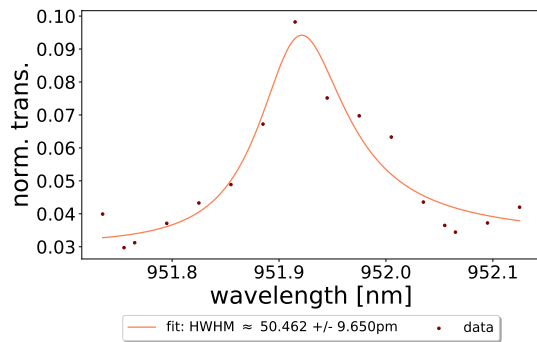
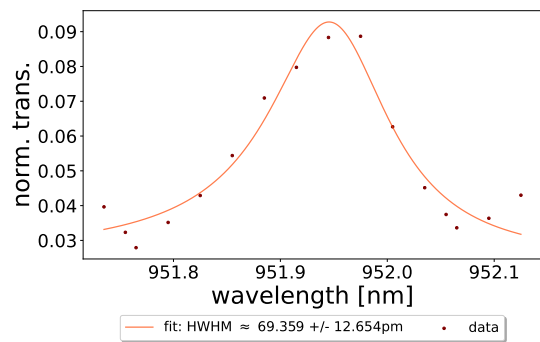
(e)

(f)



(g)

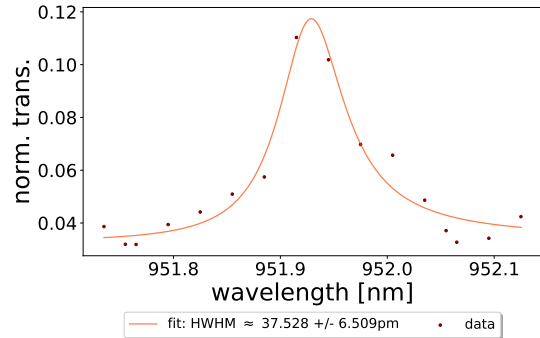
(h)



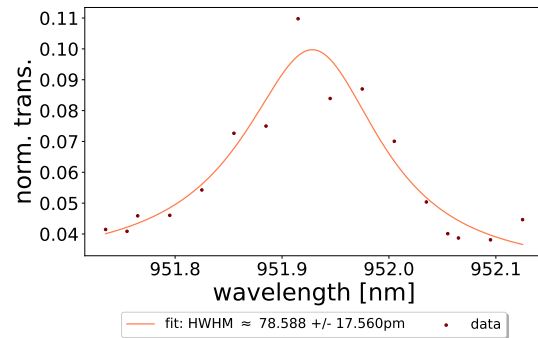
(i)

(j)

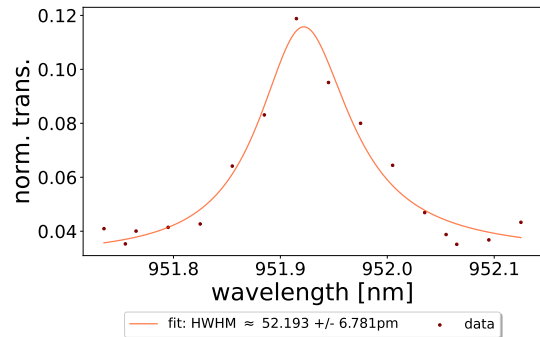
cavity length:  $l \approx 33\mu m$



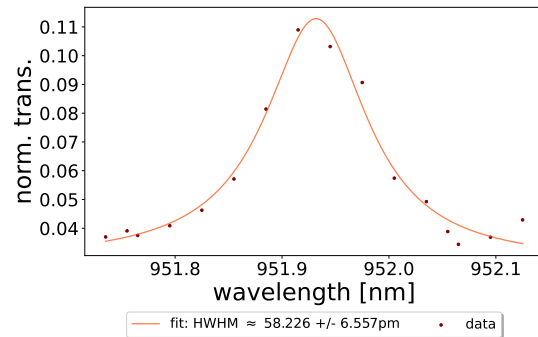
(a)



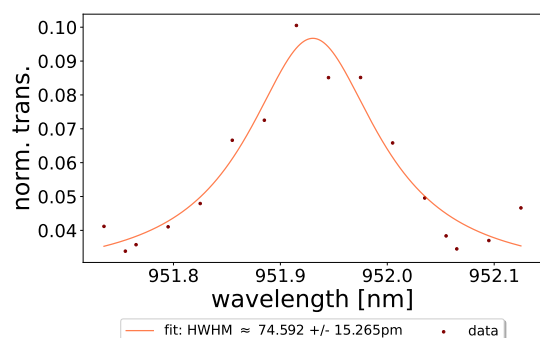
(b)



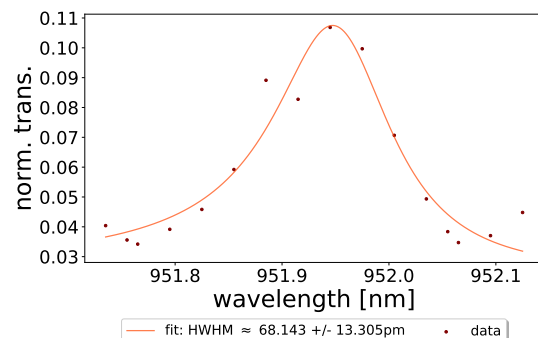
(c)



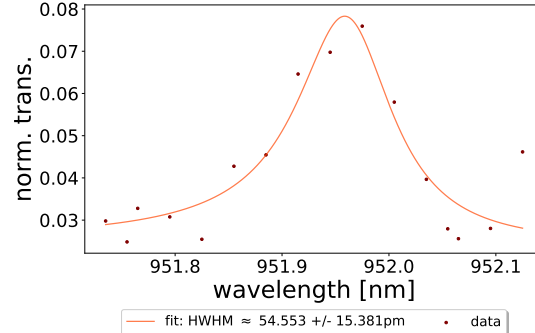
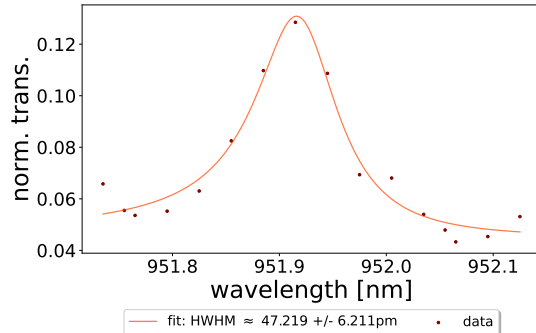
(d)



(e)

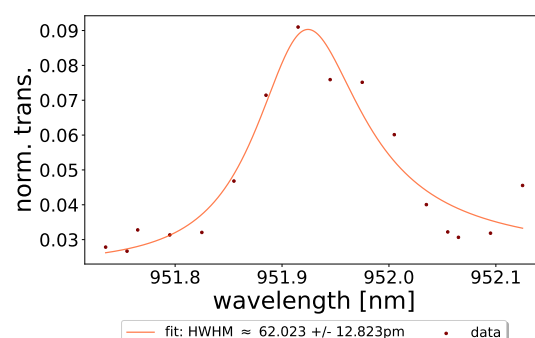
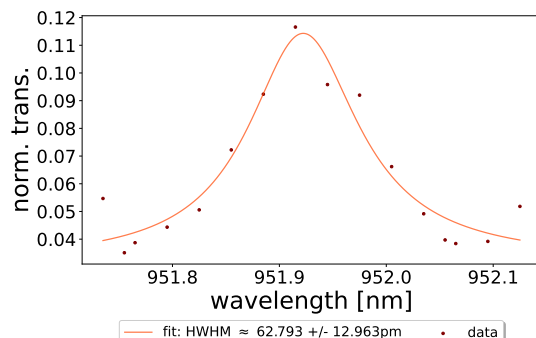


(f)



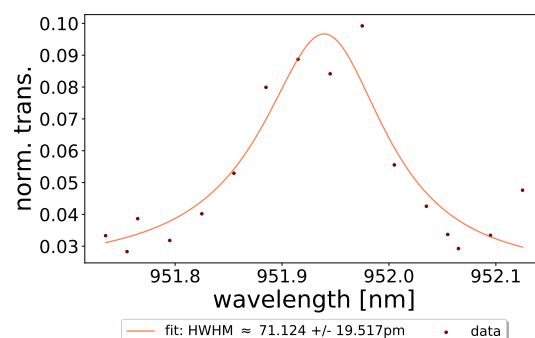
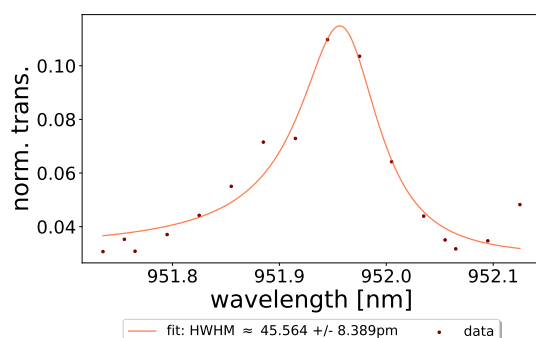
(g)

(h)



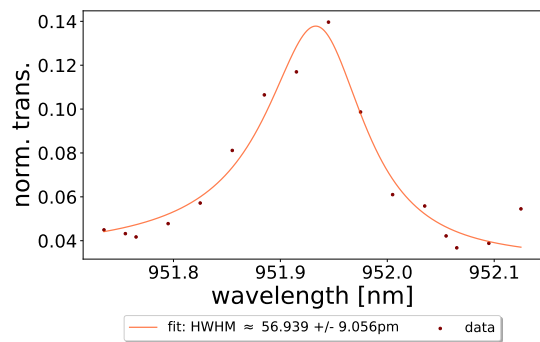
(i)

(j)

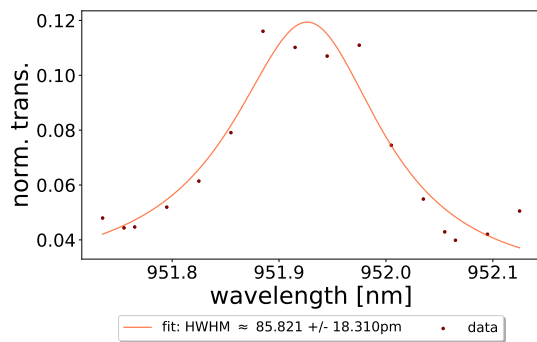


(k)

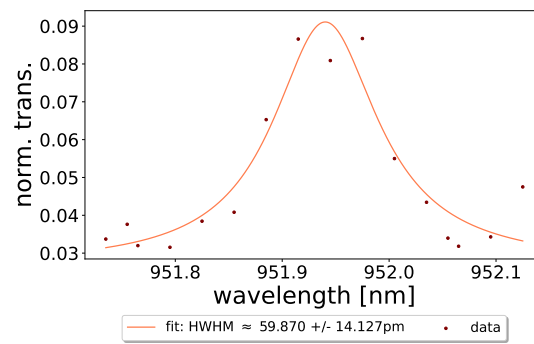
(l)



(m)

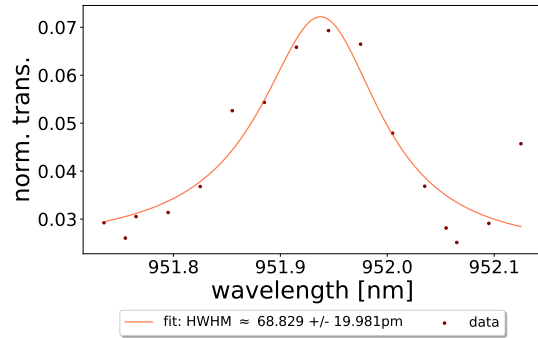


(n)

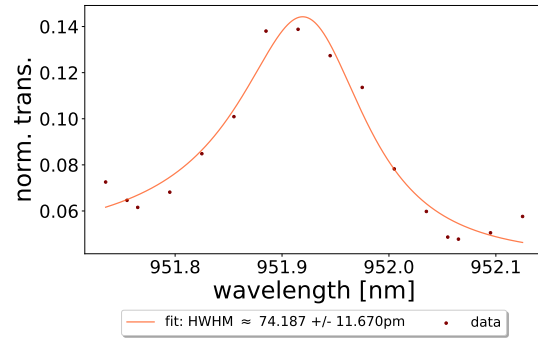


(o)

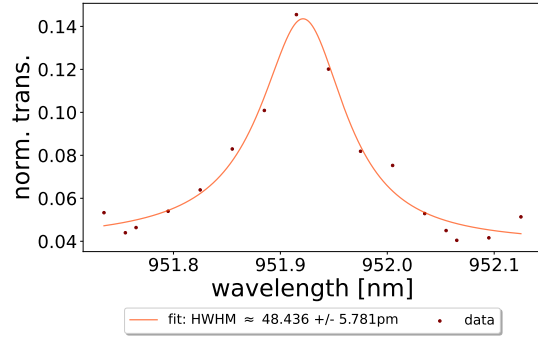
cavity length:  $l \approx 21\mu m$



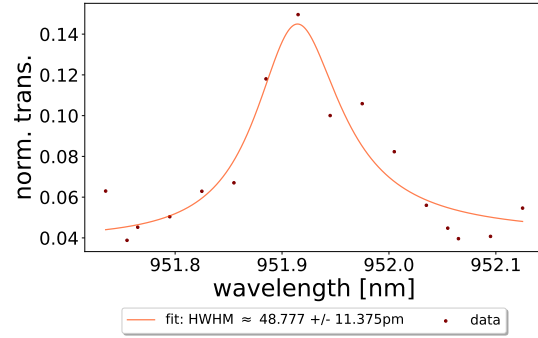
(a)



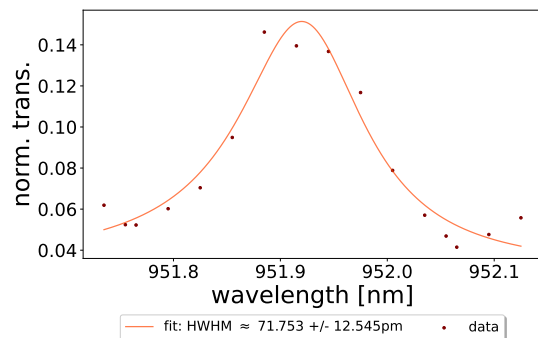
(b)



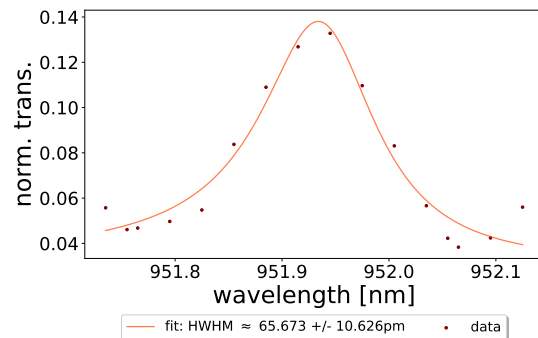
(c)



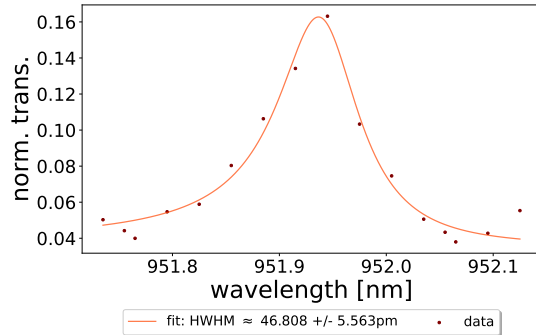
(d)



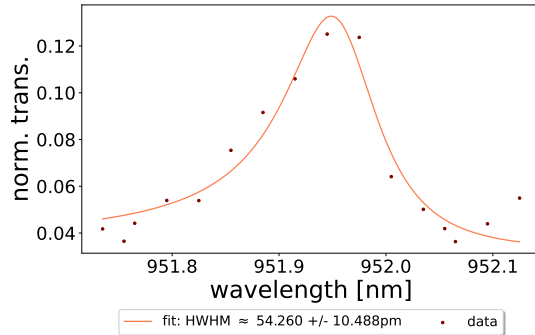
(e)



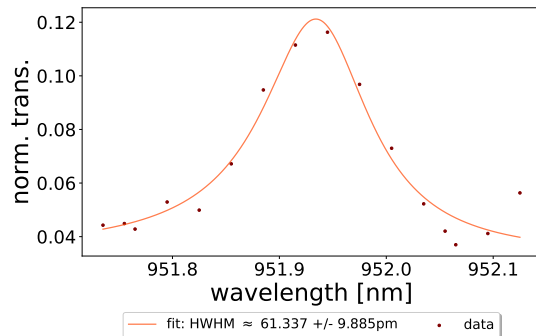
(f)



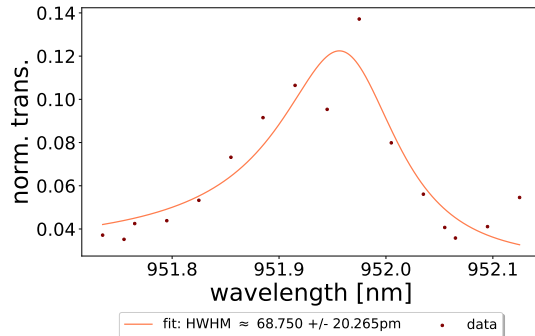
(g)



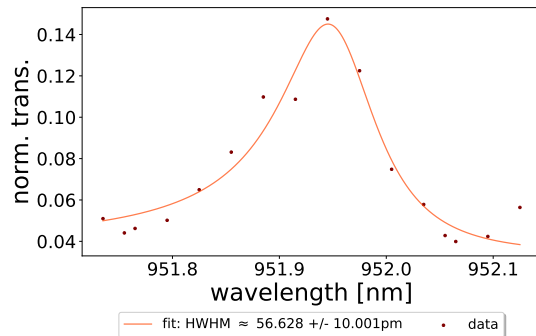
(h)



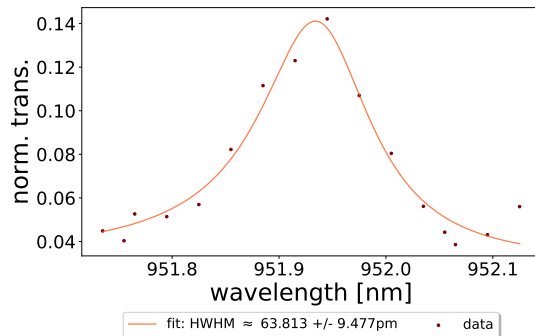
(i)



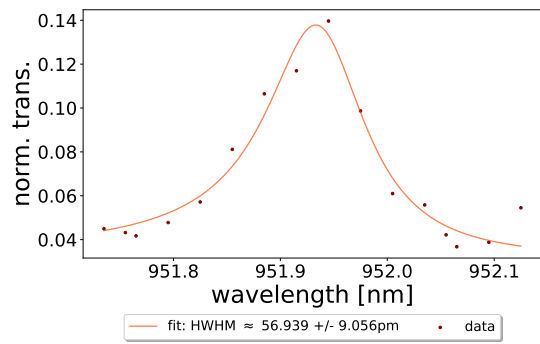
(j)



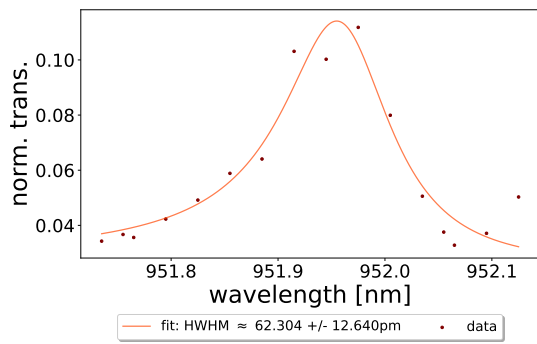
(k)



(l)



(m)



(n)